Influence of heterogeneities on the initiation of shear zones in the ductile regime

Author: Livia Nardini
Supervisor: Prof. Dr. Georg Dresen
Co-Supervisor: Dr. Luca Menegon
External Reviewer: Prof. Dr. Claudia Trepmann

Kumulative Univ.-Diss.
zur Erlangung des akademischen Grades
"doctor rerum naturalium" (Dr. rer. nat.)
in der Wissenschaftsdisziplin Geologie

Eingereicht an der
Mathematisch-Naturwissenschaftlichen Fakultät
Institut für Erd- und Umweltwissenschaften
der Universität Potsdam

Published online at the
Institutional Repository of the University of Potsdam:
https://doi.org/10.25932/publishup-44616
https://nbn-resolving.org/urn:nbn:de:kobv:517-opus4-446165

So tall, silent against the sky
Up through the clouds, where eagles fly
Wind and rain beat down on one so strong
They cut but never change, what stood so long

JOSEPH HELLMANN

Eidesstattliche Erklärung

Hiermit versichere ich an Eides statt, dass

- die eingereichte Arbeit oder wesentliche Teile derselben in keinem anderen Verfahren zur Erlangung eines akademischen Grades vorgelegt worden sind;
- bei der Anfertigung der Dissertation die Grundsätze zur Sicherung guter wissenschaftlicher Praxis der DFG eingehalten wurden, die Dissertation selbständig und ohne fremde Hilfe verfasst wurde, andere als die von mir angegebenen Quellen und Hilfsmittel nicht benutzt worden sind und die den benutzten Werken wörtlich oder sinngemäß entnommenen Stellen als solche kenntlich gemacht wurden.

Livia Nardini

Potsdam, den 02.10.2019

Abstract

The current thesis contains the results from two experimental and one modelling study focused on the topic of ductile strain localization in the presence of material heterogeneities. Localization of strain in the high temperature regime is a well known feature of rock deformation occurring in nature at different scales and in a variety of lithologies. Large scale shear zones at the roots of major crustal fault zones are considered responsible for the activity of plate tectonics on our planet. A large number of mechanisms are suggested to be associated with strain softening and nucleation of localization. Among these, the presence of material heterogeneities within homogeneous host rocks is frequently observed in field examples to trigger shear zone development. Despite a number of studies conducted on the topic, the mechanisms controlling initiation and evolution of localization are not fully understood yet. We investigated, experimentally and by means of numerical modelling, phenomenological and microphysical aspects of high temperature strain localization in a homogeneous body containing single and paired inclusions of weaker material. A monomineralic carbonate system composed of Carrara marble (homogeneous, strong matrix) and Solnhofen limestone (weak planar inclusions) is selected for our studies based on its versatility as an experimental material and on the frequent occurrence of carbonate rocks at the core of natural shear zones.

To explore the influence of different loading conditions on heterogeneity-induced high temperature shear zones we conducted torsion experiments under constant twist (deformation) rate and constant torque (stress) conditions in a Paterson-type deformation apparatus on hollow cylinders of marble containing single planar inclusions of limestone. At the imposed experimental conditions (900 °C temperature and 400 MPa confining pressure) both materials deform plastically and the marble is ≈ 9 times stronger than the limestone. The viscosity contrast between the two materials induces a perturbation of the stress field within the marble matrix at the tip of the planar inclusion. Early on along the deformation path (at bulk shear strains ≈ 0.3), heterogeneous distribution of strain can be observed under both loading conditions and a small area of incipient strain localization is formed at the tip of the weak limestone inclusion. Strongly deformed grains, incipient dynamic recrystallization and a weak crystallographic preferred orientation characterize the marble within an area a few mm in front of the inclusion. As the bulk strain is increased (up to $\gamma \approx 1$), the area of microstructural modification is expanded along the inclusion plane, the texture strengthens and grain size refinement by dynamic recrystallization becomes pervasive. Locally, evidences for coexisting brittle deformation are also observed regardless of the imposed loading conditions. A shear zone is effectively formed within the deforming Carrara marble, its geometry controlled by the plane containing the thin plate of limestone. Thorough microstructural and textural analysis, however, do not reveal substantial differences in the mechanisms or magnitude of strain localization at the different loading conditions. We conclude that, in the presence of material heterogeneities

capable of inducing strain softening, the imposed loading conditions do not affect ductile localization in its nucleating and transient stages.

As the ultimate goal of experimental rock deformation is the extrapolation of results to geologically relevant time and space scales, we developed 2D numerical models reproducing (and benchmarked to) our experimental results. Our cm-scaled models have been implemented with a first-order strain-dependent softening law to reproduce the effect of rheological weakening in the deforming material. We successfully reproduced the local stress concentration at the inclusion tips and the strain localization initiated in the marble matrix. The heterogeneous distribution of strain and its evolution with imposed bulk deformation (i.e. the shape and extent of the nucleating shear zone) are observed to depend on the degree of softening imposed to the deforming matrix. When a second (artificial) softening step is introduced at elevated bulk strains in the model, the formation of a secondary high strain layer is observed at the core of the initial shear zone, analogous to the development of ultramylonite bands in high strain natural shear zones. Our results do not only reproduce the nucleation and transient evolution of a heterogeneity-induced high temperature shear zone with high accuracy, but also confirm the importance of introducing reliable softening laws capable of mimicking strain weakening to numerical models of crustal scale ductile processes.

Material heterogeneities inducing strain localization in the field are often consisting of brittle precursors (joints and fractures). More generally, the interaction of brittle and ductile deformation mechanisms and its effect on the localization of strain have been a key topic in the structural geology community for a long time. The positive feedback between (micro)fracturing and ductile strain localization is a well recognized effect in a number of field examples. We experimentally investigated the influence of brittle deformation on the initiation and evolution of high temperature shear zones in a strong matrix containing pairs of weak material heterogeneities. Our Carrara marble-Solnhofen limestone inclusions system was tested in triaxial compression under constant strain rate and high temperature (900 °C) conditions in a Paterson deformation apparatus. The inclusion pairs were arranged in non-overlapping step-over geometries of either compressional or extensional nature. Experimental runs were conducted at different confining pressures (30, 50, 100 and 300 MPa) to induce various amounts of brittle deformation within the marble matrix. At low confinement (30 and 50 MPa) abundant brittle deformation is observed in all configurations, but the spatial distribution of cracks is dependent on the kinematics of the step-over region: concentrated along the shearing plane between the inclusions in the extensional samples, or broadly distributed around the inclusions but outside the step-over region in the compressional configuration. Accordingly, brittle-assisted ductile processes tend to localize deformation along the inclusions plane in the extensional geometry or to distribute widely across large areas of the matrix in the compressional step-over. At pressures of 100 and 300 MPa fracturing is mostly suppressed in both configurations and strain is accommodated almost entirely by viscous creep. In extensional samples this

leads to progressive de-localization with increasing confinement. Our results show that, while ductile localization of strain is indeed more efficient where assisted by brittle processes, these latter are only effective if themselves heterogeneously distributed, ultimately a function of the local stress perturbations.

Zusammenfassung

Die vorliegende Doktorarbeit umfasst Ergebnisse von zwei experimentellen und einer Modellierungsstudie. Diese befassen sich mit der Lokalisierung von duktilen Verformungen, hervorgerufen durch unterschiedliche Materialeigenschaften.

Die Lokalisierung von Verformungen im Hochtemperaturbereich in unterschiedlichen Maßstäben und in einer Vielzahl von Lithologien ist ein bekanntes Merkmal der natürlichen Gesteinsdeformationen. So wird beispielsweise die Aktivität der Plattentektonik unseres Planeten durch weiträumige Scherzonen am Grund dieser Plattengrenzen verantwortlich gemacht. Dabei wird eine große Anzahl von Mechanismen mit der durch die Verformung hervorgerufenen Materialermüdung und der Ausbildung der Lokalisierung in Verbindung gebracht. Dabei wird unter diesen Mechanismen das Vorhandensein von Materialheterogenitäten innerhalb eines Gesteins häufig als Auslöser für die Ausbildung von Scherzonen beobachtet. Obwohl bereits Studien zu diesem Thema durchgeführt wurden, sind die kontrollierenden Mechanismen, die für die Initiierung und Entwicklung der Lokalisierung zuständig sind, bis heute nicht vollumfänglich verstanden. Aus diesem Grund wurden im Rahmen der vorgelegten Dissertation phänomenologische und mikrophysikalische Aspekte der Lokalisierung von Verformungen im Hochtemperaturbereich in einem homogenen Gesteinskörper, der mit einfachen und gepaarten Inklusionen aus weicheren Material versehen wurde, experimentell und unter Hilfenahme von numerischen Modellen untersucht. Da Karbonatgesteine häufig am Ursprung natürlicher Scherzonen auftreten und diese für ihre Vielseitigkeit als Experimentiermaterial bekannt sind, wurde ein monomineralisches Karbonatsystem, bestehend aus Carrara Marmor (homogene, starke Matrix) und Solnhofen Kalkstein (schwache Inklusionen) als zu untersuchendes Probenmaterial für diese Studie gewählt.

Um den Einfluss unterschiedlicher Deformationsbedingungen auf die, durch die Materialheterogenität hervorgerufenen Scherzonen im Hochtemperaturbereich zu untersuchen, wurden Torsionsexperimente bei konstanter Torsionsrate und konstantem Drehmoment in einer Paterson-Deformationsapparatur an hohlen Carrara Marmorzylindern mit einer ebenen Inklusion bestehend aus Kalkstein durchgeführt. Unter den vorgegebenen Randbedingungen (Temperatur = 900 °C, Manteldruck = 400 MPa) verformten sich beide Materialien plastisch, wobei die Festigkeit des Marmors in etwa dem neunfachen der Kalksteinfestigkeit entspricht. An der Spitze der ebenen Kalksteininklusion wird durch den Viskositätskontrast der beiden Materialien dadurch eine Störung des Spannungsfeldes in der Marmormatrix hervorgerufen. In der frühen Phase der Deformation (Scherverformung $\gamma \approx 0.3$) kann eine heterogene Verteilung der Verformungen in der gesamten Probe bei beiden Experimenttypen beobachtet werden. Zusätzlich beginnt sich an der Spitze der schwächeren Kalksteininklusion ein Bereich mit lokaler Verformung in der Marmormatrix auszubilden. Dieser ist durch stark deformierte Mineralkörner, beginnende dynamische Rekristallisation und einer schwach ausgeprägten kristallographisch bevorzugten

Ausrichtung innerhalb einer Fläche weniger Millimeter charakterisiert. Mit ansteigender Gesamtverformung ($\gamma \approx 1$) erweitert sich die Fläche der mikrostrukturellen Modifikationen entlang der Inklusionsebene. Zusätzlich konnten eine verfestigte Textur und eine Verfeinerung der Korngröše aufgrund dynamischer Rekristallisation beobachtet werden. Lokale Anzeichen für eine gleichzeitige spröde Verformung konnten, unabhängig von den Deformationsbedingungen, ebenfalls festgestellt werden. Innerhalb des deformierten Marmors bildete sich eine Scherzone aus, deren Geometrie maßgeblich durch die Ebene der Kalksteininklusion kontrolliert wird. Sorgfältig durchgeführte mikrostrukturelle Analysen zeigten jedoch keine wesentlichen Unterschiede der Mechanismen oder dem Ausmaš der Lokalisierung der Verformung bei unterschiedlichen Deformationsbedingungen. Daraus lässt sich schließen, dass bei dem Vorhandensein von Materialheterogenitäten, welche eine verformungsbedingte Materialermüdung hervorrufen können, die verwendeten Deformationsbedingungen keinen Einfluss auf die Lokalisierung duktiler Deformation in ihrer Entstehung und übergangsphasen haben.

Da für gewöhnlich die Durchführung von Deformationsexperimenten auf die Extrapolation der gewonnenen Ergebnisse auf geologische Zeiträume abzielt, wurden zwei- dimensionale numerische Modelle entwickelt, welche in der Lage sind die aufgenommenen experimentellen Daten zu reproduzieren und zu bewerten. Diese, auf dem Zentimetermaßstab skalierten Modelle wurden mit einem verformungsbasierten Ermüdungsgesetz erster Ordnung umgesetzt, um den Effekt der rheologischen Materialermüdung nachzubilden. Die lokale Spannungskonzentration an der Spitze der Inklusionen und die in der Marmormatrix initiierten Lokalisierung der Verformung konnten mit diesen Modellen erfolgreich reproduziert werden. Dabei wurde festgestellt, dass die heterogene Verteilung der Verformung und deren Entwicklung mit zunehmender Gesamtverformung (z.B. Form und Umfang der sich ausbildenden Scherzone) abhängig vom Grad der Ermüdung der deformierten Matrix ist. Analog zu der Entwicklung von Ultramylonitbändern in natürlichen Scherzonen mit hoher Verformung, konnte bei der Einführung eines zweites (künstlichen) Ermüdungsschritts bei erhöhter Gesamtverformung, die Ausbildung einer zweiten Schicht mit grošer Verformung am Kern der initialen Scherzone beobachtet werden. Mit den gewonnenen Ergebnissen der numerischen Simulationen wurde nicht nur die Ausbildung und transiente Entwicklung, der durch die Materialheterogenität hervorgerufenen Scherzone im Hochtemperaturbereich mit grošer Genauigkeit reproduziert. Auch wurde die Wichtigkeit verlässliche Ermüdungsgesetze aufzustellen, die in der Lage sind die durch die Verformung hervorgerufenen Materialermüdung im geologischen Maßstab unter Hinzunahme von numerischen Modellen nachzuahmen, bestätigt.

Die durch Materialheterogenitäten hervorgerufene Lokalisierung von Verformungen in der Natur bestehen häufig aus spröden Vorläufern, wie beispielsweise Klüften und Rissen. Die Interaktion von spröden und duktilen Deformationsmechanismen im Allgemeinen und ihr Effekt auf die Lokalisierung von Verformungen sind seit langem Schlüsselthema auf dem Gebiet der Strukturgeologie. Die Kopplung von spröden Bruchprozessen mit

der Lokalisierung duktiler Verformungen ist oft Gegenstand der Untersuchung in einer Vielzahl von Feldstudien. Daher wurde experimentell der Einfluss von spröder Deformation auf die Initiierung und Entwicklung von Hochtemperatur Scherzonen in einer starken Matrix mit schwächeren Materialheterogenitäten untersucht. Dafür wurden Carrara Marmor-Solnhofen Kalksteininklusions-Systeme unter triaxialen Bedingungen bei konstanter axialer Verformungsrate und hoher Temperatur (T = 900 °C) in einer Paterson-Apparatur deformiert. Dabei wurden die Inklusionen in einer übereinander liegenden, aber nicht überlappenden Geometrie so angeordnet, dass sich bei axialer Probendeformation entweder Kompression oder Dehnung in der Fläche zwischen den Inklusionen einstellt. Die Versuche wurden bei verschiedenen Manteldrücken (P = 30, 50, 100 und 300 MPa) durchgeführt, um unterschiedliche Beträge an spröder Deformation in der Marmormatrix hervorzurufen. Bei geringen Manteldrücken (P = 30 und 50 MPa) kann ein hoher Anteil an spröder Deformation in allen Probenkonfigurationen beobachtet werden. Allerdings ist die räumliche Verteilung der Risse abhängig von der Kinematik der sich übereinanderliegenden Inklusionen. Bei der Dehnungskonfiguration sind die Risse entlang der Scherfläche zwischen den Inklusionen konzentriert, während sie bei der Kompressionskonfiguration auŝer halb der Inklusionen weit verteilt sind. Dementsprechend neigen duktile, durch spröde unterstützte Prozesse Deformationen entlang der Inklusionsebene bei Dehnung zu lokalisieren oder sich über weite Fläche der Matrix bei Kompression zu verteilen. Bei Manteldrücken von 100 und 300 MPa ist die Risserzeugung in beiden Konfigurationen weitestgehend unterdrückt und die Verformung wird fast ausschlieŝlich durch viskoses Kriechen akkommodiert. Mit ansteigendem Manteldruck führt das bei Proben der Dehnungskonfiguration zu fortschreitender De-Lokalisierung. Die Ergebnisse zeigen, dass die Lokalisierung von duktilen Verformungen effizienter ist, wenn diese durch spröde Bruchprozesse assistiert werden. Allerdings sind diese spröden Prozesse nur dann effektiv, wenn sie heterogen verteilt sind, was letztendlich eine Funktion der lokalen Spannungsstörungen ist.

Statement of contribution

The cumulative thesis here presented consists of two peer-reviewed papers that have been published in scientific journals and one paper which has been submitted for publication and is currently under review. The PhD candidate is first author of two of these three papers, which constitute Chapters 2, 3 and 4 of the thesis. Each of these chapters is organized according to its published structure, namely comprising introduction, methods, results, discussion, conclusions and acknowledgements.

A general introduction to the topic and the project is given in Chapter 1, while major conclusions and an outlook of future work are presented in Chapters 5 and 6. A combined reference list (for both introduction, conclusions and individual papers) is presented at the end of the thesis.

The major results of this project are published or submitted for publication as:

Chapter 2: L. Nardini, E. Rybacki, M. J. E. A. Döhmann, L. F. G. Morales, S. Brune, G. Dresen, 2018. "High-temperature shear zone formation in Carrara marble: The effect of loading conditions" published in Tectonophysics, doi: 10.1016/j.tecto.2018.10.022. The paper was authored by the PhD candidate; the revisions made by the co-authors helped improving the paper substantially.

Chapter 3: M. J. E. A. Döhmann, S. Brune, L. Nardini, E. Rybacki, G. Dresen, 2019. "Strain Localization and Weakening Processes in Viscously Deforming Rocks: Numerical Modeling Based on Laboratory Torsion Experiments" published in Journal of Geophysical Research: Solid Earth, doi: 10.1029/2018JB016917. The PhD candidate co-authored this paper.

Chapter 4: L. Nardini, E. Rybacki, M. Krause, L. F. G. Morales, G. Dresen, "Control of the geometric arrangement of material heterogeneities on strain localization at the brittle-to-ductile transition in experimentally deformed carbonate rocks" submitted to Journal of Structural Geology, currently under review. The paper was authored by the PhD candidate; the revisions made by the co-authors helped improving the paper substantially.

Declaration

The PhD project here presented was funded via the DFG grant GR 4468/2. Experimental and analytical work was carried out mainly by the PhD candidate with contributions from the co-authors. Deformation experiments were carried out in a Paterson-type deformation apparatus at the Deutsche GeoForschungZentrum (GFZ) in Potsdam (Germany) under the supervision of Michael Naumann, who is greatly acknowledged. Samples and thin sections preparation was carried out by Stephan Gehrmann (GFZ). Electron microscopy (SEM) and electron-backscattered diffraction (EBSD) were conducted by the PhD candidate after training by Dr. L. F. G. Morales. Transmission electron microscopy (TEM) was performed under the supervision of Dr. Richard Wirth. The numerical modelling presented in Chapter 3 was run on the cluster facilities of the Deutsche GeoForschungZentrum (GFZ) in Potsdam; additional funding from the Helmholtz Young Investigators Group CRYSTALS (VH-NG-1132) is acknowledged.

Acknowledgements

First and foremost, I would like to thank my main supervisor, Professor Dresen. You have been an inspiration and a guide, and I am very grateful I had a chance to learn so enormously much during the long discussions we had over my not always so convincing results. You might not have taken the Thomas Mann out of me yet, but I still feel like I have put to good use a number of your wise advices.

To Erik, who has been the best unofficial-but-really-de-facto supervisor anyone could wish for, goes all my gratitude: thank you for always having an open door to discuss all my silly doubts (scientific as well as existential), for the invaluable help you gave me, for the pep talks you had to give when my structural insecurity would surface and I would distrust everything I do. Thank you for keeping up with the ridiculous review-deadlines I set in the past few months and for helping me get past my recent breakdowns. I am a better scientist thanks to you, and I might have even climbed a tiny step up the self-confidence ladder.

Michael and Luiz have been amazing people to work with. I have learned a ton of things from both of you guys, and have enjoyed every minute we spent together in the supertidy Paterson lab or in the freezing SEM room; you can always create a wonderful working atmosphere and I am truly happy I had the chance to meet both of you. Special thanks go to Rita, the loveliest secretary in the world and the most caring person ever.

My fellow middle-earthers, Johannes, Stephan, Vanessa and Bernhard, are probably the reason I didn't quit within the first six months of my PhD. You guys have always managed to put a smile on my face no matter what, and you supported me through the tough times. Together with Audrey, Io, Amandine, Vivi, Valerian, Claudius, Bita, Christopher, Maria, Aglaja and Lea you have been the best bunch one could hope to meet on the work place. I am going to miss the coffee breaks and the lunches in the post-zombie-apocalypse conference room, but I count on still being part of the karaoke committee in the future!

So many friends have been my strength during the past three and a half years – and really the best part of my life. Giacomino, Cecilia, Katharina, Federica, Dasha, Gaia, Giulio, Toby, Christian, Jack, Giorgino, Brecht: life wouldn't be half as good without the skype calls, the holidays together, the spontaneous meetups and the not-so-spontaneous visits to each other across the whole of Europe, the wonderful memories we share and the certainty that many more are yet to come. Thanks for being there for me, and for putting up with so much of my craziness.

Thanks a bunch to my geo-friends from the Uni days as well: Teo, Stefania, Lele, Iso, Andrea, Alice and Davide, it's so nice to be able to still have our traditional geo-lunches every once in a while when I show up in Italy. It reminds me of the good old days full of card-games during lunch break, crowded study sessions in the only room with AC in the whole department and of course the best excursions in the history of the University

of Padova.

Finally, I want to thank my amazing family for simply being there for me, in all possible ways. My lovely sisters, who showed me how meaningless distance can be, are my best friends and the people I care for the most in the whole world. We are different like flowers growing in the same garden, and I love the way that bonds us. A huge thank you to my wonderful parents, who worked relentlessly to provide me and my sisters with every opportunity in life, and taught us how to seize them. Knowing that I can count on you no matter what is the greatest gift you could give me, and I feel unbelievably lucky to be your daughter.

Contents

List of Figures

List of Tables

1 General Introduction

1.1 Motivation

The study of the physical state of rocks in relationship to the conditions of pressure and temperature they are subjected to over geological time scales is essential for the understanding of global geological processes. Plate tectonics, to the best of our knowledge only occurring on our planet, has been suggested to be primarily responsible for the evolution of complex life on Earth (Stern, 2016). Yet, this apparently simple process involves the complex interaction of different styles of deformation and the coupling, at depth, of some of Earth's structural components, which are characterized by markedly dissimilar mechanical behaviours.

Accessing the depths at which high temperature and high-pressure deformation processes are taking place is unattainable with the current technologies. To this day, the deepest borehole ever drilled is the Kola Superdeep Borehole located in north-eastern Russia, with a true vertical depth of about 12 km. The classic view of the layering of the continental crust, albeit strongly dependent on the tectonic setting, predicts an upper layer of about 12-13 km thickness, underlain by middle crustal material down to 23-24 km depth and a lower crust extending to a depth of 35-40 km (e.g., Rudnick & Gao, 2003; Huang et al., 2013). Due to the current lack of ultra-deep boreholes, indirect methods of investigation are necessary to gain information on the styles of deformation within deeper crustal levels. The study of outcropping middle and lower crustal material, experimental high temperature deformation and geodynamic modelling are typical approaches that attempt to understand the phenomenological and physical aspects of the rheology of crustal rocks. Each of these methods, taken separately, involves imponderables which can substantially hamper the reliability of interpretations. Field examples are the result of naturally occurring processes, but the exposure of deep crustal material to the Earth's surface by necessity involves some degree of overprinting of original structures during exhumation. Moreover, the number of variables present in nature is inherently larger than that of the constraints that can be placed on the final structures under examination. Experimental work, while allowing for more control over the system components and intervening processes, requires substantial spatial down-scaling and orders of magnitude faster deformation rates with respect to nature. Numerical modelling, on the other hand, requires substantial simplifications of the processes involved and often fails at dealing with non-linear interactions of mechanisms. Therefore, a multi-disciplinary approach is essential to obtain a holistic understanding of the rheology of the deeper crustal levels.

Experimental rock deformation is the subject of this study dealing with the processes and parameters controlling the localization of strain in the nominally ductile regime, a common occurrence in nature. Localization is a key mechanism of deformation in deep crustal environments, as testified by the abundance of outcropping examples of

high temperature shear zones (see ***section 1.2.2***). In addition, numerical modelling is benchmarked to some of the experimental results to mathematically reproduce the strain softening mechanisms at the basis of ductile localization.

1.2 Rheology of the lithosphere

Mechanisms of deformation within the Earth's crust vary with temperature and pressure conditions, i.e. with depth. While the upper continental crust deforms largely by pressure-dependent frictional sliding along pre-existing discontinuities (fault planes), slow temperature-dependent viscous flow is dominating in deeper regions of the crust. Markedly different physical properties are responsible for the different styles of mechanical response to stress. The dependence on strain rate and rock composition is, for example, characteristic of viscous rheologies, while brittle deformation is largely independent of both (Burov, 2011).

A plethora of studies has addressed the topic of rheology of the Earth's crust in an attempt to constrain the strength of the lithosphere (e.g., Goetze & Evans, 1979; Brace & Kohlstedt, 1980; Jackson, 2002; Afonso & Ranalli, 2004; Burov et al., 2006; Bürgmann & Dresen, 2008; Burov, 2011).

The definition of yield strength envelopes by Goetze and Evans (1979), largely based on experimental mechanical data extrapolated to natural conditions, represented the first quantification of the differential stresses supported by crustal material with increasing confining pressure as a function of their rheological properties. Ever since, a number of - somewhat simplified - models has been proposed that estimate the distribution of lithospheric strength with depth. The so-called "jelly-sandwich model" (Fig.1) prescribes a weak lower crust sandwiched between stronger upper crust and uppermost mantle. It is based on flow laws for wet quartz and feldspar representing the major constituents of the lower crust and on the rheology of dry olivine, which is assumed to be characteristic for the mechanically stronger mantle (reviewed in Bürgmann & Dresen, 2008) and it is the most accredited rheological model of the Earth's crust and uppermost mantle. An alternative model prescribing a weak mantle underlying a strong crust (assuming a dry feldspar rheology for the lower crust) has been proposed based on conservative estimates of the elastic thickness of the lithosphere (the crème brûlée model, Fig.1; Jackson, 2002). Modelling of gravimetric anomalies and growth time of convective instabilities in the mantle, together with considerations on the surface heat flow in cratonic areas, seem to contradict such a model and point in the direction of high mantle strength in a number of tectonic settings (e.g. orogenic belts, rifts, cold cratons, foreland basins, volcanic arcs), as shown by Burov et al. (2006). Regardless of the preferred model, interpretation of the distribution of strength within the lithosphere appears to be substantially more complex in continental settings than in oceanic ones: longer (and more variable) thermal histories, together with a larger compositional variability characteristic of the continental crust

are contributing to considerable uncertainty in the premises to the formulation of such simplified rheological models.

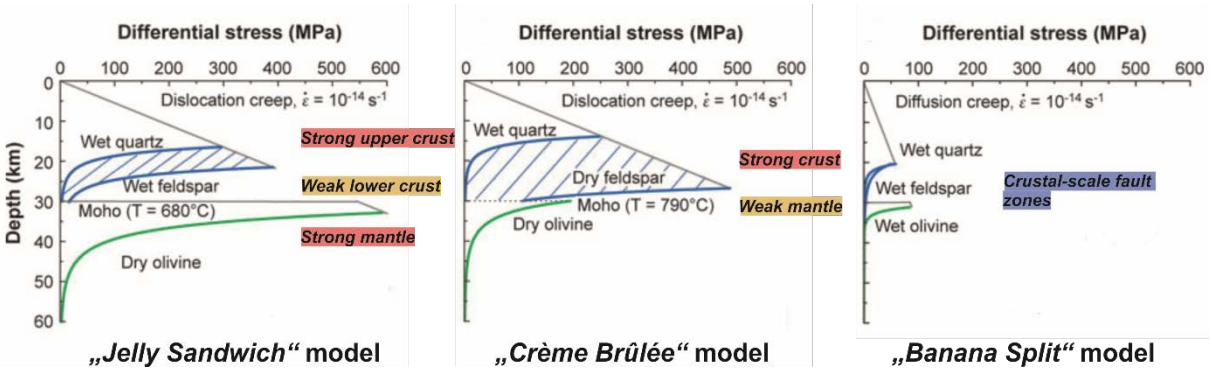

Figure 1: (modified from *Fig.1* in Bürgmann and Dresen (2008)); semi-quantitative scheme of the different models for lithospheric strength profiles.

Based on experimental rock mechanics, constitutive laws for high temperature creep of the most important constituents of the Earth's crust were suggested, which allow to estimate the bulk creep behaviour of rocks at large depths (e.g., Bürgmann & Dresen, 2008). Quartz, feldspar and pyroxene are the three major components of the continental crust, while olivine and pyroxene are assumed to be representative of the upper mantle, together with smaller amounts of other mineral phases. Relatively few materials, then, need (in principle) to be mechanically characterized to provide end-member type models of deeper crustal and upper mantle rheology. In the past decades, a substantial effort has been devoted to the experimental study of high temperature creep of these single phases (e.g., Dimanov et al. (1998), Dimanov et al. (1999), Rybacki and Dresen (2000), Rybacki et al. (2006) on feldspar; Bystricky and Mackwell (2001) and S. Chen et al. (2006) on pyroxenes; Mei and Kohlstedt (2000), Bystricky et al. (2000), Hirth and Kohlstedt (2003) and references therein on olivine). The extrapolation of this type of laboratory data to the deformation of multiphase rocks under natural conditions, however, rests on assumptions that are, at best, not entirely realistic. The expectation that the weakest or the most abundant phase is controlling the bulk mechanical behaviour of the aggregate, for example, doesn't take into account strain and strain rate dependency of creep in mineral phases (Handy, 1990; Handy & Brun, 2004). Numerical modelling, theoretical studies and, more recently, experimental data of multi-phase aggregates have pointed out the shortcomings of assuming a simple single phase rheology as representative of large portions of the lithosphere (e.g., Handy, 1990; Tullis et al., 1991; Handy, 1994; Thatcher & England, 1998; Ji et al., 2000, 2001; Dimanov et al., 2003; Rybacki et al., 2003; Dimanov et al., 2007).

Constitutive behaviour of polyphase aggregates depends on a number of factors: composition, strength difference of the phases, topography, grain size (and its effect on the dominating deformation mechanism), water and/or melt content among others (e.g., Handy, 1990, 1994; Dimanov et al., 2003). Assuming homogeneous stress and strain

rate distribution within multiphase aggregates in the lithosphere ignores the well documented presence of large volumes of long-lived, structural weakness at depth associated with shallow crustal scale fault zones (e.g., Zhu, 2000; Little et al., 2002; Kenner & Segall, 2003; Vauchez & Tommasi, 2003; Weber et al., 2004). The recently proposed model of a laterally varying lithosphere strength profile (the "banana split model" in Bürgmann & Dresen, 2008, ; Fig.1) provoked discussion over whether the bulk rheology of the lithosphere is in fact controlled by the behaviour of large weakened areas of localized strain extending to large depth across the entire crust and, potentially, into the lithospheric mantle. The mechanisms controlling the nucleation, evolution and mechanical behaviour of these zones (commonly known as "shear zones", see ***section 1.2.2***) have been the subject of extensive investigation in the past decades. Understanding their nature and rheological behaviour is important to unravel the mechanisms controlling the earthquake cycle on Earth. Advances on our probabilistic analysis of the seismic risk require a sounder modelling of stress distribution at all levels within the Earth's crust (Bürgmann et al., 2002). Knowing whether large episodic displacements due to shallow seismic slip are transferred to depth through distributed viscous shearing or via highly localized aseismic deformation is key to assess and mitigate the seismic hazard.

1.2.1 The brittle-to-ductile transition

Whichever model of lithospheric strength is preferred, a transition is prescribed to occur with depth between brittle failure and ductile flow. The depth (expressed in terms of in-situ temperature) at which crystal plasticity is activated and the differential stress becomes smaller than the effective confining pressure (Kohlstedt et al., 1995) marks the so-called brittle-to-ductile transition. It should be borne in mind, however, that the relatively sharp transition between friction and creep strength that derives from the extrapolation of flaw laws for the major components of the Earth's crust and the frictional strength for a given tectonic stress regime determined by the so-called Byerlee's law (Byerlee, 1978) does not necessarily represent what occurs at the microscale within rocks that are composed of several minerals. For example, as feldspar is usually stronger than quartz in nature, the former will display brittle behaviour at temperatures already allowing plastic processes in quartz to occur. It is clear, then, that the bulk behaviour of rocks is controlled by the relative amounts and distribution of their constituent phases (e.g., Handy, 1990). The brittle-to-ductile transition is, therefore, a region of the crust of varying thickness depending (not only) on the lithologies involved, within which a regime of "semibrittle behaviour" can be recognized (Kohlstedt et al., 1995). As the mechanical behaviour of mineral phases is dependent on the conditions of stress, temperature, strain rate and fluid pressure they are subjected to, any change in these parameters could contribute to transient or permanent variations in the depth and thickness of the brittle-to-ductile transition. For example, in the Sesia zone (an exposed lower crustal section of the Alpine

nappe pile) microstructures record the occurrence of high stress co-seismic loading transiently extending the depth of brittle deformation into portions of the crust typically characterized by viscous flow (below 13-15 km depending on the derived thermal structure, W.-P. Chen & Molnar, 1983) (Küster & Stöckhert, 1999; Trepmann & Stöckhert, 2002, 2003). Similarly, recent studies have proposed the occurrence of lower crustal seismicity in different tectonic settings (e.g., Maggi, Jackson, Mckenzie, & Priestley, 2000; Maggi, Jackson, Priestley, & Baker, 2000; Fagereng, 2013; Menegon et al., 2017). On a more local scale, a strain-dependent brittle-to-ductile transition has been suggested to operate during the evolution of large anastomosing shear zone networks (Fusseis et al., 2006). Ultimately, transient deformation can lead to a certain degree of dynamic change in the rheological response of rocks to imposed stress. The interaction between brittle and ductile processes at different boundary conditions can play a major role in the localization of strain at depth within the lithosphere, as will be discussed in the next section.

1.2.2 Localized deformation in the viscous regime: high-temperature shear zones

Ductile localization of strain under conditions of high temperature and pressure is a ubiquitous feature within lower crustal levels, as testified by the large number of exhumed field examples of high-temperature shear zones developing in different lithologies and across a variety of tectonometamorphic conditions (e.g., Burg & Laurent, 1978; Berthé et al., 1979; Vauchez et al., 1995; Christiansen & Pollard, 1997; Carreras, 2001; Ebert et al., 2007; Pennacchioni & Mancktelow, 2007). Shear zones are a key feature of deeper crustal deformation and have been proposed to be necessary to sustain the very mechanism of plate tectonics on our planet (Bercovici & Ricard, 2012) by allowing deformation in the ductile field to be localized at plate boundaries. Shear zones are defined as scale-independent zones of higher strain with respect to their surroundings. A strain gradient (as visualized by characteristic microstructures like sigmoidal foliation, passive rotation of markers, cleavage planes) is usually present from the core of the shear zone towards the margins, with the wall rock characterized by substantially lower strain, down to seemingly undeformed material (see Fossen & Cavalcante, 2017, for a review). As large-scale shear zones have been shown to extend to deep crustal levels, changes in dominating microstructure, rheological behaviour and mesoscale features (collectively named “shear zone facies”, following Fossen & Cavalcante, 2017) are expected (Fig. 2).

For strain to localize in the ductile regime, potentially leading to the development of shear zones, strain softening has to occur in the deforming material (Poirier, 1980; White et al., 1980). A multitude of mechanisms have been proposed to cause strain softening in materials deforming by intracrystalline plasticity: 1) grain size reduction by dynamic recrystallization and/or brittle comminution, 2) development of textures (crystallographic preferred orientations, CPO) and/or shape preferred orientations (including foliations)

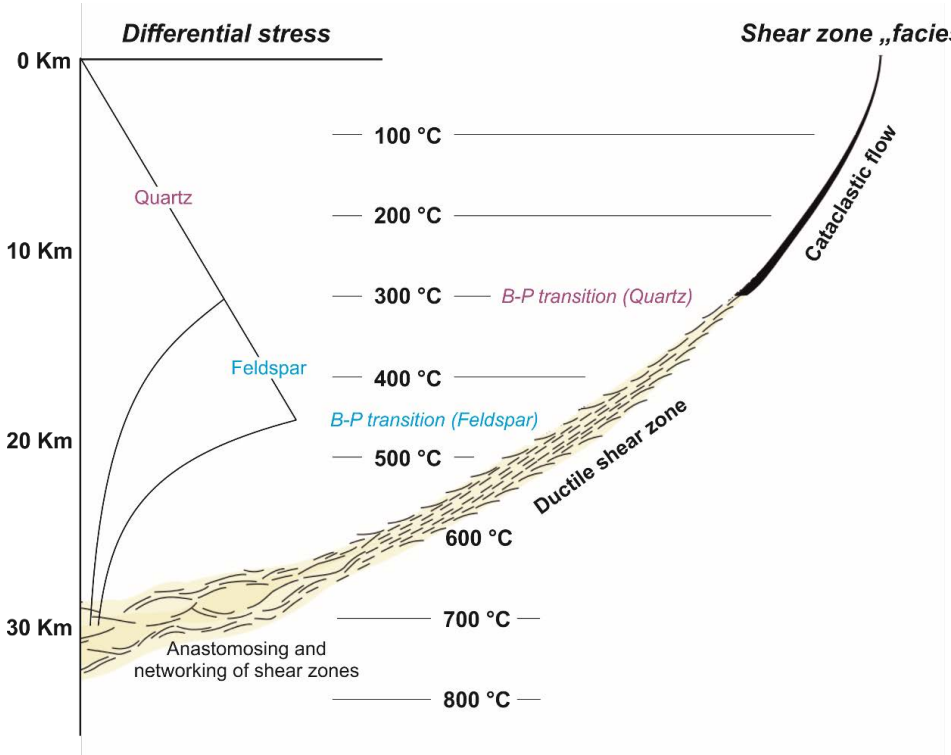

Figure 2: (modified from *Fig. 3* in Fossen and Cavalcante (2017)); simplified scheme relating the evolution of shear zone "facies" with depth and flow laws for the two main components of upper and lower crust. Brittle-Plastic transitions for (wet) quartz and feldspar are indicated in the graph.

causing geometric softening, 3) metamorphic reactions producing weaker mineral phases, 4) fluid influx inducing dissolution-precipitation or the reduction of effective pressure, leading to brittle deformation, and 5) shear heating leading to locally higher temperatures (for a review of these processes, see Burlini & Bruhn, 2005). One dominant or a combination of these mechanisms evolving with progressive strain are likely to occur in nature during the nucleation and growth phase of high temperature shear zones. Recently, Hansen et al. (2012) suggested that the style of loading (constant load or constant deformation rate) can also affect the efficiency of ductile strain localization in monomineralic aggregates.

Pioneering work on the topic lead to the assumption that pre-existing stratification of weaker and stronger lithologies (Ranalli & Murphy, 1987) or the presence of mechanically weaker inclusions within a stronger matrix (Kirby, 1985) are necessary for the nucleation of localized strain. At the brittle-to-ductile transition, brittle precursors are shown to play a key role in the creation of planes of structural heterogeneity that get exploited by subsequent ductile deformation and become the nuclei of localized strain (e.g., Austrheim, 1987; Mancktelow & Pennacchioni, 2005; Fusseis et al., 2006; Pennacchioni & Mancktelow, 2007; Fusseis & Handy, 2008). Ductile fracturing (e.g., cavity coalescence, Dimanov et al. (2007), Rybacki et al. (2008), (2010); high P-T fracturing along cleavage planes, Menegon et al. (2013)) can be responsible for increased porosity (leading to fluid influx) and/or for brittle comminution producing fine grained material that can deform in the diffusion creep regime. Purely crystal-plastic deformation mechanisms (grain bound-

ary sliding, dissolution-precipitation) are thought to lead to increased porosity (creep cavitation) that can create a syn-deformation dynamic influx of fluid (Fusseis et al., 2009). While most of these mechanisms involve the weakening influence of deformation fluids, simple rheological contrast between different components is also shown to produce the conditions for strain to localize (e.g., lithologic boundaries, Pennacchioni and Mancktelow (2007); pseudotachylites creating a surface heterogeneity, Pittarello et al. (2012); randomly distributed weak particles in a stronger matrix, Mancktelow (2002)).

1.3 High-temperature rock deformation: the experimental approach

Experimentally derived flow laws are to a large extent based on investigations conducted in a Paterson-type deformation apparatus, which is one of the earliest to use gas as a confining medium (Paterson, 1970). The apparatus can reach temperatures as high as $\approx$ 1300 °C and confining pressures up to $\approx$ 500 MPa, while the strain rates vary between about 10^{-7} and 10^{-3} s^{-1}. Experiments can be carried out in conditions of constant deformation rate and/or constant load. At higher confining pressures, deformation tests are commonly performed using a Griggs-type apparatus, where the pressure medium consists of solid or molten salt. However, the accuracy of stress measurements is limited for this type of machines because the load cell is placed outside of the pressure vessel. Experiments performed in the Paterson apparatus have been the basis for the definition of constitutive laws and deformation mechanism maps for feldspar rocks in Dimanov et al. (1999), Rybacki and Dresen (2000) and Rybacki and Dresen (2004), Rybacki et al. (2006). With the addition of the torsion set-up to the apparatus, experiments in simple shear could be conducted up to large shear strains that are more representative of natural conditions (e.g., Bystricky et al., 2000; Mei & Kohlstedt, 2000; Pieri, Burlini, et al., 2001; Pieri, Kunze, et al., 2001; Rybacki et al., 2003; Schmocker et al., 2003; Barnhoorn et al., 2004).

1.3.1 Previous experiments on ductile strain localization

High strain experimental rock deformation conducted in the Paterson apparatus in torsion mode allowed for the extensive investigation on the topic of strain localization in the ductile regime. A number of studies conducted on monomineralic materials (e.g., Pieri, Burlini, et al. (2001) and Pieri, Kunze, et al. (2001); Barnhoorn et al. (2004) on calcite; Bystricky et al. (2000) on olivine; Rybacki et al. (2008) on feldspar; Wenk et al. (2009) on halite) show little to no strain localization (unless creep cavitation and porosity bands are formed, ultimately leading to ductile failure, Rybacki et al., 2008, 2010), although for olivine constant stress loading conditions seem to favour localization compared to constant strain rate (Hansen et al., 2012). Polyphase rocks are generally expected to be more likely undergoing strain localization due to the interaction between constituents, for

example due to metamorphic reactions or different rheological behaviour leading to stress inhomogeneity. Therefore, experimental deformation of two-phase aggregates has been conducted extensively, revealing a more common occurrence of strain localization (e.g., Ji et al., 2004; Barnhoorn, Bystricky, Kunze, et al., 2005; Delle Piane et al., 2007, 2009), although rather homogeneous microstructures are observed if the phases both deform in the dislocation creep regime (e.g., Rybacki et al., 2003; Bystricky et al., 2006).

The experimental configuration employed in this project was previously tested in a study investigating the effect of single inclusions of either lower or higher viscosity than the surrounding matrix on the bulk behaviour of the aggregate (Rybacki et al., 2014). Also conducted in a Paterson deformation apparatus, both triaxial and torsion experiments were run on samples of Carrara marble matrix containing inclusions of either weaker Solnhofen limestone or stronger novaculite (a very dense and homogeneous quartz rock; Wenk et al., 2006), deformed at high temperature and confining pressure conditions. Results showed that weak inclusions promoted strain localization in the matrix and a lower aggregate strength, while the effect of strong inclusions was negligible and no microstructure indicative of localized strain was observed.

1.3.2 The carbonate system as an experimental material

Calcite-rich rocks are often used in experimental rock deformation (e.g., Griggs & Miller, 1951; Rutter, 1972; Wenk et al., 1973; Rutter, 1974; Rutter et al., 1994; Schmid et al., 1977; Pieri, Burlini, et al., 2001; Pieri, Kunze, et al., 2001; Barnhoorn et al., 2004; Barnhoorn, Bystricky, Burlini, & Kunze, 2005). An abundant mineral on the Earth's surface, calcite that deforms plastically at lower temperatures than most other main lithosphere components. Characteristic deformation microstructures and textures are produced in calcite at different pressures and temperatures, allowing to relate post-mortem structures to specific regimes of plastic deformation.

Among the most utilized calcite-rich experimental materials are two natural lithologies of remarkable purity, Carrara marble and Solnhofen limestone. Carrara marble is a highly pure metamorphic calcite rock that has been quarried in central Italy for centuries. It is composed nearly entirely of calcite (up to 98%, Pieri, Burlini, et al., 2001) and has virtually no effective porosity ($\approx$ 0.1%, Rutter, 1972). The grain size is very coarse, on the order of $\approx$ 0.2 mm and it is characterized by very homogeneous microstructure and texture, with very little stored strain (Rutter, 1972; Pieri, Burlini, et al., 2001) and only a small amount of twins. Grain boundaries are generally straight and form abundant 120° triple junctions, indicative of static recrystallization.

Solnhofen limestone is a very fine-grained material containing up to 98% calcite, which has been also extensively tested in experimental rock deformation (e.g., Wenk et al., 1973; Schmid et al., 1977; Casey et al., 1998; Llana-Fúnez & Rutter, 2008). With an average grain size on the order of $\approx$ 5 to 20 μm, Solnhofen limestone can be deformed in the

grain size sensitive creep regime at conditions of high temperature and pressure. Effective porosity is relatively low, estimated on the order of 1 to 5%, with a dependency on the location of sampling (Rutter, 1972). The presence of up to 4% of impurity phases (quartz and clay) at the grain boundaries (Rutter et al., 1994) is likely to cause substantial second-phase pinning that inhibits grain growth both during deformation and annealing.

1.3.3 Natural shear zones in carbonates

Calcite-rich rocks, of sedimentary and metamorphic origin, are abundant at the Earth's surface and within the deeper levels of the lithosphere. Because of the relative weakness of calcite relative to most of the other abundant rock-constituents, carbonates are often the locus for ductile strain localization within, for example, orogenic nappe complexes.

The Glarus Thrust, in eastern Switzerland, is an example of a large structure accommodating regional displacements of up to $\approx$ 50 km (Pfiffner, 1985) and mainly involving carbonates of Mesozoic age. Strongly foliated calc-mylonites and synkinematic calcite veins characterize the exposed thrust surface, while microstructural and textural investigations reveal a gradient in the deformation conditions both along the thrust and due to the superimposition of retrograde conditions (Ebert et al., 2007, and references therein).

In Switzerland, the Morcles nappe, within the alpine Helvetic nappe complex, is a recumbent fault composed of mostly carbonatic lithologies from a shallow-water basin of Jurassic and Cretaceous age. During the Alpine orogeny, the area was subjected to closure and inversion of the marine basin, with overthrusting of the whole nappe system on top of the Aiguille Rouge Massif. A basal thrust zone formed in the carbonatic units with the development of meso-scale shear zones accommodating a total displacement of the nappe in the order of 10-12 km (Austin et al., 2008, and references therein).

Other examples include Triassic to Early Cretaceous limestones within the Agly Massif in the north-eastern Pyrenees that are strongly mylonitized and appear to be associated with pre-orogenic exhumation of the massif, accommodating the regional extension that led to the formation of the Boucheville basin in the Late Cretaceous (Vauchez et al., 2013). Other similar examples can be found in a multitude of crustal scale deformation settings. Kennedy and White (2001) collected and compared samples from thrusting systems developing within carbonate-rich lithologies in the Canadian Rocky Mountains and in Virginia (USA).

1.4 Outline of the thesis

The current thesis is mostly based on experimental work, combined with numerical modelling that was aimed at reproducing one of the configurations tested in the experiments.

Chapter 2 deals with the effect of loading conditions on the initiation and evolution of localized shear zones induced by the presence of a material heterogeneity in a homogeneous matrix. A series of torsion experiments were conducted on samples of Car-

rara marble (matrix material) containing a single planar inclusion of mechanically weaker Solnhofen limestone. High temperature (900 °C) and high confining pressure (400 MPa) were employed, conditions placing the coarse-grained Carrara marble in the dislocation creep regime, while the Solnhofen limestone is likely to deform by diffusion creep. The experiments were run at either constant twist rate (deformation rate) or constant torque (stress), with the aim of investigating potential differences in the amount and efficiency of strain localization between different loading conditions.

Chapter 3 presents results from a numerical modelling study that reproduces the experimental configuration and mechanical behaviour presented in **chapter 2**. Introducing a simple strain softening law to the model, the stress-strain curves and final distribution of strain from the experiments can be reproduced with a high degree of accuracy. Benchmarking models capable of mimicking weakening processes is of great importance for the reliability of numerical modelling techniques reproducing crustal scale processes.

Chapter 4 displays results from a series of triaxial experiments investigating the interplay between brittle and ductile deformation in contractional and extensional step-over regions between planar inclusions within a homogeneous matrix. The combination of Carrara marble and Solnhofen limestone was again employed, this time with two inclusions inclined at 45° to the long axis of the cylindrical sample, forming step-over geometries of different kinematic nature (extensional or compressional). Varying confining pressures (30, 50, 100 and 300 MPa) were applied to the high temperature (900 °C) runs to induce diverse degrees of brittle deformation and examine the effect on the intervening ductile processes and the overall impact on strain localization. In this sense, the configuration employed mimics the frequent occurrence, in nature, of brittle precursors facilitating the nucleation of ductile shear zones (see ***section 1.2.2***).

Chapter 5 will be discussing and summarizing the main conclusions and implications of the studies here presented, while **chapter 6** will outline the potential prospects of future investigations within the topic of high temperature strain localization.

2 High-temperature shear zone formation in Carrara marble: The effect of loading conditions

Summary

Rock deformation at depths in the Earth's crust is often localized in high temperature shear zones occurring at different scales in a variety of lithologies. The presence of material heterogeneities is known to trigger shear zone development, but the mechanisms controlling initiation and evolution of localization are not fully understood.

To investigate the effect of loading conditions on shear zone nucleation along heterogeneities, we performed torsion experiments under constant twist rate (CTR) and constant torque (CT) conditions in a Paterson-type deformation apparatus. The sample assemblage consisted of cylindrical Carrara marble specimens containing a thin plate of Solnhofen limestone perpendicular to the cylinder's longitudinal axis. Under experimental conditions (900 °C, 400 MPa confining pressure), samples were plastically deformed and limestone is about 9 times weaker than marble, acting as a weak inclusion in a strong matrix. CTR experiments were performed at maximum bulk shear strain rates of $\approx 2\times10^{-4}$ s^{-1}, yielding peak shear stresses of $\approx$ 20 MPa. CT tests were conducted at shear stresses of $\approx$ 20 MPa resulting in bulk shear strain rates of $1\text{-}4\times10^{-4}$ s^{-1}. Experiments were terminated at maximum bulk shear strains of $\approx$ 0.3 and 1.0.

Strain was localized within the Carrara marble in front of the inclusion in an area of strongly deformed grains and intense grain size reduction. Locally, evidences for coexisting brittle deformation are also observed regardless of the imposed loading conditions. The local shear strain at the inclusion tip is up to 30 times higher than the strain in the adjacent host rock, rapidly dropping to 5 times higher at larger distance from the inclusion. At both bulk strains, the evolution of microstructural and textural parameters is independent of loading conditions. Our results suggest that loading conditions do not significantly affect material heterogeneity-induced strain localization during its nucleation and transient stages.

2.1 Introduction

Localization of deformation in the deep crust and mantle is a key mechanism involved in the formation of tectonic plates and mountain belts on our planet (Tackley, 2000; Schubert et al., 2001; Bercovici & Karato, 2002; Bercovici, 2003; Regenauer-Lieb & Yuen, 2003, 2004). Therefore, the knowledge of how deformation is accommodated at plate boundaries and orogenic belts requires the understanding of physical processes that govern localized deformation in the ductile regime and its persistence over geological times. A multitude of mechanisms have been proposed to be responsible for nucleation of localized deformation in the middle to lower crust, under the generally accepted premise that a dynamic

(positive) feedback mechanism is required to induce thermo-mechanical perturbances in otherwise homogeneously deforming mediums (Bercovici, 1996, 1998; Bercovici & Karato, 2002; Regenauer-Lieb & Yuen, 2003). Grain size reduction by dynamic recrystallization (e.g., Montési & Hirth, 2003; Kilian et al., 2011; Platt & Behr, 2011b), fluid influx inducing metamorphic reactions (e.g., Fusseis & Handy, 2008), development or pre-existence of a crystallographic preferred orientation (e.g., Michibayashi & Mainprice, 2004; Tommasi et al., 2009), ductile fracturing (e.g., Handy & Stünitz, 2002; Dimanov et al., 2007; Rybacki et al., 2008; Menegon et al., 2013) and the presence of material heterogeneities (e.g., Rybacki et al., 2014) are only some of the mechanisms that were recognized in the field and through experimental work as factors causing rheological weakening and subsequent ductile localization of strain (see Burlini & Bruhn, 2005, for a review). A number of experimental investigations at constant strain rate have failed to produce notable localization in monophase materials in the ductile regime even at very high strains (e.g., Bystricky et al., 2000; Ter Heege et al., 2002; Barnhoorn et al., 2004). Some observations suggest that constant stress loading conditions appear to initiate localization in highly deformed olivine aggregates (Hansen et al., 2012). However, the effects of material properties and boundary conditions on the mechanical and microstructural evolution associated with strain localization and weakening are not yet understood and only a few experimental studies have addressed this. So far, the effect of the imposed loading conditions on the efficiency of localization within homogeneous materials has largely been investigated in theoretical models (Fressengeas & Molinari, 1987; Leroy & Molinari, 1992; Paterson, 2007) but experimental studies of ductile localization induced by some of the aforementioned mechanisms of rheological weakening have not yet been performed. In nature, calcite-rich rocks are known to host localized shear zones developed in the high temperature ductile regime, leading to the formation of large scale shear zones where up to tens of kilometres of displacement are accommodated (e.g. the Glarus Thrust in the Helvetic Nappe, Groshong Jr et al., 1984; Herwegh & Kunze, 2002; Ebert et al., 2007). Calcite and natural carbonate materials have been extensively studied in the ductile regime both experimentally (e.g., Schmid et al., 1980; Rutter et al., 1994; Rutter, 1995; Pieri, Burlini, et al., 2001; Pieri, Kunze, et al., 2001; Barnhoorn et al., 2004) and in the field (Schmid et al., 1981; Bestmann et al., 2000; Rogowitz et al., 2014, 2016), so that the calibration of mechanical, microstructural and textural data for calcite at different deformation conditions is well established. In this contribution, we experimentally investigate the effects of different loading conditions (constant stress versus constant strain rate) on the nucleation and evolution of heterogeneity-induced high temperature shear zones in a carbonate system. It is important to anticipate that the phenomena investigated in the present study are inherently transient, as they mimic the nucleation stage of shear zone formation and its progressive propagation within intact material. Therefore, the loading condition may affect the shear zone evolution, which is in contrast to the commonly assumed path-independency of steady state deformation treated as being in thermodynamic

equilibrium.

2.2 Experimental setup

The torsion experiments presented here were carried out on mono-mineralic calcite aggregates consisting of Carrara marble with elongated Solnhofen limestone inclusions. A thin (0.75 mm) circle segment of Solnhofen limestone with an arc length of about 11.8 mm was inserted in a saw-cut slot in a hollow cylinder (10 mm height, 15 mm outer diameter, 6.1 mm inner diameter) of Carrara marble. Ceramic glue was used to fill up the possible gaps in the slot. Two alumina spacers (for protection of the pistons in the deformation apparatus) and a solid gold cylinder inserted in the inner borehole of the sample completed the setup (Fig. 3).

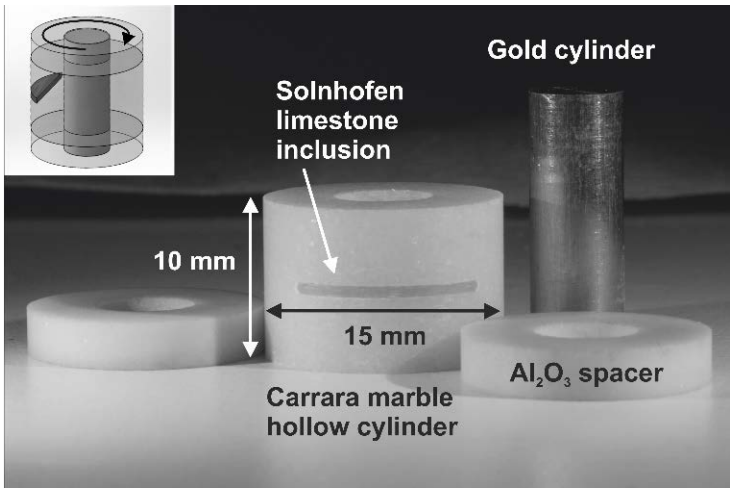

Figure 3: Elements of the sample assembly. In the small inset, the setup prior to insertion in the copper jacket; indicated is the direction of the applied torsion.

The hollow cylinder configuration was preferred as it guarantees a relatively homogeneous distribution of shear stress within the sample (Paterson & Olgaard, 2000). Carrara marble is a largely used material in experimental rock deformation due to its exceptional purity (> 99% $CaCO_3$) and low to no initial porosity (Rutter, 1995; Pieri, Burlini, et al., 2001; Pieri, Kunze, et al., 2001; Ter Heege et al., 2002; Barnhoorn et al., 2004; De Bresser et al., 2005). The undeformed marble shows a uniform grain size distribution with an average grain size on the order of the hundreds of microns ($\approx$ 150 μm), abundant triple junctions, straight grain boundaries and a quasi-uniform crystallographic orientation distribution (see ***section 2.4.3*** and figures therein). Twinned crystals are present, but the twins are extremely thin (< 5 μm), straight and not pervasive; these types of twins are commonly interpreted as late features typical of a low temperature natural environment (Burkhard, 1993; Ferrill et al., 2004). Solnhofen limestone is an extremely fine grained ($\approx$ 5 μm average grain size) almost pure calcite rock (more than 97 wt.% calcite, Rutter, 1972), which has been long used as a standard material for experimental deformation of natural fine-grained calcite (e.g., Rutter, 1972; Rutter & Schmid, 1975; Schmid et al.,

1980, 1987; Casey et al., 1998). As a consequence of a large difference in initial grain size, Solnhofen limestone is up to 9 times weaker than Carrara Marble at the imposed experimental conditions of 900 °C temperature and 400 MPa confining pressure (e.g., Rybacki et al., 2014). As a result, the Solnhofen limestone inclusion and Carrara marble host introduce a large viscosity contrast in the experimental setup.

Experiments were performed in a Paterson-type gas deformation apparatus equipped with a torsion actuator (Paterson & Olgaard, 2000). Prior to experimental runs, the samples were inserted into copper jackets of ≈ 0.2 mm thickness (to isolate them from the gas confining pressure medium) the strength of which is accounted for in the evaluation of the mechanical data. The samples were first pressurized to 400 MPa, followed by heating at a rate of ≈ 30 °C/min up to the desired temperature of 900 °C (with accuracy of ± 2 °C along the sample axis). After test termination, the load imposed by the actuator was maintained constant during cooling (at equal rate to the heating phase) to preserve deformation microstructures and to reduce the amount of static recovery occurring within the samples.

Following Paterson and Olgaard (2000), the measured torque M was converted to maximum shear stress τ at the periphery of the sample cylinder according to the equation:

$$\tau = \frac{4M(3+\frac{1}{n})}{\pi} \frac{D_0^{\frac{1}{n}}}{D_0^{3+\frac{1}{n}} - D_i^{3+\frac{1}{n}}} \tag{1}$$

where D_0 and D_i are the external and internal diameters of the cylinder, respectively. Measured displacement rate $\dot{\theta}$ in radians is converted to maximum shear strain rate $\dot{\gamma}$ according to the following:

$$\dot{\gamma} = \frac{D_0 \dot{\theta}}{2l} \tag{2}$$

where D_0 is the external diameter of the sample and l is the length of the cylindrical specimen.

2.3 Analytical methods

Thin sections were produced for microstructural and textural investigations. To ensure the analyses were carried out on the portion of the sample that experienced the highest (measured) strain, the sections were cut tangentially to the outer rim and parallel to the longitudinal axis of the cylinders (after Paterson & Olgaard, 2000). The thin sections were polished in two steps, first with diamond paste up to 0.25 μm grain size followed by 2 hours of chemical-mechanical polishing with an alkaline solution of colloidal silica. To investigate the crystallographic orientation of the calcite grains, all thin sections were examined with the electron back-scattered diffraction (EBSD) technique on a FEI Quanta 3D FEG dual beam machine equipped with an EDAX-TSL Digiview IV EBSD detector and the TSL software OIM 5.31 for the acquisition of diffraction patterns. EBSD analyses

were performed on uncoated samples under low vacuum conditions (10 Pa H_2O) using an accelerating voltage of 15 kV and beam current of 8 nA at variable working distances between 13 and 16 mm.

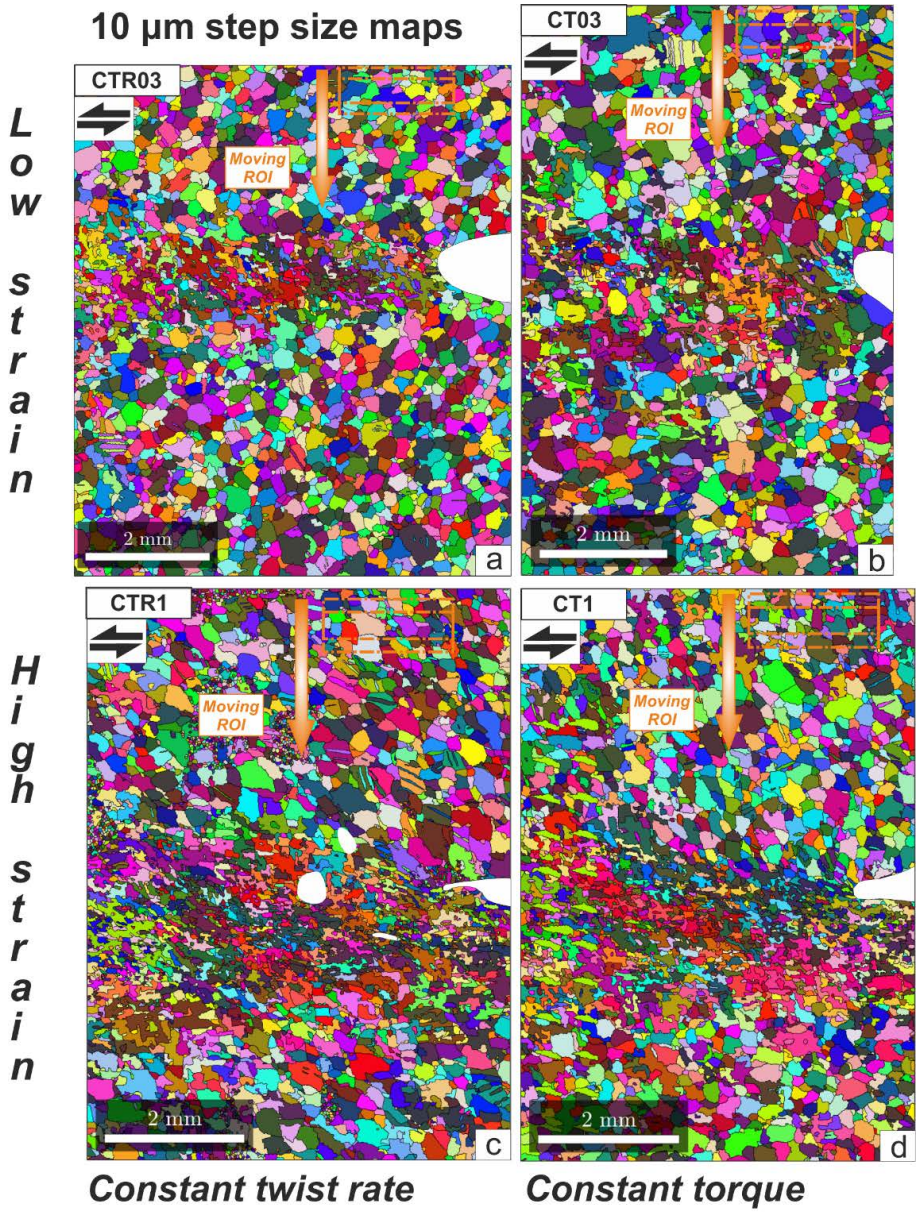

Figure 4: 10 μm step size orientation maps from EBSD data, used for the construction of grain size profiles across the thin sections (in orange, the partially overlapping moving region of interest, ROI). In a and c the constant twist rate samples and in b and d the constant torque ones. Color coding represent IPF (inverse pole figure); the white patches in c are patches of misoriented data due to damages in the thin section.

Crystallographic orientation mapping was performed systematically in all samples using two different step sizes (10 μm and 3.5 μm). The coarser step size map was used to map the orientations of the whole sample and for the construction of mean grain size profiles across the thin sections (top to bottom; orange rectangles in Fig. 4a-d). The fine step size mapping was limited to the area in front of the limestone inclusion, where deformation in the marble localizes (Fig. 5a-d); these maps were used for the study of shape descriptors (***section 2.4.4***) and their variations within regions in and outside of the localized zone in front of the inclusion (red rectangles in Fig. 5a-d).

Clean-up of the raw data was carried out using the TLS software OIM Analysis 7.3, with standardization of the confidence index (CI) within grains. Individual grains were defined using the following parameters: minimum grain tolerance angle of 10° (misorientation angle between neighbouring points) and a minimum of 10 indexed points per grain. Following this step, a CI correlation between neighbour points was applied to the datasets with low CI (< 0.1) points reassigned to the orientation and CI of the neighbour data point with the highest CI within individual grains. To identify very small (dynami-

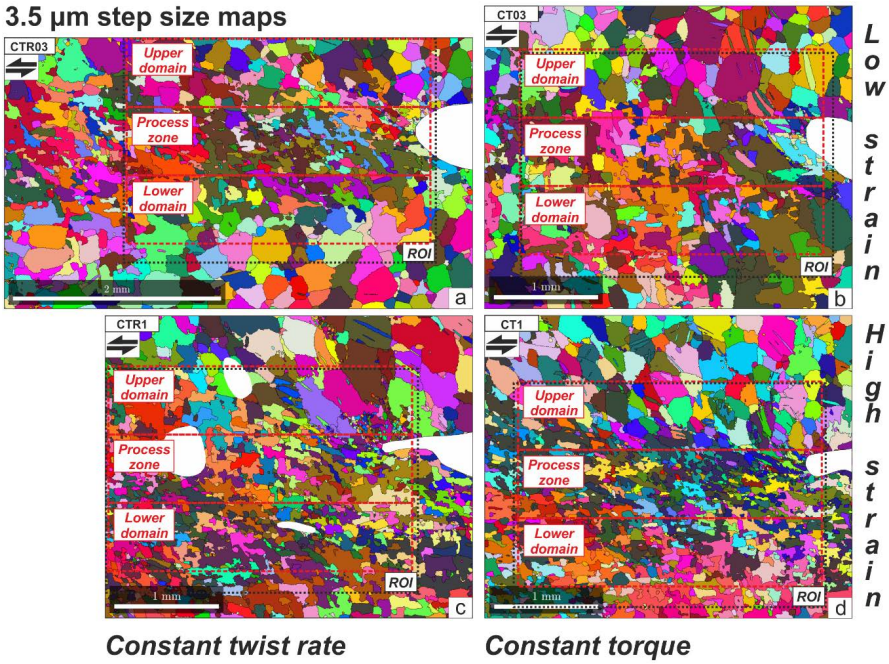

Figure 5: Location of regions of interest for different data extractions on 3.5 μm step size orientation maps from EBSD data. Two types of areas (red and black) are considered for different calculations. In a and c the constant twist rate samples, in b and d the constant torque ones. Color coding represent IPF (inverse pole figure); the white patches in c are patches of misoriented data due to damages in the thin section.

cally recrystallized) grains and their spatial distribution, a minimum of 5 indexed points per grain criterion (to reduce the loss of small grains by interpolation and smoothing) was used in the finer stepping size maps within a region of interest (Fig. 5a-d, black rectangles). Unless otherwise specified, grain sizes are expressed as equivalent diameter (diameter of a circle of equivalent area to the grain).

Calculations on the EBSD data were performed using the MTEX 4.3.2 toolbox for Matlab (Hielscher & Schaeben, 2008; Bachmann et al., 2010). Orientation distribution function and pole figure contouring were calculated using a Gaussian half-width of 10° and a maximum harmonic expansion factor of 32.

Grain size evolution across the samples (see ***section 2.4.4***) was investigated using the coarser EBSD maps (10 μm step size). A moving, partially overlapping (one third of the vertical size) window of size 1.85×0.5 mm (Fig. 4a-d) was used to extract data along a profile parallel to the longitudinal axis of the sample cylinder located directly in front of the limestone inclusion in the Carrara marble. Grains transected by the boundary of the moving window were excluded from the calculations. For each window, we estimated

the average grain size using the RMS (root mean square) value of the distribution.

To characterize grain shape evolution within the area covered by the finer step size maps (***section 2.4.4***), two shape descriptors were considered. First, the inverse aspect ratio (according to the definition of the MTEX toolbox, Hielscher and Schaeben (2008): $IAR = \frac{w}{l}$, w and l being the width and length of the particle, respectively) and secondly a variation of the classical circularity shape factor, defined as follows:

$$Circ = \frac{4\pi A}{P^2} \tag{3}$$

where A is the area and P the perimeter of a grain (Heilbronner & Barrett, 2013). Both shape descriptors assume values between 1 and 0, where the former represents a circle (maximum IAR) with smooth surfaces (maximum circularity) and the latter is characteristic of an infinitely non-circular shape (minimum IAR) with infinitely rough surfaces (minimum circularity).

For the study of shape descriptors, a grain size filtering was applied to the datasets in order to remove small grains produced by dynamic recrystallization, which are expected to approach the ideal circular shape at the time of formation. The size filter was set to 20 μm, which is the average grain size of dynamically recrystallized grains determined by optical microscopy.

Six transmission electron microscopy foils (0.15 μm in thickness) from a single thin section (sample CTR03) were prepared using the focused ion beam technique (e.g., Wirth, 2005) and subsequently inspected with transmission electron microscopy (TEM) on a FEI Tecnai G2 F20 X-Twin TEM for the calculation of dislocation densities (see ***section 2.4.5***).

2.4 Results

2.4.1 Mechanical data

We present the results from four experiments, two of which were run at constant twist rate and two at constant torque conditions (CTR and CT, respectively, equivalent to constant strain rate and constant stress) in the torsion setup of a Paterson-type gas deformation apparatus. The final bulk strains reached in the experiments are $\gamma \approx 0.3$ and $\gamma \approx 1$, respectively, for both loading configurations. Experimental conditions for the four samples presented here are shown in Table 1.

In CTR experiments (Fig. 6a), shear stress is plotted against bulk shear strain, while for CT experiments (Fig. 6b), shear strain rate is plotted versus bulk shear strain in semi-logarithmic scale. In constant twist rate experiments, measured peak shear stresses of about 19 MPa at the periphery of the samples are reached at low values of bulk shear strain ($\gamma \approx 0.15$), after which mechanical softening occurs and a gradual weakening of the samples can be observed up to the maximum bulk strains reached, $\gamma = 0.29$ for

Sample number	**P [MPa]**	**T [°C]**	**Test type**	$\dot{\gamma}$ [s^{-1}]	τ [MPa]	γ_{max}	γ_{sec}
CTR03	400	900	Torsion	1.8×10^{-4}	20.1	0.293	0.2
CT03	400	900	Torsion	2.1 - 2.4 $\times 10^{-4}$	19.8	0.29	0.2
CTR1	400	900	Torsion	1.9×10^{-4}	19.7 - 17.6	0.99	0.68
CT1	400	900	Torsion	1.2 - 4.0 $\times 10^{-4}$	18.8 - 18.4	0.94	0.65

Table 1: Experimental conditions for the four samples examined. CTR is constant twist rate (strain rate) experiments, CT constant torque (stress), $\dot{\gamma}$ is shear strain rate (in s^{-1}), γ_{max} is maximum bulk shear strain and γ_{sec} is the local shear strain in a section of radius r_{sec}.

sample CTR03 and $\gamma = 0.99$ for sample CTR1. For constant torque experiments, the applied torque was set so that the shear stress at the periphery of the samples is $\approx$ 19 MPa, similar to the maximum stress measured in constant twist rate tests. Bulk shear strain rates first decreased rapidly due to elastic loading, followed by a gradual decrease up to a minimum at $\gamma \approx$ 0.1-0.2. Subsequently, strain rates increased corresponding to mechanical weakening of the samples up to a factor of about 4 at $\gamma = 1$ (Fig. 6b). The slightly higher minimum strain rate of sample CT03 compared to CT1 is related to the higher initially applied stress (Tab. 1).

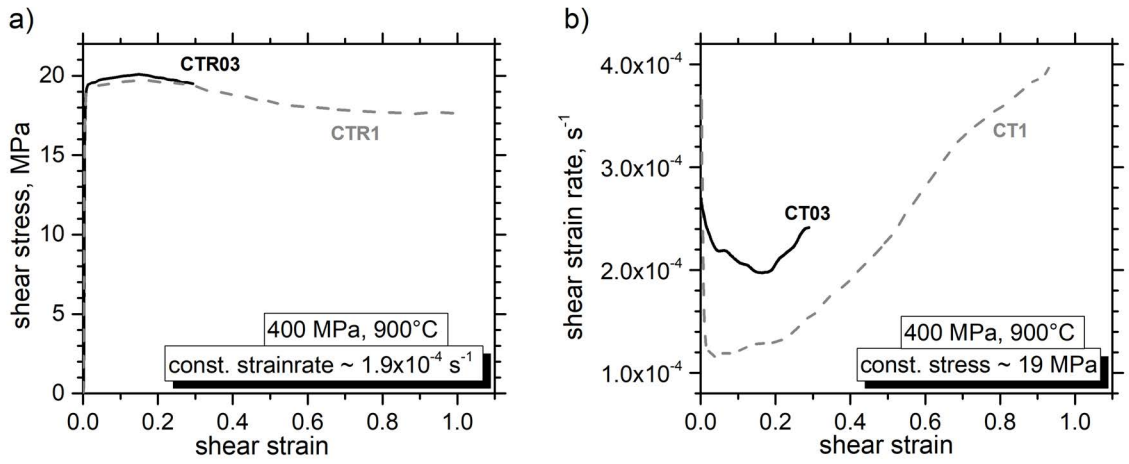

Figure 6: Mechanical shear stress-strain curves of torsion experiments performed at constant twist rate (a) and constant torque (b).

2.4.2 Strain localization

In order to quantify the local distribution of shear strain within the samples, passive strain markers were applied to the copper jackets prior to the experimental runs (except for sample CTR03). A grid of evenly spaced straight lines, parallel to the cylinder axis, was carved in the copper jacket (Fig. 7; with denser spacing applied to the area where the inclusion is) and recovered after the experiments. The locally imposed shear strain is

estimated from the angular deflection of the originally straight lines. After deformation, the distribution of those lines is clearly heterogeneous and reflects the partitioning of strain between the limestone inclusion and the Carrara marble.

In particular, a substantial difference in shear strain can be observed between the region

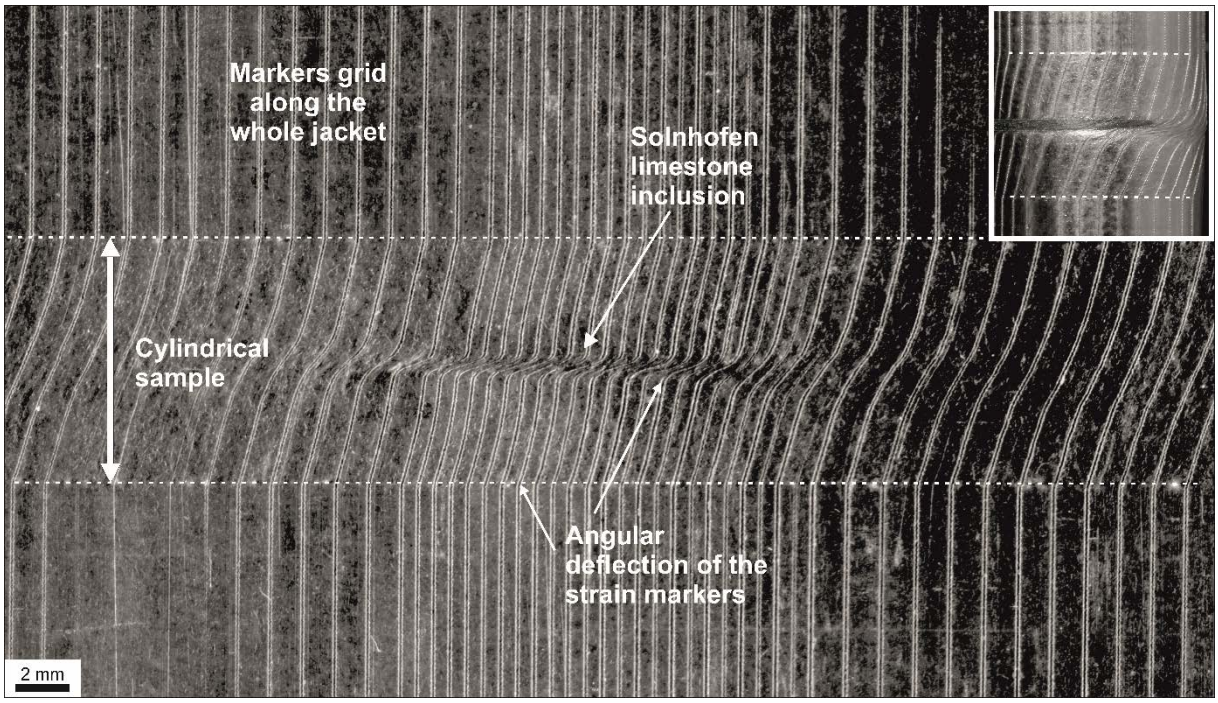

Figure 7: Example of the strain markers grid as applied on the copper jacket, recovered after the experimental run.

directly in front of the Solnhofen inclusion and the surrounding matrix, indicative of ongoing strain localization within the Carrara marble itself, related to the presence of a nearby material heterogeneity.

Local shear strains are calculated for this area of incipient localized deformation (named hereafter the process zone) and for the less deformed matrix at some distance from the inclusion tip. A strongly localized shear strain in front of the inclusion is observed (up to a factor ≈ 12 compared to the imposed bulk strain), rapidly decaying to background strain level with distance (≈ 10 mm) from the inclusion (Fig. 8a). The degree of strain localization (i.e. the ratio between local to bulk shear strain) is not substantially different between the two loading conditions of constant twist rate or constant torque (cf., samples CTR1 and CT1, respectively), especially when one considers the large uncertainty in the calculated local strains when the angular deflection is large and the measurements become less accurate (a 3° variation can lead to a difference in γ of 10). In Figure 8b the local strain measured in the process zone is normalized to that of the surrounding, less deformed matrix, plotted against distance from the inclusion tip in the lateral dimension. The localization of deformation in the process zone with respect to the adjacent matrix is higher by a factor $\approx$ 2-3 than with respect to the bulk strain (Fig. 8a). Clearly, the degree of localization is further developed at higher total bulk strain (samples CTR1 and CT1, as opposed to sample CT03). Again, no substantial difference is noticed between

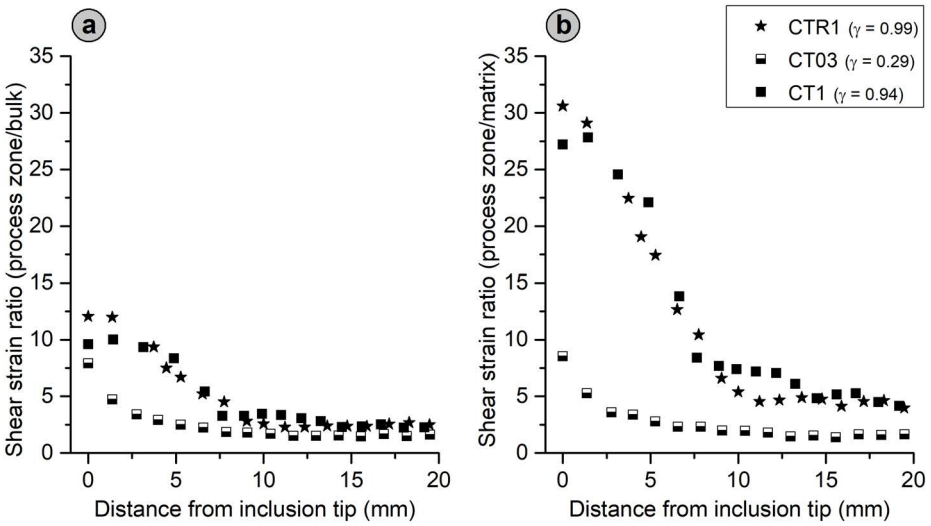

Figure 8: Local shear strain evolution with distance from inclusion tip. a) Normalized local shear strain ($\gamma_{processzone}$ / γ_{bulk}); b) local shear strain ratio, $\gamma_{processzone}$ / γ_{matrix}.

constant stress and constant strain rate samples.

2.4.3 Microstructures

In composite micrographs from optical microscopy images we typically observe an area of intense grain size reduction and highly deformed grains in the Carrara marble matrix, close to the Solnhofen limestone inclusion (Fig. 9a-b and f-g). In contrast, the surrounding matrix region remains almost undeformed, and equant grains display similar characteristics to the undeformed Carrara marble (Fig. 7k-m). Note that the bulk shear strain indicated on the micrographs refers to the maximum measured shear strain. Approximate local shear strain γ_{sec} within a section of the sample cylinder cut at a radius r_{sec} is about 30% lower (Tab. 1), determined by:

$$\gamma_{sec} = \frac{r_{sec}}{r}\,\gamma_{max} \tag{4}$$

In all micrographs the Solnhofen limestone inclusion is located on the right side, showing at higher strain stronger distortion from the original undeformed rectangular shape (Fig. 3). In the low strain samples (CTR03 and CT03, $\gamma \approx 0.3$; Fig. 9a and f) the process zone, represented by the area of intense localized deformation in front of the inclusion tip, is characterized by intense twinning, with grains often developing two distinct sets of twins oriented at $\approx 60°$ to each other (Figs. 9c and 9h-i). Bending and tapering of twin sets can be observed in several cases (arrows in Fig. 9c and i). After Burkhard (1993) and Ferrill et al. (2004), twins are identified as predominantly type 2 and 3, with some remnants of type 1 twins mainly at a distance from the inclusion. Undulose extinction and lobate grain boundaries (arrows in Figs. 9c-d and Figs. 9h-i) are pervasive, indicating active crystal plasticity and intracrystalline deformation mostly by dislocation glide. Grain size reduction by dynamic recrystallization is incipient in the process zone of the low strain

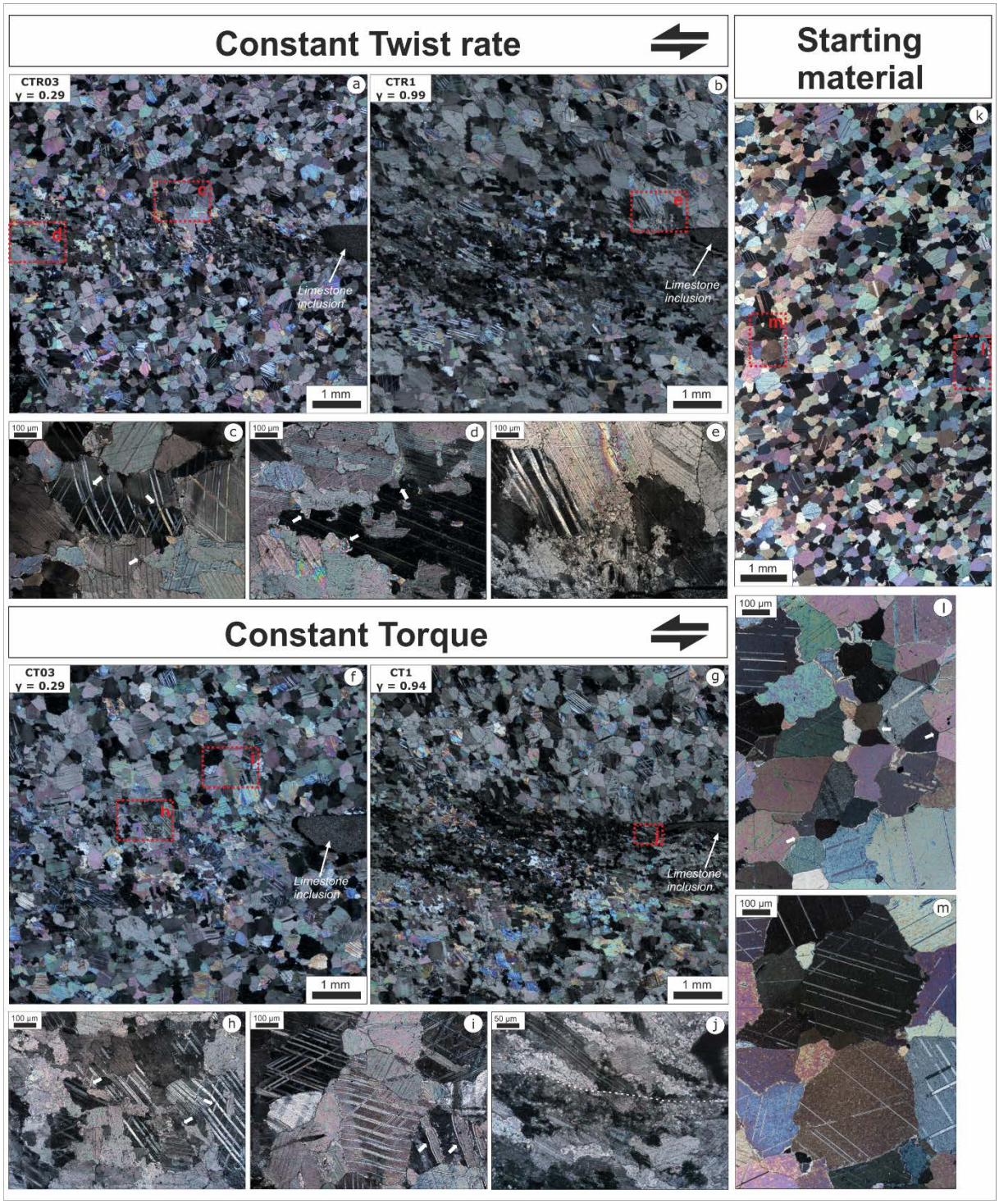

Figure 9: Optical micrographs of 5 thin sections (four from the experimental runs and one from the undeformed starting material), and small insets (c-e, h-j and l,m) displaying details of the microstructures; insets c and d are areas of sample CTR03, e is from sample CTR1, f and g from CT03 and h from CT1. The undeformed starting material displays a homogeneous microstructure with little to no stored strain, large equant grains and abundance of triple junctions (l); twin sets are thin and straight (m). In the overview micrographs of the deformed samples (a-b and f-g), a strongly inhomogeneous distribution of strain can be observed, with the incipient (CTR03 and CT03) and progressive (CTR1 and CT1) formation of an area of intensely localized deformation in front of the inclusion.

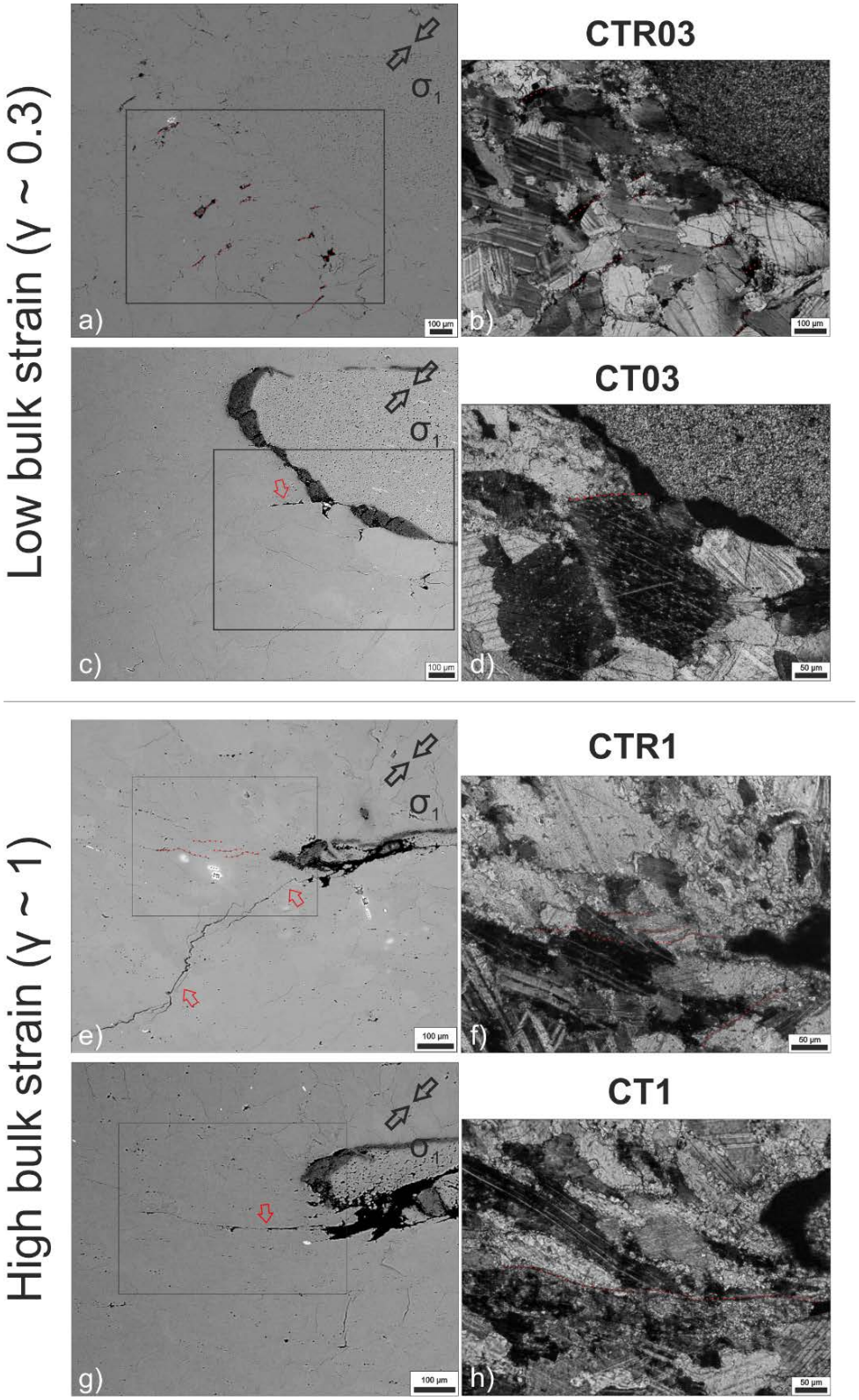

Figure 10: SEM images and optical close-ups of brittle features in the deformed samples for low (a-d) and high (e-h) bulk strain. Applied loading conditions are specified in brackets together with the sample number. The direction of maximum compressive stress, σ_1 is indicated in the upper right corner of the SEM images. The orientation of brittle cracks with respect to the direction of the principal stress is somewhat different at low strain between constant twist rate (a-b) and constant torque (c-d). Note voids that formed ahead of the inclusions (dotted segments in a). Dark seam at inclusion/matrix interface (b) is deformed ceramic cement. Note abundant pores decorating open and closed grain boundaries around the inclusion tip. With increasing bulk strain, similarly oriented fractures are present in both samples, while in the constant twist rate sample (e-f) a single fracture with similar orientation as at lower strain (a-b) is present. Cracks may have been enhanced by unloading at the end of the experimental run.

samples. Qualitatively, the microstructures of the two samples deformed to similar strain at different boundary conditions show similar characteristics.

The most striking feature characterizing the process zone of the high bulk shear strain samples (CTR1 and CT1, $\gamma \approx 1$; Fig. 9b and g) is the intense grain size reduction due to pervasive dynamic recrystallization (Fig. 9e and j), frequently resulting in core-and-mantle structures. The abundance of undulose extinction, lobate grains boundaries and subgrains similar in size to the recrystallized grains suggest prevailing subgrain rotation recrystallization with subordinate contributions of grain boundary migration recrystallization (Guillope & Poirier, 1979; Drury & Urai, 1990). At high strain twinning is less prominent. Grain boundaries are typically sutured and curved indicating grain boundary migration. We observe a shape preferred orientation of the deformed elongate grains resulting in a foliation gently inclined to the shear plane (Fig. 9b and g). Similar to the low strain samples, the main microstructural features are similar in samples deformed in both loading conditions applied to the high strain samples. Close to the inclusion tip incipient brittle deformation is visible in all samples (Fig. 10). Scanning electron microscope (SEM) images combined with optical close-ups reveal cracks preferentially located at grain boundaries and small voids ahead of the inclusion tip. Small, mostly tensile cracks oriented parallel to the direction of σ_1 are visible in the low strain constant twist rate sample (Fig. 10a-b). In the equivalent strain constant torque sample, a single shear fracture propagating from the tip of the weak limestone inclusion is formed within the host marble (Fig. 10c-d). Many grain boundaries in the process zone surrounding the inclusion tip are decorated by strings of pores. It is conceivable that these indicate crack closure and healing during the tests. The displacement associated with the shear fracture is accommodated by the weakest phase (the limestone), as can be observed in the relative movement of the ceramic glue at the contact between the marble and the inclusion. At higher bulk strain (Fig. 10e-h), a long single shear fracture is observed in the constant torque sample (Fig. 10g-h). For constant twist rate conditions (Fig. 10e-f) a few small incipient intracrystalline cracks developed at the very tip of the soft inclusion. No substantial offset can be discerned along these small cracks. A large, extended fracture oriented consistently to the direction of σ_1 is seen in this sample, potentially enhanced during unloading given its extension, developing beyond the microstructurally defined process zone.

2.4.4 Grain size and grain shape evolution

The microstructures of the investigated samples vary strongly on the sample scale as a result of the strain partitioning between limestone inclusion and host Carrara marble, and within the marble matrix due to the formation of a shear zone in front of the inclusion. To investigate the distribution of these heterogeneities within samples and between specimens deformed at different conditions we collected EBSD data and performed analysis

of grain size distribution and characterized the grain shape evolution (for details on the methods applied, see ***section 2.3***). Based on optical observations measuring some tens of recrystallized grains per thin section, average grain size of dynamically recrystallized grains was estimated to 20 ± 4 μm.

Grain size evolution: Figures 11a (low bulk strain samples) and 11b (high bulk strain samples), respectively, show profiles of average grain size plotted against axial distance from the inclusion (above and below; red rectangles in Fig. 11a and b indicate the approximate location of the inclusion). For details on the parameters used for the construction of profiles, see ***section 2.3***. Significantly reduced average grain size down to about 60 μm, as a result of intense dynamic recrystallization, is clearly visible in the process zone of all samples. Up to a shear strain of 0.3 a clear symmetry in the average grain size evolution across the process zone is displayed (Fig. 11a). At high strains of about 1 the development of two distinct domains on opposite sides of the inclusion becomes more evident, with lower average grain size values in the lower sector of the samples (Fig. 11b, note the different slopes of the profiles on opposite sides of the inclusion). The applied loading conditions have no significant effect on grain size evolution, suggesting that the amount of recrystallized material associated with localized deformation is not substantially dependent on the imposed boundary conditions. The finer step size EBSD maps

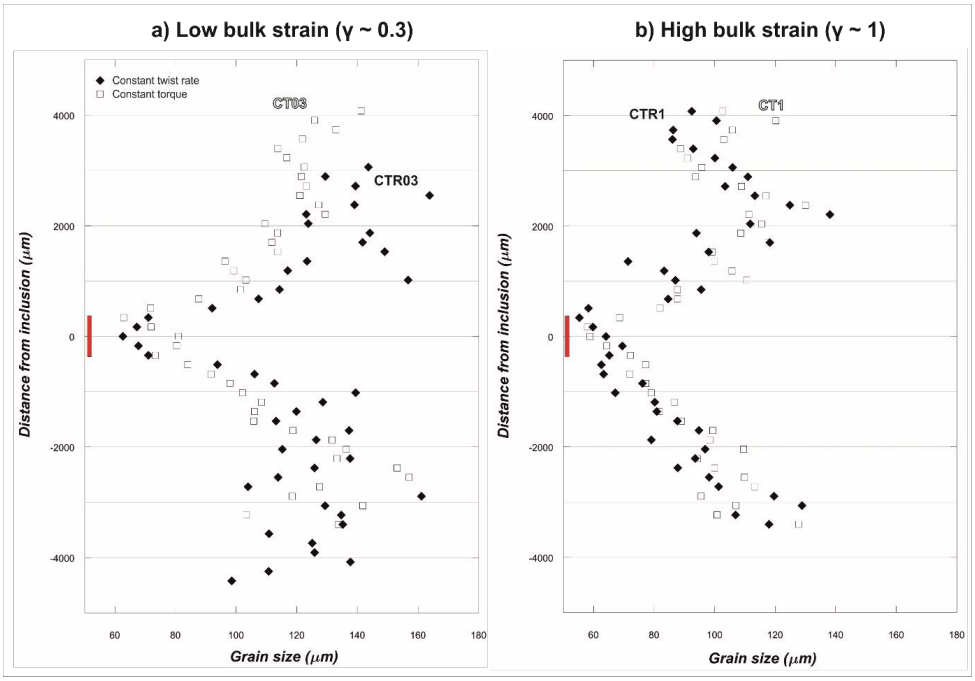

Figure 11: Evolution of average grain size across the thin section, above and below the process zone where deformation localizes in front of the limestone inclusion (the position of the inclusion is indicated in red). a) bulk strain = 0.3; b) bulk strain = 1.

(see ***section 2.3***) were used to investigate three regions of the samples in more detail (here referred to as upper domain, process zone and lower domain; Fig. 5a-d). The grain size distributions for all three domains, for the cumulative area of the maps and for the

undeformed starting material are shown in terms of area fraction vs equivalent diameter (Fig. 12; diameter of a circle of equivalent area to each grain). Solid, dashed and stippled lines indicate the median values for constant twist rate, constant torque and starting material samples, respectively (see Table 2 for a transcription of the values).

Sample number	**Total** γ_{bulk}	**Recrystallized grain size [μm]**	$\sigma^{\mathbf{a}}$ **[MPa]**	$\frac{\sigma_{local}}{\sigma_{bulk}}$	$\sigma^{\mathbf{b}}$ **[MPa]**	$\frac{\sigma_{local}}{\sigma_{bulk}}$
CTR03	0.29	10 ± 4	77 ± 30	2.2	100 ± 40	2.9
CT03	0.29	9 ± 3	87 ± 20	2.5	115 ± 30	3.4
CTR1	0.99	9 ± 3	85 ± 20	2.5	135 ± 40	4.2
CT1	0.94	8 ± 3	101 ± 35	3.1	135 ± 40	4.2

[a] Barnhoorn et al. (2004)
[b] Rutter (1995)

Table 2: Estimated recrystallized grain size and corresponding calculated equivalent stresses. Total γ_{bulk} = total imposed bulk strain.

For both low and high bulk shear strains the overall grain size distributions of constant torque and constant twist rate samples within the whole thin section area are largely overlapping with rather similar median values (Fig. 12a and e). In all samples, the average grain sizes are significantly reduced in the process zones compared to adjacent domains and the starting material. Reduction of average grain size outside the process zone is more pronounced at high strain (cf. median lines in Fig. 12h compared to Fig. 12d) as a consequence of the increased contribution of dynamically recrystallized grains.

For low strain samples (Fig. 12b-d) the strongest grain size reduction occurs within the process zone (Fig. 12c), where the applied loading conditions appear to play no role in the resulting distribution. Upper and lower domains (Fig. 12b and d) display some subtle differences in evolution between constant twist rate (CTR03) and constant torque (CT03) samples. For constant twist rate samples, grain size distributions are similar above and below the process zone. Samples deformed at constant torque show a generally lower average grain sizes in the domain below the process zone (Fig. 12d). In general, however, grain size evolutions are very similar in samples deformed at different loading conditions. At high strain, the asymmetry in grain size evolution between the upper and lower domain is preserved (also seen in Fig. 11), but the difference between loading conditions is reduced (Fig. 12f and h). Note, however, that the overall grain size evolution (Fig. 11) and distribution (Fig. 12a and e) ultimately appear not to be influenced by the imposed boundary conditions.

The spatial distribution of dynamically recrystallized grains across the combined three domains (stippled black rectangle in Figure 5a-d) using 3.5 μm step size maps is plotted in Fig. 13. Bivariate histograms are constructed by defining a 25x25 grid colour coded

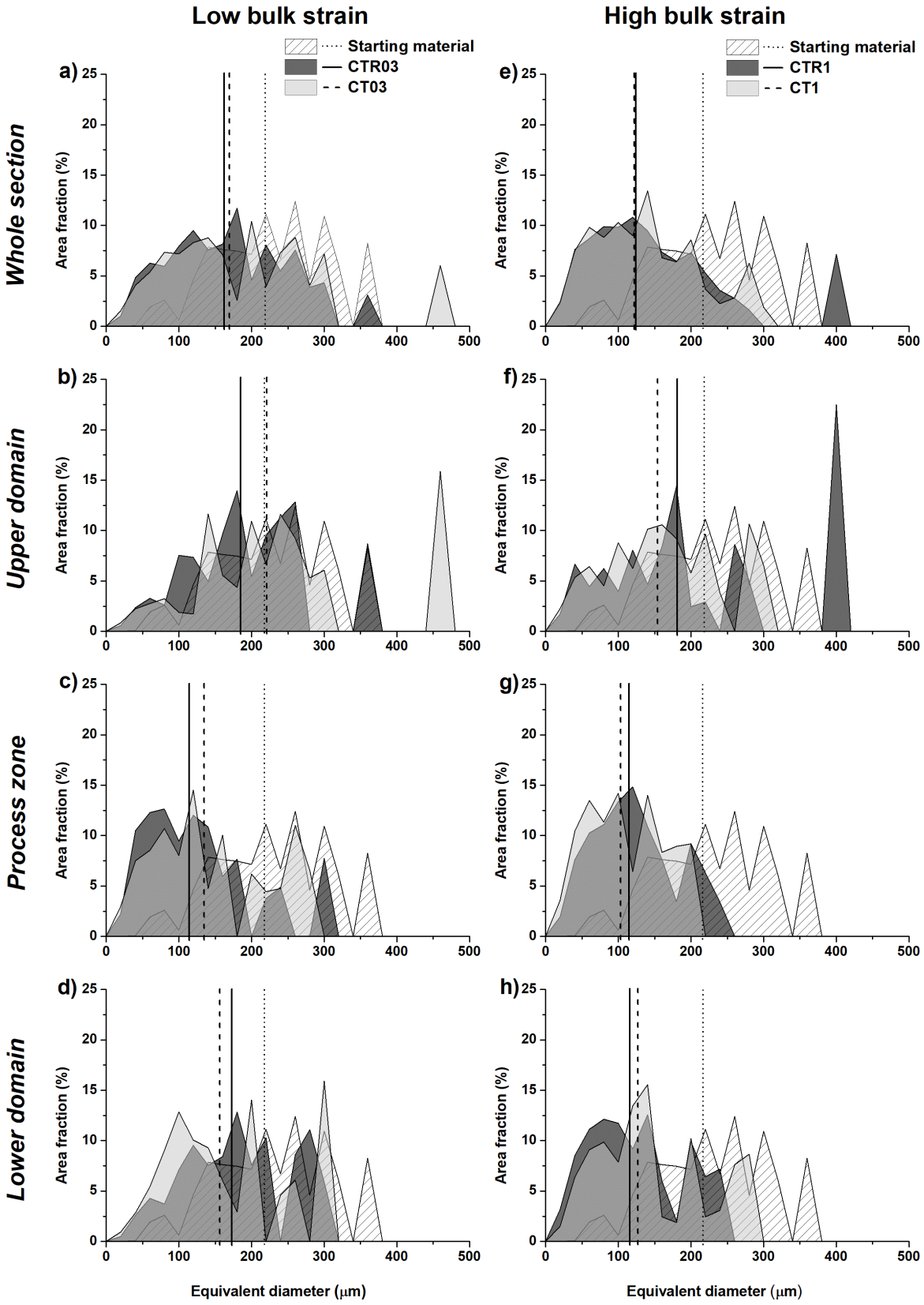

Figure 12: Grain size distribution expressed as normalized area fraction within domains described in text (upper, lower domains and process zone) and for the whole thin section for the two populations of samples (low bulk strain in a-d, high bulk strain in e-h) compared to the starting material. Solid, stippled and dotted lines indicate the median value of grain size distribution for constant twist rate, constant torque samples and undeformed material, respectively. The median grain size in the process zone of all deformed samples is significantly smaller than in adjacent domains and compared to the starting material.

based on how many recrystallized grains (equivalent diameter < 20 μm) are present within each grid square. The frequency of recrystallized grains is largest ahead of the inclusion and increases with increasing bulk strain. No major differences can be observed between the different loading conditions. This is in accordance with the observation that the area fraction of grains with equivalent diameter smaller than 20 μm is similar in samples deformed at both imposed boundary conditions (Fig. 12a and e).

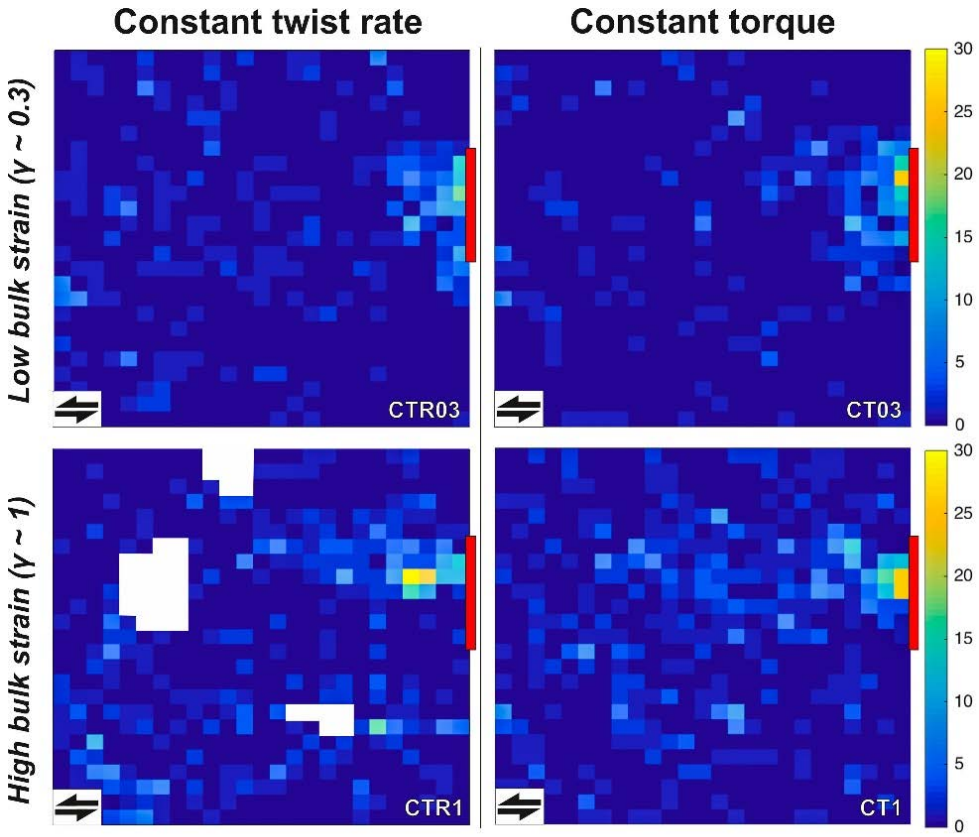

Figure 13: Bivariate histograms showing the spatial distribution of small recrystallized grains (eq. diameter < 20 μm) for constant twist rate (left) and constant torque (right) samples. A 25×25 grid was defined over the region of interest where the calculation is carried out (black rectangles, Fig. 5a-d); the scale indicates the number of measurements within each unit of the grid. A red bar indicates the approximate position of the inclusion prior to deformation. The white polygons in sample CTR1 correspond to patches of misindexed data (where the thin section was damaged) that were computed as artificial small grains by the mtex toolbox.

Grain shape evolution: We determined the average grain shape within the aforementioned domains to analyze the degree of plastic deformation of the matrix material (see ***section 2.3*** for details). In Figure 14a-l, normalized circularity and inverse aspect ratio data are plotted within the three area domains for the two considered bulk strains (Fig. 14a-f, $\gamma \approx 0.3$ and Fig. 14g-l $\gamma \approx 1.0$; the data is normalized to the total number of grains).

The shape distribution of the starting material (hatched curves) is given for comparison. Vertical lines indicate the median values of each distribution.

The histograms in Figs. 14a-c and 14g-i show the distribution of circularity data, i.e. a measure of the roughness of grain boundaries, at low and high bulk strain, respectively.

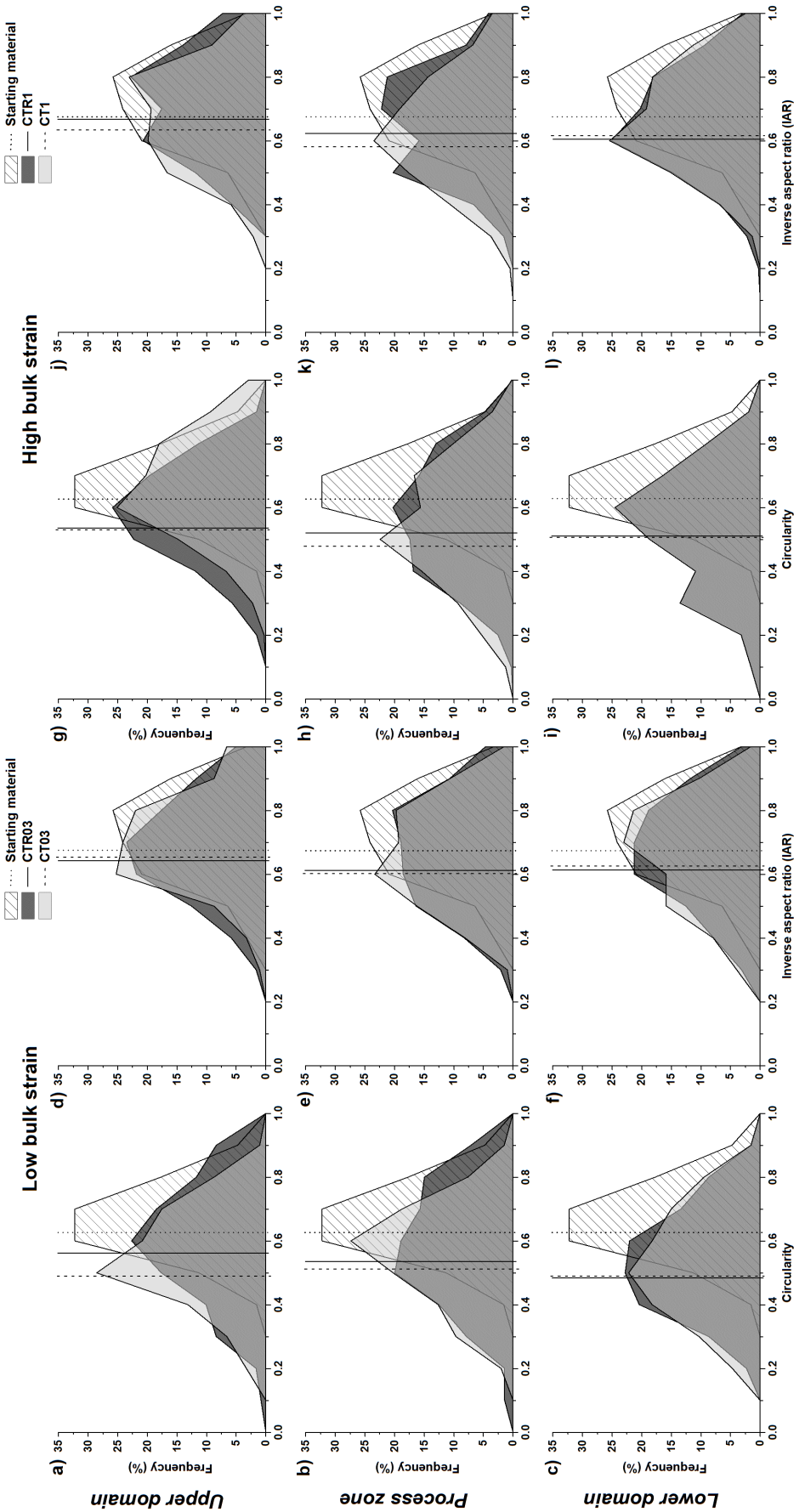
Low bulk strain
High bulk strain
Starting material
CTR03
CT03
CTR1
CT1
Upper domain
Process zone
Lower domain
Frequency (%)
Circularity
Inverse aspect ratio (IAR)
a)
b)
c)
d)
e)
f)
g)
h)
i)
j)
k)
l)

Figure 14: Frequency histograms for the two shape descriptors considered (circularity in a-c and g-i and inverse aspect ratio in d-f and j-l) within the three described domains (upper, lower and process zone) for all samples (low bulk strain in a-f and high bulk strain in g-l) with comparison to starting material distributions. Vertical lines indicate the median value of each distribution. For detailed description see text.

A comparison of the median values shows that the imposed boundary conditions do not produce a very significant difference in the distribution of circularities within any of the domains considered. Compared to the starting material distribution, both constant twist rate (CTR03, CTR1) and constant torque (CT03, CT1) samples show an overall increase in surface roughness (decrease in circularity values) across the entire thin section. The similarities between different boundary conditions are also found for the inverse aspect ratio data, especially at low strains (Fig. 14d-f). Within the general trend of increased ellipticity (decreased inverse aspect ratio) with respect to the starting material distribution, small differences are present in the process zone of high strain samples (Fig. 14k).

2.4.5 Local stress concentration at the tip of the inclusions

The observations carried out on macrostructural and microstructural data indicate that strain is locally concentrated within the Carrara marble in front of the weak Solnhofen inclusion. This suggests that the distribution of stress within the samples is also strongly heterogeneous. Stress appears to be locally enhanced in regions around the inclusion tips that experience the highest amounts of dynamic recrystallization and intracrystalline deformation. Several paleopiezometer techniques may be used to estimate local stresses (e.g., recrystallized grain size, dislocation density, twin density), but they all rest on the assumption that the considered microstructures are in equilibrium with the thermodynamic conditions. On the scale of the entire sample we observe a transient evolution of both strength and microstructure as the shear zone propagates into the Carrara matrix. Although on a local scale (process zone) we may have reached local steady state of stress and microstructure this is not the case for the entire samples considered here. The results presented in the following in terms of recrystallized grain size and dislocation density piezometry are therefore expected to represent lower and upper bounds, respectively, to the true stress values locally experienced by the samples. Recrystallized grains may be larger than the steady state size at the given stress conditions (lower bound), while the density of free dislocations might not be fully reset to the local stress (upper bound). Calibration of the recrystallized grain size piezometer for Carrara marble has been carried out at different experimental conditions by several authors (Schmid et al., 1980; Rutter, 1995; De Bresser, 1996; Barnhoorn et al., 2004). In this study, we applied the piezometer from Barnhoorn et al. (2004) calibrated on high strain torsion experiments performed between 500 and 700 °C and from Rutter (1995), who used triaxial compressive and extensional configurations at temperatures between 500 and 1000 °C. The general relationship

between stress and recrystallized grain size is given by:

$$\sigma = C \times d^m \tag{5}$$

where σ is the equivalent stress, d is the recrystallized grain size, and C and m are two constants. Note that the conversion from shear to equivalent stress is defined as follows (Paterson & Olgaard, 2000):

$$\tau = \frac{1}{\sqrt{3}}\sigma \tag{6}$$

The values of the two constants are 573.03 and -0.82, respectively, calibrated by Barnhoorn et al. (2004) and 812.83 and -0.88 using the calibration from Rutter (1995). Note that both piezometers are based on the assumption that subgrain rotation is the predominant recrystallization mechanism, as is expected from our microstructural observations (see ***section 2.4.3***). For the determination of recrystallized grain sizes within a lateral distance of about 500 μm from the inclusion, between 50 and 100 grains were digitized in each of the samples, and the average of their equivalent diameters was calculated. Results show stress concentration with respect to the applied bulk stress of 2.2-3.1 and 2.9-4.2 using the Barnhoorn and Rutter calibration, respectively (Tab. 3). Within error in grain size determinations, calculated stress values are independent of bulk finite strain and loading conditions.

Domain	***Low strain samples***		***High strain samples***		**Starting material**
	CTR03	CT03	CTR1	CTR1	
Whole section	158.2 μm	168.41 μm	134.52 μm	132.55 μm	214.17 μm
Upper domain	183.06 μm	218.44 μm	180.12 μm	163.39 μm	
Process zone	114.77 μm	136.28 μm	115.8 μm	102.14 μm	
Lower domain	169.77 μm	154.44 μm	116.18 μm	137.27 μm	

Table 3: Median values (in μm) for the area fraction grain size distribution presented in Figure 12.

Dislocation densities at increasing distance from the tip of the weak Solnhofen inclusion were estimated using transmission electron microscopy (TEM) of sample CTR03 (low bulk strain constant twist rate). Six foils of 0.15 μm thickness were prepared from areas within relict deformed grains at incremental distances of $\approx$ 500 μm (Fig. 15a). The foils were examined in STEM mode (scanning transmission electron microscope). Detailed images of each foil were acquired at 5 different tilt angles to highlight the number of visible dislocations. Subsequently, detailed images were stitched together and, by means of a user defined grid, spatial densities of free dislocations (number of dislocations per unit area, i.e. the number of free dislocations that would intersect the linear traverses of the

grid) were manually calculated for all the tilt angles considered. Following De Bresser (1996), the density is defined as:

$$\rho = \frac{2N}{\lambda t} \tag{7}$$

where N is the number of intersections, λ the length of the transect line and t the (constant) thickness of the TEM foil.

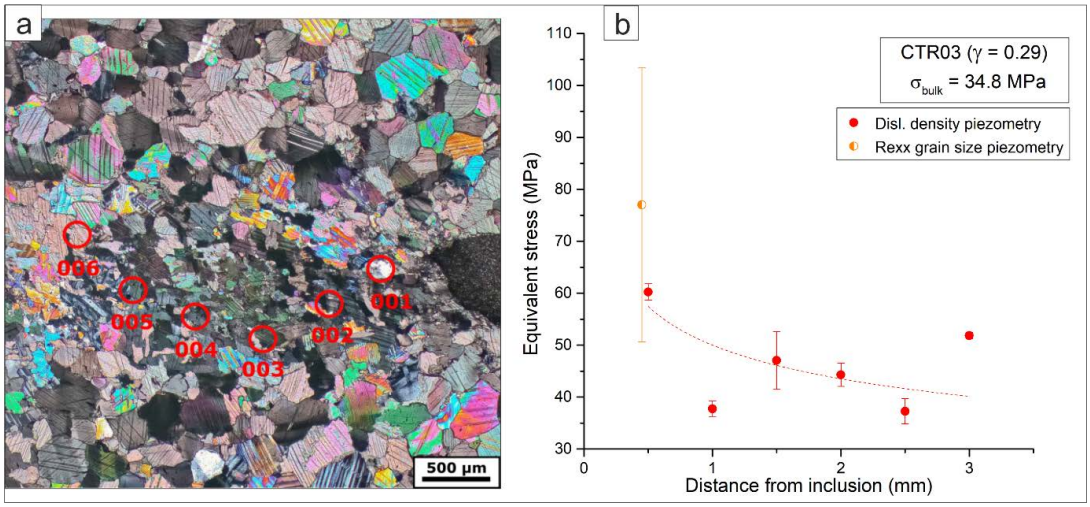

Figure 15: a) Micrograph of sample CTR03 with approximate locations of FIB foils for TEM analysis, b) local stress with distance from the inclusion tip as calculated using dislocation density (red) and recrystallized grain size (orange) piezometry.

The piezometer was calibrated by De Bresser (1996) on both single crystals and polycrystalline calcite deformed between 550-800 °C, yielding:

$$\sigma = 10^{-6.21} \times \rho^{-0.62} \tag{8}$$

where σ is the equivalent stress in MPa and ρ is the dislocation density in m^{-2}. Resulting stresses show significant error bars (as a consequence of the uncertainty in the measured dislocation densities), but decrease non-linearly with distance (Fig. 15b). With respect to the applied bulk equivalent stress of 34.8 MPa, the resulting stress concentration at the tip of the inclusion is approximately a factor 2, in accordance with the results from the recrystallized grain size piezometry.

2.4.6 Crystallographic preferred orientation

For the calculation of pole figures, maps produced with a 10 micron step size were used. A rectangular area of the thin sections covering the process zone was analyzed for all samples. Irrespective of applied loading conditions, a strong CPO developed in the deformed samples with increasing strain. Samples deformed at constant torque and constant twist rate show comparable textural evolution (Fig. 16b-e) and pole figures that differ significantly from the starting material (Fig. 16a).

In CTR03 (low strain constant twist rate sample, Fig. 16b), the [0001] axes are distributed along a rather complete girdle normal to the shear plane and with two maxima

at a high angle to the pole of the shear plane. For this sample, an incipient alignment of the poles of {10-14} with the pole of the shear plane is observed, while the poles of {11-20} appear to be quite scattered, with a component parallel to the shear direction. The {01-12} poles are distributed across two clear maxima at an angle of ≈ 45° to the shear direction. With increasing strain (Fig. 16c), the girdle of [0001] poles becomes more continuous and it cross-cuts the shear plane, also developing a strong maximum around 20° to the shear plane pole. While the {10-14} poles undergo some dispersion, poles of {11-20} strengthen the parallelism to the shear direction. Similarly, {01-12} poles preserve the two described maxima and develop two more, also at ≈ 45° to the shear direction. Poles of {01-18} form small girdles perpendicular to the shear zone, with a maximum concentration at an angle (≈ 15°) to the shear plane pole. In constant torque

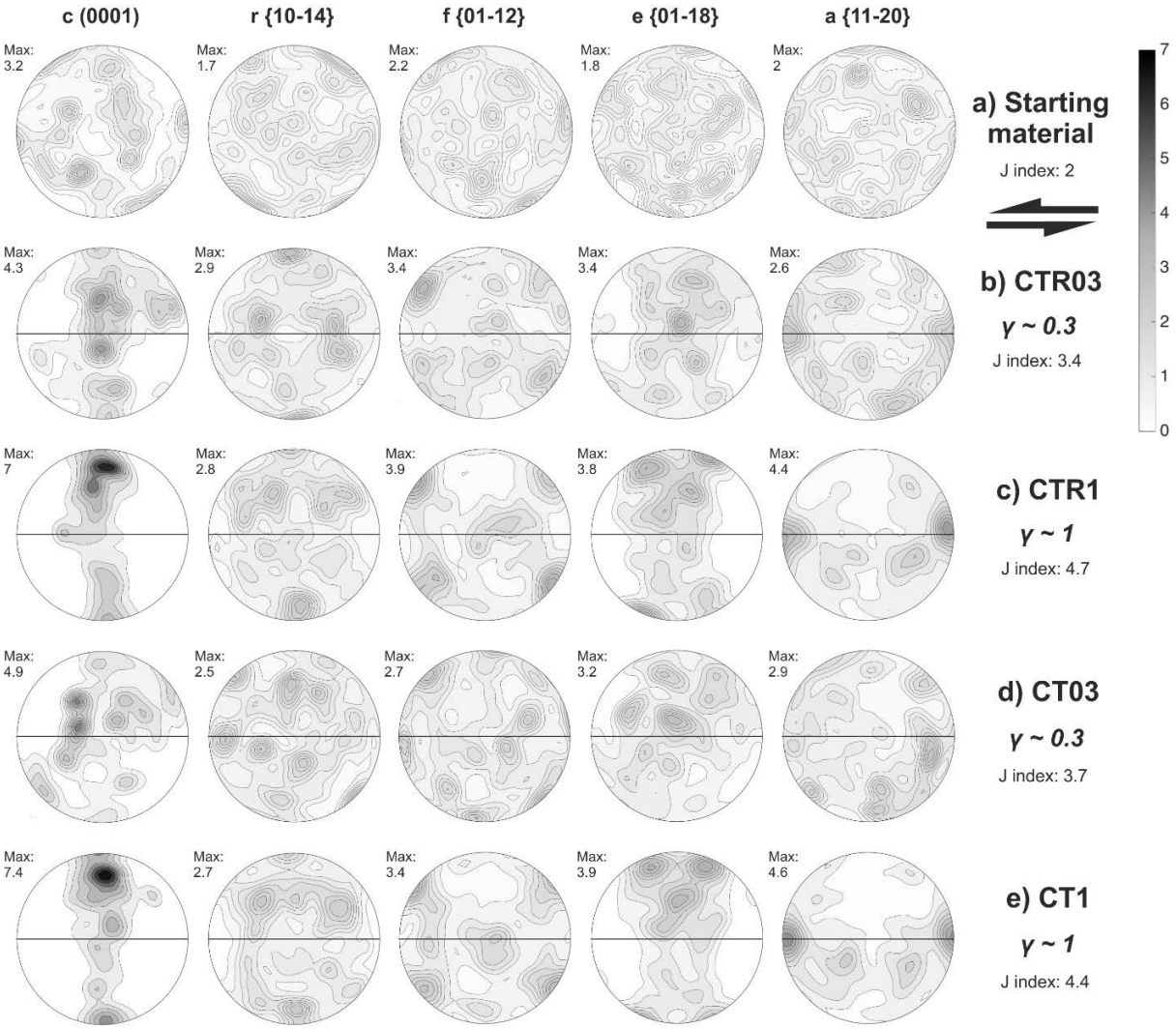

Figure 16: Crystallographic preferred orientation of calcite in Carrara marble a) from the undeformed sample or b-e) within the process zone of the experimental samples (as defined in fig. 3a-d), for the poles of basal (c (0001)), rhomb (r {10-14}, f {01-12}), (e {01-18}) and prismatic (a {11-20}) planes. Orientation of shear plane is indicated by arrows at the top right of the figure.

samples (Fig. 16d-e), CT03 presents a weak texture similar to the low strain, constant twist rate experiment. Poles of [0001] display a weak girdle with a maximum at about 30° from the center of the pole figure within the shear reference plane and two incipient

weak maxima oblique ($\approx 45°$) to the shear plane and opposite the shear direction are also visible. The poles to {10-14} and {11-20} planes are rather dispersed, although these latter display maxima normal and at $\approx 45°$ to the shear plane. Poles of {01-12} are again arranged in four symmetrical maxima at $\approx 45°$ to shear direction, with the addition of further maxima normal and sub-parallel to the shear plane. With increasing strain (Fig. 16e), the CPO strengthens substantially, similar to the sample deformed at constant twist rate. Poles of [0001] are now arranged in one single girdle normal to the shear plane, with one dominant maximum at $\approx 20°$ to the poles of the shear plane. The {10-14} poles show an alignment parallel to the shear plane, while the poles of {11-20} seem to follow the shear direction. Poles of {01-12} are arranged in four symmetrical maxima as described for the constant twist rate sample. A strong preferred orientation is observed for {01-18} poles as well, forming girdles around the normal to the shear plane.

2.5 Discussion

2.5.1 Weakening mechanisms

Plastic strain localization requires the development of an instability in the system undergoing deformation (Poirier, 1980; Hobbs et al., 1990). It is generally assumed that potentially coexisting weakening mechanisms (recrystallization-induced grain size reduction, CPO formation, reaction softening, shear heating) may lead to local strength perturbations and ultimately to strain localization (for a review, see Fossen & Cavalcante, 2017).

At the given experimental conditions, Carrara marble is expected to deform in the dislocation creep regime (e.g., Schmid et al., 1987; Pieri, Burlini, et al., 2001; Pieri, Kunze, et al., 2001; Rybacki et al., 2014). This assumption is confirmed by the observed presence of a strong crystallographic preferred orientation even at early increments of bulk shear strain (Fig. 16). Moreover, the increased mean aspect ratio of relict grains with respect to the undeformed starting material (Fig. 17a-b) associated with the development of a SPO within the process zone of the investigated samples (Fig. 17c-d) are indicative of intracrystalline deformation.

Intense, strain dependent grain size reduction by dynamic recrystallization is observed to develop dominantly in the process zone (Fig. 13), induced by the concentration of stresses and shear strain around the inclusion tip (Fig. 15). Some contribution of grain size sensitive diffusion creep is expected to be active in fine-grained regions in Carrara marble, as shown for the same experimental conditions and for recrystallized grain sizes in the order of 10-15 μm (ref. Fig. 13 in Rybacki et al., 2014). As discussed by the latter authors, the measured stress concentration at the tip of the inclusion may induce switching into the dislocation creep regime, suggesting that the deformation mechanism in Carrara marble leading to weakening at the examined experimental conditions is grain size insensitive. This is supported by our observations indicating formation of cracks at

the inclusion tip. The textural data (Fig. 16) allows identifying possible slip systems

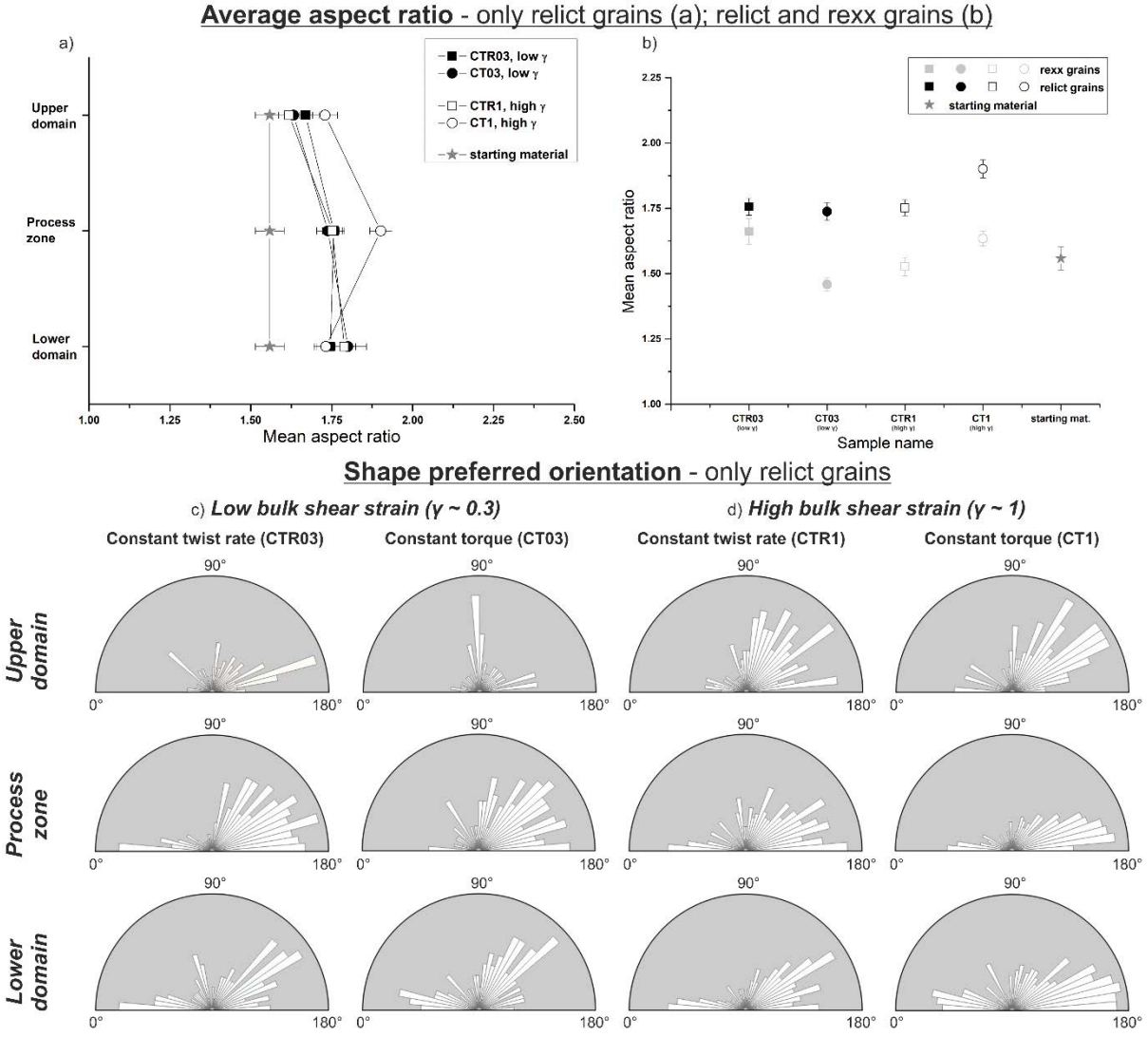

Figure 17: a) Analysis of mean aspect ratio of relict grains (equivalent diameter > 20 μm) across the vertical profiles defined in Fig. 4a-d; b) comparison of mean aspect ratios of relict (eq diam. >20 μm) and recrystallized (eq. diam < 20 μm) grains within the process zone of the samples; c, d) shape preferred orientation of relict grains (equivalent diameter > 20 μm) across the vertical profiles defined in Fig. 4a-d.

activated in the process zone of the samples, based on the classification of slip systems operating in calcite deformed at high temperature (e.g., de Bresser & Spiers, 1993). A general trend of switching main slip systems with increasing strain is observed in both constant twist rate and constant torque samples. Basal slip (notice the strong alignment of c-poles in Fig. 16c, e) is prevalent in both the high bulk strain samples, together with remnants of slip along the rhomb r plane in the a-direction {10-14} <20-21>. The low strain samples show a weaker texture, mainly due to slip along the rhomb r{10-14} and f{01-12} planes in the a<20-21> direction (Fig. 16b, d). Strengths of the texture within the process zone, as quantified by the calculated j-index (Bunge, 1982), are similar for constant twist rate and constant torque samples at similar bulk strains. Pole figures are in good agreement with observations on calcite at similar conditions in previous studies (Schmid et al., 1987; Pieri, Burlini, et al., 2001; Pieri, Kunze, et al., 2001; Barnhoorn et

al., 2004; Rybacki et al., 2014). The activity of similar slip systems and the analogous degree of textural development as a function of finite strain in our samples suggests that the deformation mechanisms active in the process zone are independent of applied loading conditions.

All deformed samples show cracks at the inclusion tips (Fig. 10a-h). Cracks mostly follow grain boundaries and some open fractures are oriented parallel to the maximum compressive stress. Although some microcracks may have been induced by cooling and unloading, voids, low aspect ratio cracks and healed cracks clearly formed during the tests. Locally, where stresses are concentrated, brittle deformation assists in reducing grain size as described in natural examples of crustal scale shear zone networks (Fusseis et al., 2006; Fusseis & Handy, 2008). The microstructural observations show that brittle fracturing even occurs in combination with plastic deformation of calcite (Fig. 10). As the process zone propagates into the Carrara marble matrix, cracking is overprinted by high-temperature creep of the fine-grained recrystallized matrix assisted by crack healing. It is conceivable that some of the cracking is also obliterated during unloading and slow cooling of the samples at the end of the experimental runs.

In CTR samples (Fig. 10a-b and e-f), microcracks and voids display a somewhat different distribution and orientation with respect to constant torque samples. At low strain, a set of small (50-100 μm) cracks is found, most that are oriented parallel to the direction of σ_1 (Fig. 10a-b). Most of these cracks are open and appear to be tensile in nature while others are associated with small, dynamically recrystallized material. At higher bulk shear strains (Fig. 10e-f), some intracrystalline microcracks occur in parallel to the maximum shear direction, together with a long interconnected fracture parallel to σ_1. In both constant torque experiments (Fig. 10c-d and g-h), a single fracture forms in plane with the shear propagation direction from the tip of the inclusion, consistent with the far field direction of maximum shear stress. It is, in all cases, difficult to assess with certainty whether any displacement occurred along these fractures, as the presence of fine recrystallized material related to the ongoing plastic deformation overprints any possible passive marker in the microstructure. The preservation of such a fracture in both low and high bulk strain sample suggests its formation in the early stages of deformation and its further exploitation with increasing strain. Brittle deformation, in all samples, appears to be confined to small domains (where local stresses and strain rates are highest) and small intervals of strain, associated with pervasive high-temperature creep of calcite.

2.5.2 Stress distribution and deformation transients

The heterogeneous stress distribution produced in the matrix due to the presence of an inclusion is clearly expressed in the resulting microstructures. The stress enhancement in the marble matrix in the process zone in front of the inclusion tip is substantial and has been quantified to a factor of 1.5-3 with respect to the applied bulk stress (Tab. 3, Fig.

15), although it should be borne in mind that the paleopiezometers applied here were calibrated for steady state conditions not achieved in our tests (Rutter, 1995; De Bresser, 1996; Barnhoorn et al., 2004). Note that the amount of stress concentration surrounding

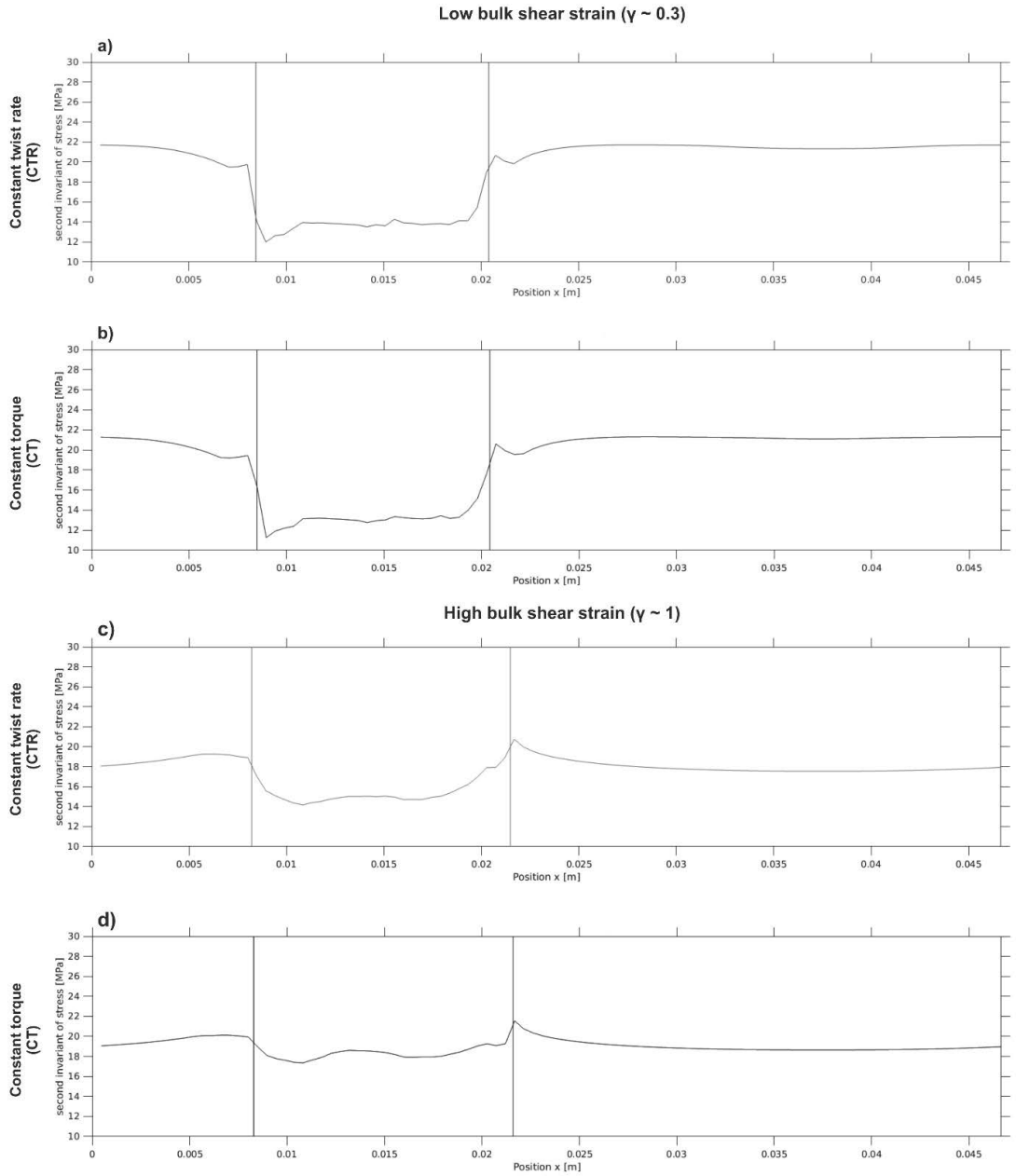

Figure 18: Results of a modeling study assuming material parameters and experimental conditions as in the tests (Döhmann et al., 2019). The profiles of the second invariant of stress are plotted across the outer surface of the sample cylinders; vertical lines are indicating the position of the Solnhofen limestone inclusion at the final bulk shear strain for low strain (a, b) and high strain (c, d). Note low shear stresses within the inclusion and stress maxima at the inclusion tips.

a material heterogeneity depends on the effective viscosity contrast between inclusion and matrix and on coupling of the two materials (Kenkmann & Dresen, 1998). At given thermodynamic conditions of our tests, the initial viscosity contrast between Carrara marble and Solnhofen limestone is expected to be a factor ≈ 10 (Rybacki et al., 2014). As suggested by the local shear strain, stress and grain size distributions found in the process zone, an exponential decay is observed with distance from the inclusion towards the matrix.

The time-dependent strain localisation pattern can be additionally investigated using numerical forward models (Döhmann et al., 2019, and Fig. 18). Here we employ 2D Cartesian models with periodic boundary conditions that have been benchmarked to experimental mechanical data. The gradient in flow stress reconstructed for sample CTR03 (Fig. 15) by means of dislocation density piezometry is in general accordance with results from numerical models (Fig. 18). In their study, Döhmann et al. (2019) found a rapid stress drop, down to roughly far-field levels, within 2-3 mm from the inclusion tip. Numerical modeling was carried out by means of the geodynamic modeling software SLIM3D (Semi-Lagrangian Implicit Model for 3 Dimensions, Popov & Sobolev, 2008), which was originally intended for the study of lithospheric-scale processes (Brune, 2016) but has been applied to laboratory scale localization models as well (Cyprych et al., 2016). For the applied thermodynamically coupled conservation equations, see Popov and Sobolev (2008). Experimentally derived (Schmid et al., 1980; Rybacki et al., 2014) flow laws were used to model deformation of Carrara marble and Solnhofen limestone, and a strain-dependent viscous softening mechanism was implemented (Brune et al., 2014). Model-derived profiles of the second invariant of stress along the inclusion and process zone at the cylinders' outer surface show local stress concentration at the inclusion tip decaying towards the matrix (Fig. 18).

Stress concentration is significantly smaller than observed in the deformed samples but the general trend agrees with experimental results. For example, a nonlinear stress decay is observed with increasing distance from the inclusion towards the matrix irrespective of loading conditions. The enhanced strain induced in the marble by the applied higher stresses leads to a progressive stress relaxation along the process zone (compare Fig. 18a and c for constant twist rate and 18b and d for constant torque experiments). Note that a stress peak at the inclusion tip is preserved in all cases, regardless of total strain (Table 3 and Fig. 18), as the viscosity contrast between the inclusion and the matrix surrounding it is still high. Fig. 18 also shows little difference in the shape and magnitude of the area of enhanced stress.

The paleowattmeter introduced by Austin and Evans (2007) allows grain size of dynamically recrystallized material to be related to mechanical work rather than to flow stress alone. We applied the suggested scaling relationship (Eq. 8, 9 in Austin & Evans, 2007) to our data. Using the measured grain sizes listed in Table 3 and the values of local strain rates derived from the strain markers (see ***section 2.4.2***), the predicted concentration in stresses with respect to the far field equivalent stress is in the range 3-5, in good agreement with the paleopiezometric estimates (factor 2-4, depending on calibration, Table 3). The approach may also be used to predict the average recrystallized grain size for given differential stresses and strain rates. Resulting recrystallized grain sizes vary between 10-12 μm (far field stress) and 8-10 μm (up to a factor 4 stress concentration, the upper bound derived from paleopiezometry), in accordance to what is measured optically in the samples (Table 3). Taking into account the uncertainty of measured grain sizes

and strain rates, we conclude that our experiments do not allow us to determine if the wattmeter yields more reliable results than the piezometer.

2.5.3 Amount and geometry of strain localization

Strain localization as indicated by strain markers increased as the process zone propagated into the Carrara matrix (Fig.8a, 8b). However, localization remained unaffected by the different loading conditions. Within the process zone at low bulk strains Carrara marble is strongly twinned: thick, often tapered or bent twins are abundant, as are multiple twin sets within single crystals. Deformation twinning in calcite has been extensively studied in the past (e.g., Barber & Wenk, 1979; Wenk, 1985), and twin morphology and intensity (number of twins per mm) are often used as stress-strain indicators (paleopiezometers) during low grade metamorphism (Ferrill, 1991; Ferrill et al., 2004; Rybacki et al., 2013); (see Burkhard, 1993, for a review). At low temperatures and low stress, twinning on the e-plane {01-18} may accommodate strain until hardening sets in due to the activity of only one independent slip system (Burkhard, 1993). At higher temperatures, dynamic recovery processes accommodate strain as observed in the high strain samples, CTR1 and CT1. Qualitatively, the morphology and distribution of twin sets do not display substantial differences between samples deformed at different loading conditions. Other microstructural expressions of localized viscous deformation in the process zone have been extensively presented (***sections 2.4.3*** and ***2.4.4***): little variation is noted for constant stress and constant strain rate samples. Strain partitioning into the process zone is clearly recognizable at low bulk strains of $\gamma \approx 0.3$ and continues progressively with increasing shear strain irrespective of loading conditions (Fig. 8b). Once weakening is completed with progressive strain, partitioning of shear strain into the localized shear zone saturates at a constant shear strain ratio between shear zone and bulk sample (Fig. 8a). The slope in Fig. 8a defines the critical shear strain γ_c required to complete weakening at a critical length of the process zone. Process zone length and shear strain gradient depend on viscosity contrast between the strong host rock and weak shear zone, and the weakening mechanism(s).

2.5.4 Comparison to previous experimental work

High temperature experimental deformation has been conducted extensively on rock-forming minerals to reproduce the processes occurring in natural shear zones. Since the introduction of the torsion setup in the Paterson gas deformation apparatus, a number of large strain studies have been performed on monophase materials, such as olivine (e.g., Bystricky et al., 2000; Hansen et al., 2012), calcite (Casey et al., 1998; Pieri, Burlini, et al., 2001; Pieri, Kunze, et al., 2001; Barnhoorn et al., 2004), quartz (e.g., Schmocker et al., 2003) or on multi-phase aggregates (e.g., Rybacki et al., 2003; Barnhoorn, Bystricky, Kunze, et al., 2005; Dimanov & Dresen, 2005; Holyoke III & Tullis, 2006). Notably,

although mechanical weakening of the deforming materials was described in all cases, localization of deformation at the sample scale was only observed in a small number of these studies, where it appeared to be favoured, e.g. by high initial strength contrast between phases (Holyoke III & Tullis, 2006), by a switch in deformation mechanism in only one of the deforming phases, producing locally heterogeneous phase distribution (Barnhoorn, Bystricky, Kunze, et al., 2005) or in the case of imposed constant load (torque) boundary conditions (Hansen et al., 2012). This latter is in good agreement with what was theoretically predicted for the torsion geometry by several authors (Fressengeas & Molinari, 1987; Leroy & Molinari, 1992; Paterson, 2007) who, by means of linearized perturbation analysis, prescribe strain localization to be dependent on the applied boundary conditions. A small enough perturbation of one of the material properties is not expected to produce localization in a constant displacement rate setting even if strain weakening is observed, as opposed to a constant load setup in which localization is always favored. However, the linear perturbation analysis of Fressengeas and Molinari (1987) is carried out with the assumption that deviations from homogeneity of the material properties are small. For larger perturbations the field equations cannot be linearized and the analytical solutions are much more complex. We argue that, in our experimental setting, the initial departure from a homogeneous stress distribution imposed by the presence of a strong viscosity contrast is much larger than can be treated by the linear approximation. As a consequence, it can be inferred that, for bi- or multi-phase materials with sufficient viscosity contrast (as is often the case in nature), the expected influence of boundary conditions on localization is absent or minor.

2.5.5 Implications for natural shear zones

Our study shows that, in the presence of a material heterogeneity in an otherwise homogeneous medium, localized shear zones form regardless of the imposed loading conditions. Recent theoretical studies accompanied by integration of existing field data (Whipple Mountains core complex, southeast California; Platt & Behr, 2011a, 2011c) propose a theory for the development of viscous shear zone in the middle to lower crust in a stress-controlled environment. The authors concluded that the yield stress of the undeformed host rock controls the flow stress in the deforming shear zone. Consequently, a constant velocity boundary condition is always converted into a constant stress condition. However, the theory is based on the assumption of steady-state deformation of a homogeneous crustal material. This premise seems to apply to a limited number of tectonic situations, but may not apply to channel flow (Beaumont et al., 2004) or the dynamic feedback between the brittle upper crust and the semibrittle to ductile lower crust during syn- and inter-seismic periods (Trepmann & Stöckhert, 2003). In their review paper on shear zones in the mantle, Vauchez et al. (2012) argue that the yield stress of a rock is strain rate dependent, where the strain rate itself is a function of shear zone width; thus stress can-

not be constant. Numerous field and experimental studies conducted in the past decades have identified a number of mechanisms that are believed to trigger strain localization at the crustal scale. Most of these involve some form of inherited presence of a rheological or structural heterogeneity, or the mentioned interaction with the seismogenic crust (for a review, see Vauchez et al., 2012). Our results suggest that a rheological heterogeneity will initiate shear zone formation with little impact of the applied boundary conditions.

2.6 Conclusions

We conducted high temperature torsion experiments to investigate the effect of loading conditions (constant twist rate or constant torque) on the initial and transient stages of strain localization in marble containing a weak material heterogeneity. The inclusion induced stress concentration halos in the stronger surrounding matrix resulted in strain partitioning into localized shear bands propagating into the marble with ongoing bulk deformation. Progressive localization is associated with strain weakening accommodated by dynamic recrystallization, CPO development and plastic deformation of relict grains within a process zone which is markedly different from the surrounding, relatively intact matrix. High temperature creep of marble is the dominant deformation mechanism at the applied experimental conditions, although evidence for coexisting brittle deformation is found regardless of loading conditions and total strain. This latter observation is of particular interest, as it is a feature that is frequently recognized in nature where the presence of fractures and veins associated with localized ductile deformation is often interpreted as the necessary precursor to localization (e.g., Mancktelow & Pennacchioni, 2005) or as the expression of coexisting brittle and ductile deformation (e.g., Badertscher & Burkhard, 2000; Ebert et al., 2007; Poulet et al., 2014). Overall, we observe that the geometry, microstructural and textural features and evolution of the process zone are qualitatively and quantitatively comparable in constant torque and constant twist rate experiments. Our results suggest that the loading conditions do not significantly affect strain localization induced by the presence of a material heterogeneity during nucleation and transient evolution stages. It should be kept in mind that the experimental setup poses some intrinsic limitations on the number of variables that can be investigated simultaneously. The effects that some of the latter (as the applied confining pressure, temperature or the presence of a second phase in the deforming matrix) might have on the weakening mechanisms and ultimately on the processes favouring strain localization are manifold and would require further investigation and a multidisciplinary approach (with experimental, field based and model based studies).

Acknowledgements

We are grateful to Stefan Gehrmann for the preparation of experimental samples and thin sections. Further thanks are given to Anja Schreiber for FIB-foil cutting and Dr. Richard

Wirth for the invaluable help with TEM analysis. Dr. Luca Menegon is gratefully thanked for fruitful discussion on the manuscript and the project in general. This manuscript was greatly improved by the thorough and constructive reviews of Marco Herwegh and Andreas Kronenberg, and comments from Editor-in-chief Kelin Wang. This project was founded by DFG grant GR 4468/2. M.D. and S.B. have been funded through the Helmholtz Young Investigators Group CRYSTALS (VH-NG-1132).

3 Strain localization and weakening processes in viscously deforming rocks: Numerical modeling based on laboratory torsion experiments

Summary

Localization processes in the viscous lower crust generate ductile shear zones over a broad range of scales affecting long-term lithosphere deformation and the mechanical response of faults during the seismic cycle. Here we use centimeter-scale numerical models in order to gain detailed insight into the processes involved in strain localization and rheological weakening in viscously deforming rocks. Our 2D Cartesian models are benchmarked to high-temperature and high-pressure torsion experiments on Carrara marble samples containing a single weak Solnhofen limestone inclusion. The models successfully reproduce bulk stress-strain transients and final strain distributions observed in the experiments by applying a simple, first-order softening law that mimics rheological weakening. We find that local stress concentrations forming at the inclusion tips initiate strain localization inside the host matrix. At the tip of the propagating shear zone, weakening occurs within a process zone, which expands with time from the inclusion tips towards the matrix. Rheological weakening is a precondition for shear zone localization and the width of this shear zone is found to be controlled by the degree of softening. Introducing a second softening step at elevated strain, a high strain layer develops inside the localized shear zone, analogous to the formation of ultramylonite bands in mylonites. These results elucidate the transient evolution of stress and strain rate during inception and maturation of ductile shear zones.

3.1 Introduction

Localization of deformation is ubiquitous in Earth materials and observed over a broad range of scales in space and time (Fossen & Cavalcante, 2017). In the brittle upper crust, localization is represented by fault zones (Coyan et al., 2013; Valoroso et al., 2013) transitioning into localized ductile shear zones in the middle–lower crust at the brittle-ductile transition hosting mylonites and ultra-mylonites (Palin et al., 2015; Park & Jung, 2017). Localization within the deeper ductile lithosphere is accommodated by a combination of different deformation mechanisms, e.g. diffusion and dislocation creep, frictional sliding or cataclasis, depending on mineral composition and boundary conditions (Kenkmann & Dresen, 2002; Burlini & Bruhn, 2005). These processes cause shear zone initiation at material heterogeneities and multiple defects commonly present in rocks that serve as nucleation points for shear zones on the micro- or macro-scale. Typical examples include randomly scattered flaws (e.g., Misra & Mandal, 2007), brittle fractures (Mancktelow & Pennacchioni, 2005), weak layers (Gerbi et al., 2014), veins and dykes (Handy, 1989) or

rock fabric (Bürgmann & Dresen, 2008). A plethora of studies showed that a subsequent strength reduction in shear zones may be attributed to a wide range of processes, like grain-size reduction (Tasaka et al., 2017), shear heating (Duretz et al., 2015), a combination of both (Foley, 2018), a change in controlling deformation mechanism such as from dislocation to diffusion creep (e.g., White, 1976; Handy, 1989; Linckens et al., 2011), the development of crystallographic preferred orientations (Ji et al., 2004) or melting (Handy et al., 2001).

Laboratory experiments on rock materials provide insights into localization and weakening processes during shear zone formation at well-defined deformation conditions. Several experimental studies at high P-T conditions have investigated strength and microstructures in high-strain deformation tests on mono-mineralic geomaterials. For pure Carrara marble it was found that strain weakening is associated with recrystallization to a fine grain size, the development of a strong lattice-preferred orientation (Pieri, Burlini, et al., 2001), and that steady state flow is reached at shear strains $\gamma > 4$ (Pieri, Kunze, et al., 2001). In axial compression tests at 700–990 °C, Ter Heege et al. (2002) found that dislocation creep mechanisms dominate Carrara marble flow at peak stresses and that grain size sensitive mechanisms contribute to flow only for higher bulk shear strains. However, Barnhoorn et al. (2004) observed no significant contribution of diffusion creep even for large shear strains $\gamma \leq 50$. Only minor rheological weakening may be attributed to grain size reduction by dynamic recrystallization, if grain growth is not inhibited (De Bresser et al., 2001). Zener pinning for example impedes grain growth and can thus enhance strain localization (Bruhn et al., 1999; Herwegh et al., 2005; Linckens et al., 2011; Bercovici & Ricard, 2012). By means of experimental studies with multiphase aggregates the localization phenomena have been analyzed at various conditions. A second phase, for example, helps maintain a fine grain size that allows continuous deformation in the diffusion creep regime (Tasaka et al., 2017). Geometric phase mixing occurs only at very high shear strains and is hence a consequence of localization (Cross & Skemer, 2017). Stress partitioning in a two phase system may lead to above-average stresses in one phase and comparatively low stresses in the other (Bruhn & Casey, 1997). Strong stress and strain gradients close to matrix/inclusion interfaces were also observed in a two-phase study using anorthite-diopside aggregates and are similar to deformation microstructures observed in ultramylonites (Dimanov & Dresen, 2005).The effect of material heterogeneities on the rheological response of otherwise homogeneous Earth materials has been recently addressed by Rybacki et al. (2014), who analyzed the effect of material heterogeneities on the onset of localized viscous deformation. These studies revealed a rich interplay of various factors and processes, yet it is difficult to study individual processes in isolation and to provide a time-dependent view of strain localization.

In addition to experimental studies, numerical modeling of localization processes allows testing realistic materials in order to isolate the effect of specific deformation mechanisms and parameters. Previous numerical modeling work aimed at understanding the role of

strength anisotropies that are either caused by compositional differences (Kenkmann & Dresen, 1998; Mancktelow, 2002; Treagus & Lan, 2004; Cook et al., 2014) or due to inherited structures (Corti et al., 2007; Mazzotti & Gueydan, 2018; Webber et al., 2018). For example, during lithospheric extension the inherited mechanical structure exerts a strong control on rift geometry and architecture (Duretz et al., 2016). Material heterogeneities significantly impact strain localization: (1) Hard inclusions produce stress concentrations inside a homogeneous matrix (Kenkmann & Dresen, 1998), and (2) weak inclusions localize strain in turn producing stress concentrations at the inclusion matrix interface (Cyprych et al., 2016). Jammes et al. (2015) identified three end-member types of shear zones: (1) localized, (2) localized anastomosing and (3) delocalized shear zone that depend on the proportion of strong and weak phase and the strength ratio. Other modeling studies focused on the effect of rheological weakening and hardening mechanisms. Weakening mechanisms have been formulated as a function of strain (Cyprych et al., 2016; Mazzotti & Gueydan, 2018), stress (Gardner et al., 2017), deformation work or grain size in combination with grain-size dependent flow laws (e.g., Jessell et al., 2005; Bercovici & Ricard, 2012; Herwegh et al., 2014; Cross et al., 2015). However, all these formulations have been shown to strongly influence the localization behavior in numerical models.

Here we compare the results of our numerical models to a series of laboratory tests (Nardini et al., 2018). in order to investigate the temporal and spatial evolution of strain localization and weakening processes in viscously deforming rocks. As mentioned above, ductile shear zones are often initiated at material heterogeneities which is why we use a single weak inclusion torsion setup to analyze dynamics, strength, and geometry of the resulting ductile shear zone. Based on this reference model, we perform additional numerical experiments assessing the time-dependent impact of weakening through a scan of the relevant parameters and finally we focus on the formation of ultramylonites.

3.2 Laboratory experiments

3.2.1 Experimental setup

Sample preparation is following the procedures described in Rybacki et al. (2014): cylinders of Carrara marble (10 mm in length, 15 mm outer diameter) were cut from a single block of marble, and an internal borehole (6.1 mm of inner diameter) was cored and subsequently filled with cylinders of solid gold to provide a homogeneous distribution of stress over the entire sample through the full duration of the experiments (Paterson & Olgaard, 2000). Circular segments of Solnhofen limestone (arc length $\approx$ 11.8 mm), a very fine grained (average grain size $<$ 10 μm) rock, were produced by polishing $\approx$ 750 μm thick sections that were subsequently inserted in the external surface of the Carrara marble cylinders (see Figure 19a).

Experiments were conducted in a Paterson-type gas deformation apparatus (Paterson,

1970), at 900 °C temperature and 400 MPa confining pressure. The samples were inserted in copper jackets of ≈ 0.2 mm thickness, and jacket strength at the experimental conditions was accounted for in the evaluation of the mechanical data. Straight vertical scratches on the jacket surface serve as passive strain markers. As shown in Rybacki et al. (2014), at experimental P-T conditions the fine grained limestone is substantially softer than Carrara marble and therefore acts as a weak material heterogeneity within a homogeneous stronger matrix. Two different loading conditions, constant twist rate (equivalent to a shear strain rate of 1.9×10^{-4} s^{-1} at the outer periphery) and constant torque (≈ 18.8 MPa), were tested. For each loading type, samples were tested to a final bulk shear strain $\gamma \approx 1$ (Nardini et al., 2018).

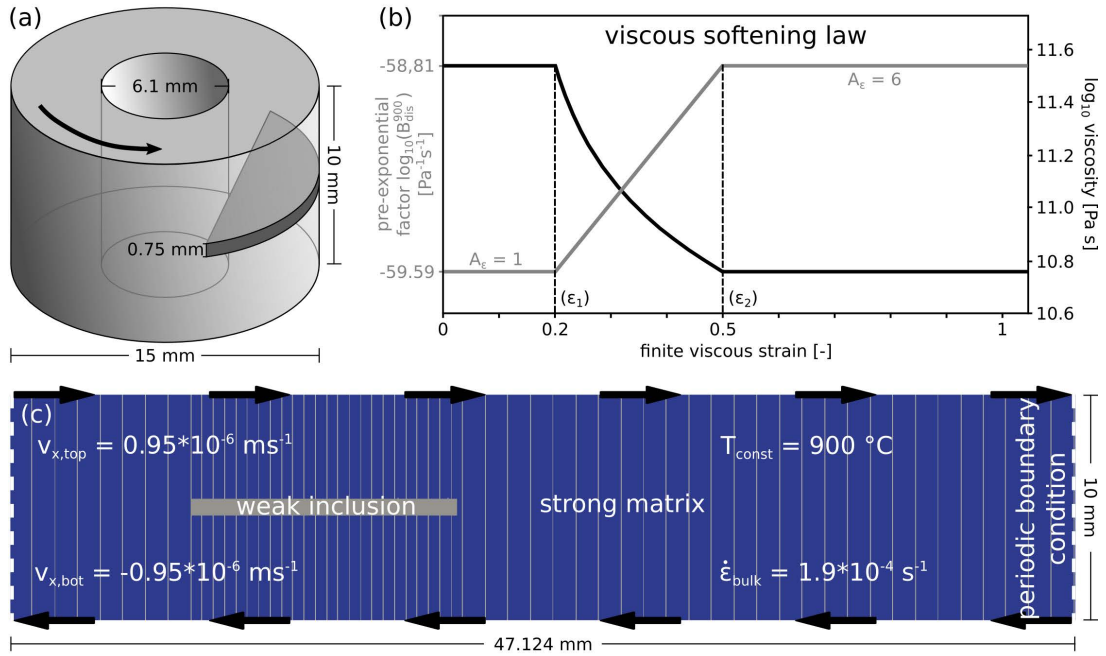

Figure 19: a) Schematic drawing of experimental setup: cylinder height is 10 mm, outer diameter is 15 mm, the inclusion features an angular length of 90° and the inner borehole has a diameter of 6.1 mm and is filled with a solid gold cylinder. The matrix consists of Carrara marble and the inclusion of Solnhofen limestone. b) Effect of viscous softening on Carrara marble flow law. The factor A_ε (a fraction of the weakening amplitude A) is increased between the two threshold values of local finite strain ε_1 and ε_2, hence the effective viscosity is locally reduced. c) Model setup and boundary conditions. Constant bulk strain rate ($\dot{\varepsilon}_{bulk}$) is achieved by prescribing velocity at top ($v_{x,top}$) and bottom ($v_{x,bot}$) model boundaries. At the left and right model side we use periodic boundary conditions, i.e. velocity and stress are continuous across these faces and any material point crossing these boundaries enters again on the other side of the model. Flow laws of matrix and inclusion are chosen to represent Carrara marble (strong matrix) and Solnhofen limestone (weak inclusion) (see Table 4). Vertical gray lines are passive strain markers.

3.2.2 Experimental results

At constant twist rate, calculated shear stress at the sample periphery initially increased up to a peak value of ≈ 19–20 MPa at a bulk shear strain of $\gamma \approx 0.2$, followed by gradual weakening up to the maximum bulk shear strain of about 1 for sample CTR1 (Figure 20a). This sample is used to benchmark the numerical model. In the constant torque experiment, torque was kept uniform such that the maximum shear stress at the sample periphery was about 18.8 MPa, similar to the peak stress measured in the constant twist rate experiment (see supplementary Figure 27 for results of the constant torque experiment

and a comparison to a numerical model). The experiments reveal that in front of the inclusion the strain within the Carrara marble was strongly localized forming a process zone consisting of highly deformed grains and grain size reduction. The local shear strain in this area is higher than in the adjacent host rock. At the inclusion tip, the local strain is up to about 30 times higher than in the neighboring matrix and ≈ 10 times higher than the bulk strain (Nardini et al., 2018).

3.3 Model description

In the following, we describe the setup of the numerical model and examine 1) the results in comparison to the associated laboratory experiments, 2) the time-dependent evolution of the model, 3) the role of softening, 4) the effect of varying softening parameters, and 5) the impact of progressive softening. Points 1) and 2) combined with the mechanical data yield further insights into the strain localization process. With 3) to 5) we expand the parameter space beyond the experimental results allowing new insights from the numerical perspective.

3.3.1 Numerical modeling technique

We use the geodynamic modeling software SLIM3D (Semi-Lagrangian Implicit Model for 3 Dimensions) (Popov & Sobolev, 2008). The implicit finite element code utilizes the Arbitrary Lagrangian-Eulerian Method, has a realistic elasto-visco-plastic formulation for rheology and a free surface. The software was originally designed to investigate lithospheric-scale processes and has since been applied in divergent (Brune et al., 2012, 2013, 2014, 2016, 2017; Brune & Autin, 2013; Brune, 2014; Heine & Brune, 2014; Koopmann et al., 2014; Clift et al., 2015) convergent (Quinteros et al., 2010; Quinteros & Sobolev, 2013; Duesterhoeft et al., 2014; Ballato et al., 2019) and transform (Popov et al., 2012; Brune, 2014) plate boundary settings. Recently however, its scope has been extended with the aim to investigate localization processes on the centimeter-scale (Cyprych et al., 2016). With the SLIM3D software, we solve the thermomechanically coupled conservation equations of momentum

$$-\frac{\partial p}{\partial x_i}+\frac{\partial \tau_{ij}}{\partial x}+\rho g_z=0 \tag{9}$$

energy

$$\rho C_p\frac{DT}{Dt}-\frac{\partial}{\partial x_i}(\lambda\frac{\partial T}{\partial x_i})-\tau_{ij}\dot{\varepsilon}_{ij}=0 \tag{10}$$

and mass

$$\frac{1}{K}\frac{Dp}{Dt}-\alpha_T\frac{DT}{Dt}+\frac{\partial \upsilon_i}{\partial x_i}=0 \tag{11}$$

with coordinates x_i, velocities υ_i, temperature T, time t, pressure p, stress deviator τ_{ij}, strain rate deviator $\dot{\varepsilon_{ij}}$, densities ρ, gravity vector g_z, heat capacities C_p, heat conductivi-

ties λ, thermal expansitivity α_T and bulk moduli K. The Einstein summation convention is applied over repeated indices.

The conservation equations are solved simultaneously considering the constitutive laws that relate deformation and stress. Total deviatoric strain rate is described as the sum of elastic and viscous strain rate (Simo & Hughes, 2006):

$$\dot{\varepsilon}_{ij} = \dot{\varepsilon}_{ij}^{elastic} + \dot{\varepsilon}_{ij}^{viscous} = \frac{1}{2G}\hat{\tau}_{ij} + \frac{1}{2\eta_{eff}}\tau_{ij} \tag{12}$$

where G is the elastic shear modulus, $\hat{\tau}_{ij}$ the objective stress rate (e.g., Bonet & Wood, 1997), and η_{eff} the effective viscosity. We use dislocation creep flow laws to model the viscous deformation of limestone and marble. The effective viscosity is described as:

$$\eta_{eff} = \frac{1}{2}\tau_{II}\dot{\varepsilon}_{dis}^{-1} \tag{13}$$

with τ_{II} as the second invariant of the effective deviatoric stress, given by:

$$\tau_{II} = \sqrt{\frac{1}{2}(\sigma_{xx} - p)^2 + \frac{1}{2}(\sigma_{yy} - p)^2 + \frac{1}{2}(\sigma_{zz} - p)^2 + \sigma_{xy}^2 + \sigma_{xz}^2 + \sigma_{yz}^2} \tag{14}$$

and $\dot{\varepsilon}_{dis}$ as the second invariant of the viscous strain rate for dislocation creep, which is defined as:

$$\dot{\varepsilon}_{dis} = B_{dis}A_{\varepsilon}(\tau_{II})^n exp(-\frac{E_{dis}}{RT}) \tag{15}$$

where B_{dis} is the material-dependent creep parameter or pre-exponential factor, A_ε is a strain-dependent function of an arbitrary factor A which we call the weakening amplitude (defined below), n is the power law stress exponent, E_{dis} the activation enthalpy and R the gas constant (Popov & Sobolev, 2008). Flow law parameters for Carrara marble and Solnhofen limestone are given in Table 4.

To account for the rheological weakening mechanisms operating in rocks at elevated temperatures and pressures, we implement the function A_ε that captures progressive weakening. The strain rate $\dot{\varepsilon}_{dis}$ in each element is increased by this factor A_ε depending on the actual viscous strain ε of the element:

$$A_\varepsilon = \begin{cases} 1 & \text{if } \varepsilon < \varepsilon_1 \\ 1 + \frac{A-1}{\varepsilon_2 - \varepsilon_1}(\varepsilon - \varepsilon_1) & \text{if } \varepsilon_1 < \varepsilon < \varepsilon_2 \\ A & \text{if } \varepsilon > \varepsilon_2 \end{cases} \tag{16}$$

The threshold values ε_1 and ε_2 depend either on 1) accumulated finite viscous strain (see Cyprych et al., 2016) or 2) deformation work per element volume W_{def} defined as:

$$W_{def} = \varepsilon_{visc} \times \tau_{II} \tag{17}$$

with ε_{visc} as the viscous component of finite strain, which is computed by integrating the second invariant of the deviatoric viscous strain rate tensor with respect to time. For all $\varepsilon < \varepsilon_1$ the factor A_ε is 1. With increasing finite viscous strain, A_ε is linearly increased between the threshold values ε_1 and ε_2. For $\varepsilon > \varepsilon_2$, A_ε is equivalent to the weakening amplitude A. As a result, this parameterization reduces the effective viscosity (see Figure 19b). The thresholds ε_1 and ε_2 and the weakening amplitude A of the reference model are determined manually by iterative comparison to experimental observations (Figure 20a). A is chosen such that the stress drop observed from peak stress until the end of the experiment is matched. The threshold values ε_1 and ε_2 control the onset and the end of weakening and were selected such that the shape of the stress strain curve from the experiment is reproduced by the numerical model.

Phase	**Boundary conditions**		**Flow laws**		**Reference strength** (at strain rate 1.9×10^{-4} s^{-1})	
	T [°C]	$\dot{\varepsilon}$ [s^{-1}]	n	$\log_{10}(B_{dis}^{900})$ [Pa^{-1} s^{-1}]	Stress [MPa]	η [Pa s]
Carrara marble (matrix)	900	1.9×10^{-4}	7.6[ab]	- 59.59[a]	22.45	5.91×10^{10}
Solnhofen limestone (inclusion)	900	1.9×10^{-4}	1.4[a]	-13.10[c]	5.00	1.32×10^{10}

[a] Rybacki et al. (2014)
[b] Schmid et al. (1980)
[c] Rybacki et al. (2014) report - 12.55; was modified such that peak stress of model is equivalent to experiment

Table 4: Flow laws and boundary conditions for the reference model. Temperature dependence is incorporated in the pre-exponential factor and flow law parameters are valid for given boundary conditions only . Reference strength gives stress and viscosity at the used bulk shear strain rate (1.9×10).

3.3.2 Setup of the numerical model

Our reference model is designed to reproduce the single inclusion experiments of Nardini et al. (2018) described above in 2D Cartesian coordinates. We model the laboratory shear deformation of a hollow cylinder by using periodic boundary conditions, such that material leaving one side of the model in shear direction enters again on the opposite side (see Figure 19c). The model height is 10 mm and the length of the model along shear direction is 47.124 mm which represents the outer circumference of the hollow cylinder in the laboratory experiment. Thermal properties of the material do not influence the model results, due to an imposed temperature of 900 °C and the small model size. For the same reason temperature gradients are quickly dissipated, which is why shear heating does not play a role. To compare with the experiments, we apply constant strain rate and constant stress boundary conditions, respectively. Flow laws implemented in the models are based on a series of torsion and triaxial experiments performed on Carrara marble and Solnhofen limestone by Rybacki et al. (2014). The flow law parameters are similar to those obtained by Schmid et al. (1980). Activation energy and thus temperature dependency are incorporated into the material-dependent pre-exponential parameter (B_{dis}^{900}), as the experiments and models are performed at a constant temperature (900 °C) (see Table

4). The Solnhofen limestone flows as a superplastic material at the given P-T conditions (Schmid et al., 1977), due to its small grain-size. This is incorporated into the model setup by employing a low stress exponent of n = 1.4 derived by Rybacki et al. (2014)

3.4 Numerical model results

3.4.1 Benchmarking of the numerical model

We deduce the three weakening parameters of our strain-dependent softening parametrization (ε_1, ε_2, A), by iterative comparison between experiments and model. The experimentally derived stress-strain curve and final strain distribution are successfully reproduced using a model with the following values for the accumulated finite strain thresholds: ε_1 = 0.2, ε_2 = 0.5 and the weakening amplitude: A = 6 (Figure 19b) affecting the Carrara marble.

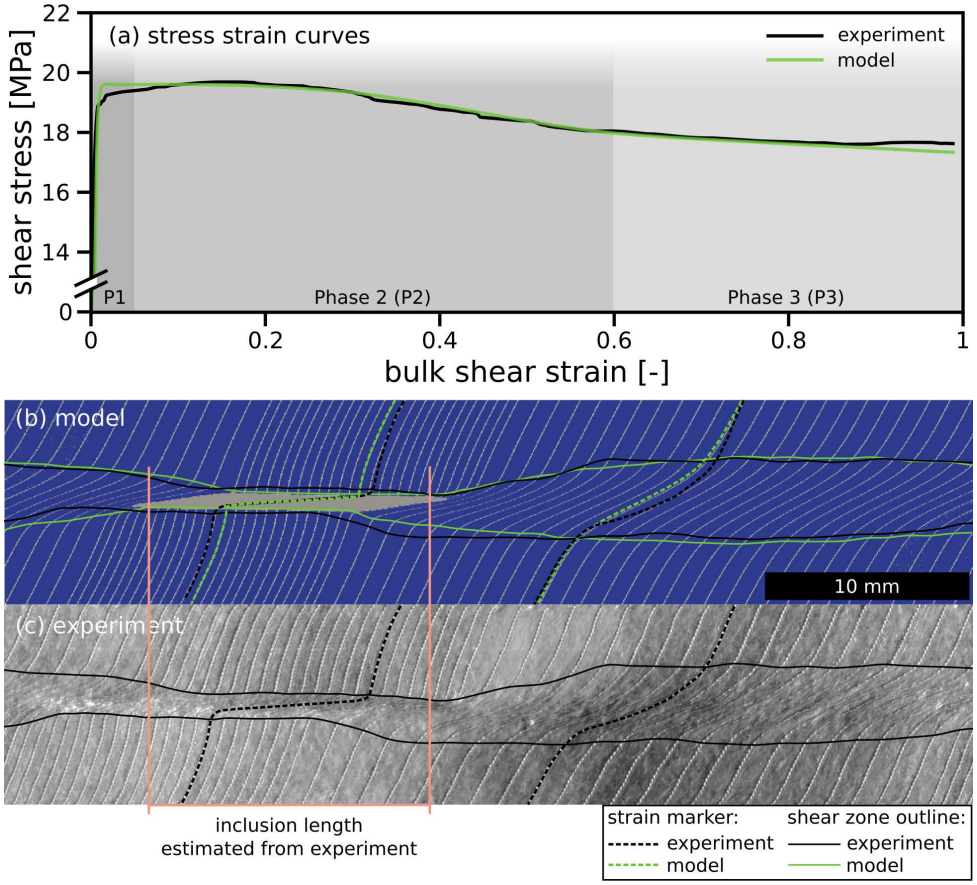

Figure 20: Benchmark and comparison of constant strain rate model to experiment. a) Stress strain curves of reference model (green) and experiment (black). Background shows the phases P1 – pre-weakening, P2 – onset and acceleration of weakening and P3 – deceleration of weakening. b) Model with passive strain markers and shear zone outlines of model (green) and experiment (black). c) Copper jacket from experiment with passive strain markers, estimated inclusion length and shear zone outline. Results in b) and c) are shown at a bulk shear strain of ≈1.

Our model results are in excellent agreement with experimental results at constant strain rate (CTR1). Stress strain curve (see Figure 20a), shear zone width and matrix deformation are very similar as shown by the passive strain markers (see Figure 20b,c). The inclusion length fits to the experimental estimate and its distorted rhomboidal shape

(Rybacki et al., 2014) is also observed in the model. Steady-state deformation is not yet reached at a bulk shear strain of $\gamma = 1$, indicated by the non-zero slope of the stress strain curve. Constant stress model and experimental results also do not differ significantly as shown in the supplements (Figure 27). In agreement with the results from Nardini et al. (2018), this test likewise indicates that both loading configurations (constant strain rate and constant stress) lead to nucleation of ductile shear zones.

The benchmark comparison also reveals a minor difference between model and experiment. When using the experimentally determined flow laws, we find that the maximum bulk shear stress of the model is $\approx 5\%$ lower than in the experiment. Likely, this offset is due to experimental uncertainties contained in the flow laws, which we level out by adopting a slightly smaller pre-exponential factor for the Solnhofen inclusion (Table 4).

3.4.2 Spatial and temporal model evolution

In this section we investigate the bulk stress evolution by analyzing the evolution of model-intrinsic strength variations that arise from the flow laws and local stress partitioning. To describe inhomogeneous deformation surrounding the shear zone tip we use the term process zone, which originates from nonlinear fracture mechanics (Zang et al., 2000). Here we expand its meaning to viscous materials describing a region of enhanced microstructural modification in comparison to the remaining matrix (Rybacki et al., 2014). To analyze the evolution of the process zone that is observed in the experiments, we visualize the stress and strain distribution in space and time. We distinguish four phases (P1–P4) during model evolution: *pre-weakening* (P1), *onset and acceleration of weakening* (P2), *deceleration of weakening* (P3) and *steady-state* (P4). In phase P1 stresses build up (loading) and no material is weakened by viscous softening, but with ongoing deformation the shear strain locally exceeds the threshold strain ε_1 defining the beginning of weakening and phase P2 at a bulk shear strain of $\gamma \approx 0.05$. From this moment on the Carrara marble matrix is subdivided into an unaltered zone A and the process zone B that is submitted to ongoing weakening (Figure 21). With progressive deformation the process zone grows and a larger volume exceeds the weakening threshold, accelerating bulk softening. At a bulk shear strain of $\gamma \approx 0.6$ the process is slowing down defining the beginning of P3. Two fully weakened regions C emerge in the model center where shear strains start to exceed ε_2 that defines the second threshold and completion of weakening (Figure 21d). In phase P4 the deformation proceeds at steady state, which is only observed for bulk shear strains $\gamma > 2$ using the reference setup. In the experiment and the benchmark model, steady state is not reached since the test is terminated at a bulk shear strain of $\gamma \approx 1$.

Pronounced stress peaks in front of the inclusion tips are observed during early stages of deformation (P1 and early P2) (see Figure 21a) resulting in higher strain rates (Figure 21g) than in surrounding matrix regions of low stress. Similar to the experimental results, strain rates in the process zone are locally increased by up to a factor of ≈ 30 in comparison

to the matrix. Due to this stress and thus strain rate differences, the finite strain threshold value ε_1 (white outline) is first exceeded at the inclusion tips where softening of the material starts. This leads to a positive feedback promoting localization. Strain rate subsequently increases further and soon the second threshold value ε_2 (black outline) is also exceeded indicating local completion of softening (see Figure 21b–f and 21h–l). Consequently, stress gradually decreases again locally between the onset outline and the inclusion (see Figure 21b and c). The stress concentrations at the inclusion tips remain

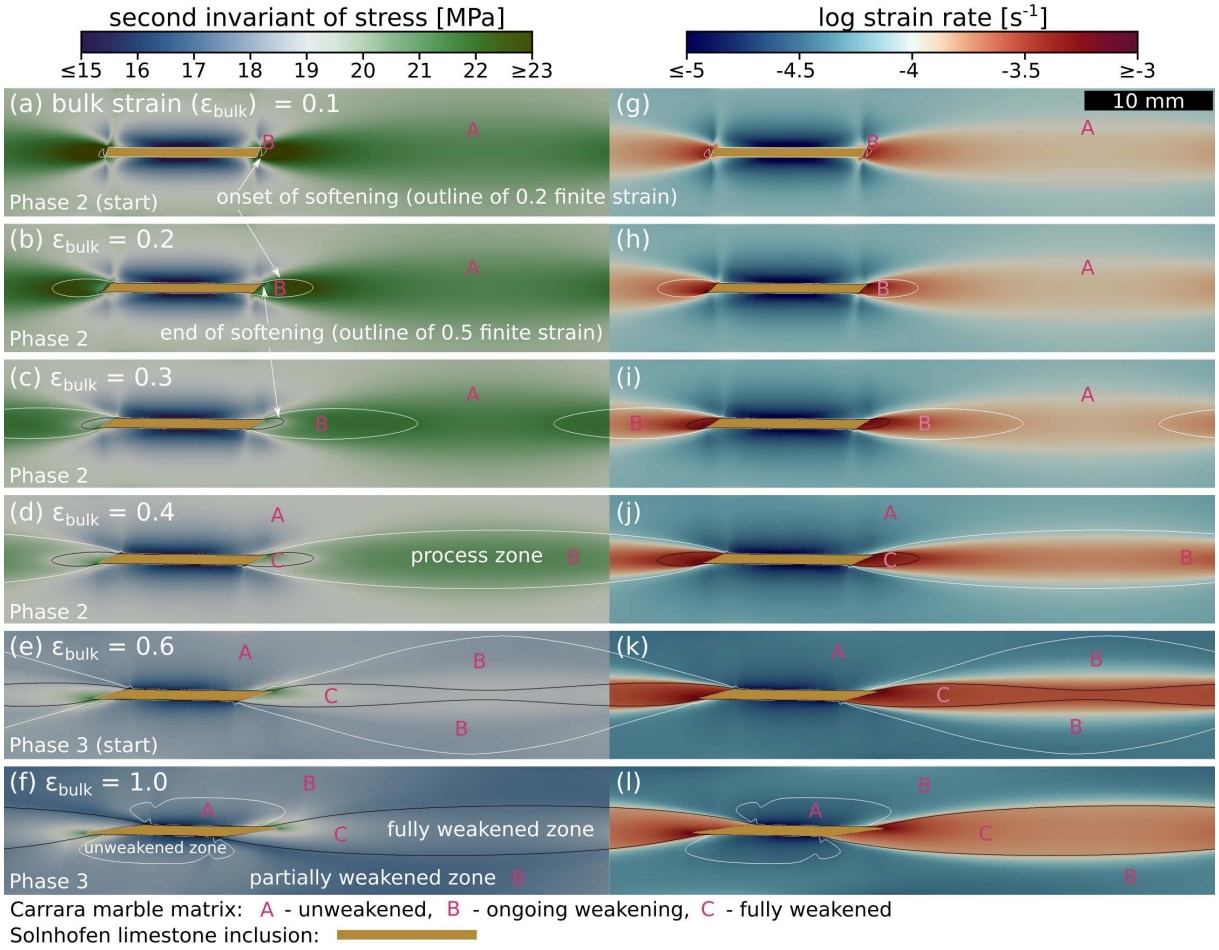

Figure 21: Local stress (second invariant of the effective deviatoric stress) (a-f) and strain rate (g-l) evolution within the matrix of the constant strain rate benchmark model. A, B and C distinguish three different Carrara marble zones and their outlines indicate finite strain thresholds of $\varepsilon_1 = 0.2$ for beginning (white) and $\varepsilon_2 = 0.5$ for end (black) of softening. The process zone B is associated with a local stress maximum propagating into the matrix (a-c). The zone is controlled by the onset and end of softening. A second stress peak remains fixed at the inclusion tips (a-f).

due to the remaining viscosity contrast between matrix and inclusion. The cylindrical symmetry of the experiment and our model results in a merge of the two weakening fronts (ε_1 outline). Once the two local stress peaks causing the onset of softening merge, they combine to a single, local stress maximum in the model center and the stress gradient in the process zone decreases significantly with further deformation (see Figure 21e). The fully weakened zones C grow, as the process zone B propagates into the matrix from the inclusion, featuring a gradual stress increase from the end of softening outline towards the inclusion tips (see Figure 21d). In phase P3 the completely weakened areas in the vertical model center are connected (see Figure 21e and k), after which the rate of

weakening decreases (Figure 20a). Stress and strain rates directly above and below the inclusion remain low throughout the experiment due to local stress partitioning. A small transition zone between the inclusion and matrix exists due to coupling of the materials. The overall observed stress drop in the matrix (Figure 21a-f) results from our weakening parameterization, which decreases the effective viscosity of the Carrara marble.

Analytical solutions of a linear dislocation in an elastic half- space predict extremely high stresses as displacements vanish towards fracture tips (Okada, 1985). Within the ductile regime and for inclusions of finite width, however, we can show that the localization process at the inclusion tip evolves in a smoother and time-dependent way. Figure 22

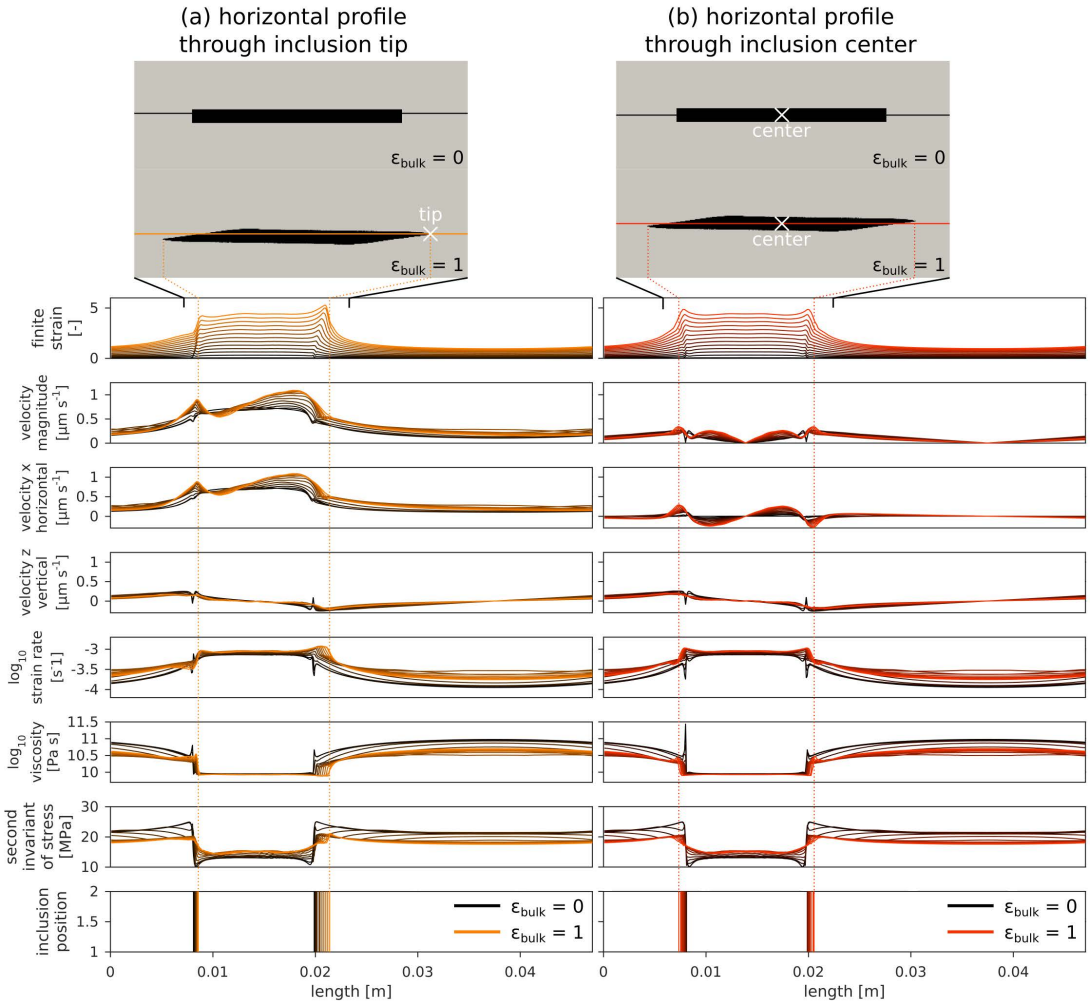

Figure 22: Along-strike variations of key variables through time. The inclusion deforms due to simple shear generating differences between horizontal profiles at various vertical positions. Here we show horizontal profiles along the center of the inclusion (at a bulk shear strain of 1) and along the center of overall model domain, which is also the center of the inclusion. a) Horizontal profile along the center of the inclusion tip. Maximum rate of deformation and accumulated finite strain are found in the inclusion tip and maximum stress in the matrix directly in front of the inclusion tip. b) Horizontal profile along the model center. Due to the symmetry of the setup, results are approximately point symmetric to the model center.

shows length profiles that display key parameter values and their evolution with increasing bulk strain along two horizontal model cross sections. The position of profile (a) is chosen such that it crosses the center of the right inclusion tip at a bulk shear strain of 1 which is 0.1 mm above profile (b) along the model center. Horizontal velocity in profile (a)

is increased, due to the vertical shift in position. By that, the point symmetry to the inclusion center is broken, which on the other hand is a feature of profile (b). Similar to a dislocation in an elastic medium, the area surrounding the inclusion tip exhibits high gradients in deformation and stress. The profiles show the highest strain rates and strains inside the weak inclusion directly at the tip. Highest stress values are however observed in the matrix in front of the inclusion. Local strain in the process zone at the inclusion tip increases approximately linear with bulk strain by a factor of ≈ 4.

3.4.3 The impact of softening on the reference model

To better constrain the effect of the viscous softening formalism, we run an additional constant strain rate model, but without the strain dependent weakening law. Besides the differences in the stress strain curves (Figure 23a), also a less pronounced shear zone development is observed (Figure 23b). This is indicated by the linearly deflected, yellow

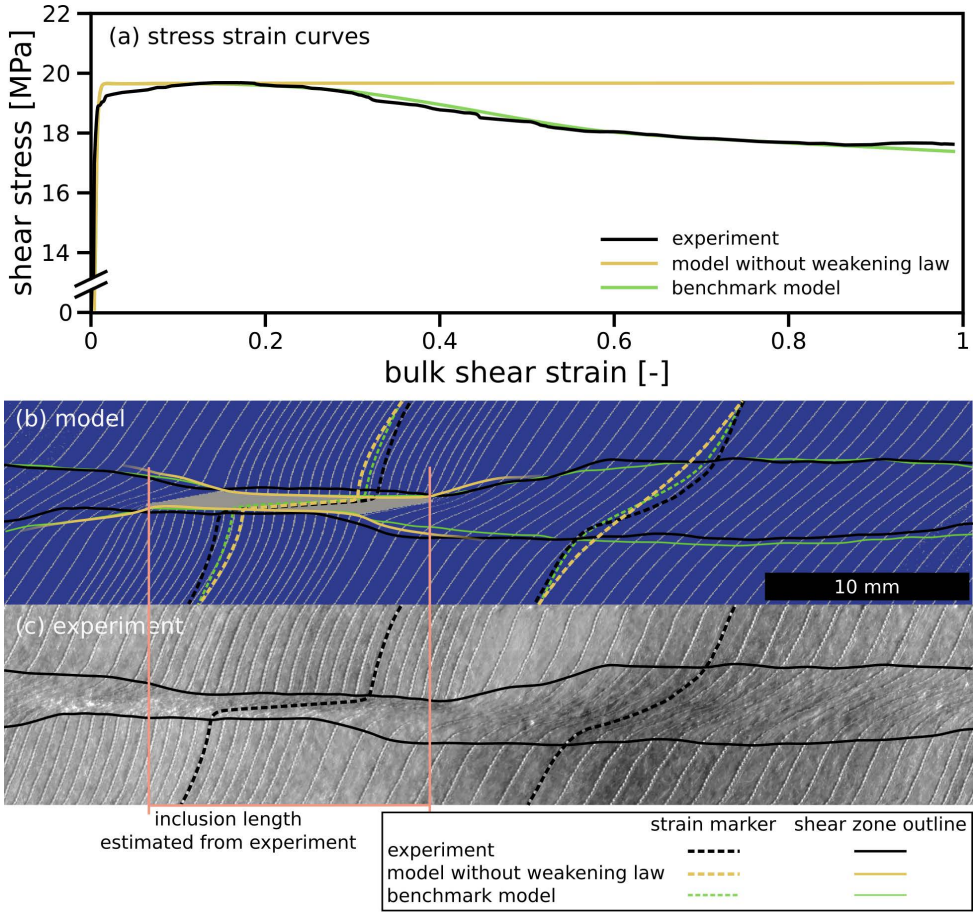

Figure 23: Comparison of model without the weakening law to experiment and reference model (same as in Figure 20c). a) Stress strain curves of model without weakening law (yellow), experiment (black) and reference model (green). b) Model without weakening law with passive strain markers and shear zone outlines of model where inferable (yellow), experiment (black) and reference model (green). c) Copper jacket from experiment with passive strain markers, estimated inclusion length and shear zone outline. Results in b) and c) are shown at a bulk shear strain of /$gamma \approx 1$. In comparison to the reference model, shear stress remains constant over time and the shear zone in the matrix is less pronounced.

strain marker crossing the matrix and the yellow shear zone outline. Strain is instead localizing mainly in the inclusion and, to a lesser extent, in the matrix close to the

inclusion tips. Nonetheless, the results of this test still show reasonable agreement with the experimental data, because the bulk weakening is generally low for the used samples and setup, which is indicated by the total shear stress drop of just $\approx$ 2 MPa in the experiment.

Additionally, we test a softening law that is based on deformation work instead of finite strain as discussed above. In this formulation, the weakening thresholds (ε_1 and ε_2, Eq. 16) are not based on finite strain, but on deformation work as defined in Eq. 17. Threshold values ε_1 and ε_2 were chosen following the iterative procedure described above for finite strain. However, we find no significant difference to the strain based softening implementation (see supplementary Figure 28).

3.4.4 The softening law parameters

This chapter addresses the effects of the softening law parameters on the localization process. We therefore vary the three controlling parameters (Figure 19b), the finite strain threshold values onset (ε_1) and end (ε_2), as well as the weakening amplitude (A).

In order to test the effect of varying A, we change this parameter between 1 and 500 leaving the remaining reference model parameters unchanged, i.e. ε_1 (0.2) and ε_2 (0.5) (Table 5). Models are conducted up to a bulk shear strain of $\gamma \approx 4$, where steady state conditions are reached in almost all cases. The reference model for instance reaches steady state at a bulk shear strain of approximately 2 (Figure 24a). Increasing A amplifies

Models for testing weakening ampliture (A)	ε_1	ε_2	$\Delta\varepsilon$	**A**
M0 - no softening	-	-	-	1
M1 - reference model	0.2	0.5	0.3	6
E1	0.2	0.5	0.3	20
E2	0.2	0.5	0.3	100
E3	0.2	0.5	0.3	500

Table 5: Parameters for models used to test the effect of the weakening amplitude (A) of the softening law.

the weakening of the Carrara marble matrix, resulting in a bulk shear stress drop and enhanced strain and thus shear zone localization, which is also indicated by a decreasing angle between inclusion and matrix shear zone (Figure 24). Large values of A increase the rate of strain localization. This is indicated by the sudden shear stress drop at a bulk shear strain of 0.4 and by faster stress peak propagation into the matrix. For values of A $>$ 50 the matrix separates into two zones of substantial viscosity contrast (Figure 24b). In another experiment, models are run up to a bulk shear strain of 4, varying ε_1 and ε_2 at constant A (Table 6). As expected, this shifts the onset and end of weakening – earlier for lower finite shear strain values and later for higher – but the actual effect on the model is not linear (Figure 25a). Note that by changing the strain range of softening $\Delta\varepsilon = \varepsilon_1 - \varepsilon_2$, the slope of the stress strain curve and thus localization rate is affected as well.

Models for testing onset and end (ε_1, ε_2)	ε_1	ε_2	$\Delta\varepsilon$	**A**
M0 - no softening	-	-	-	1
M1 - reference model	0.2	0.5	0.3	6
E1	0.0	0.5	0.5	6
E2	0.2	1.0	0.8	6
E3	0.5	1.0	0.5	6

Table 6: Parameters for models used to test the effect of onset (ε_1) and end (ε_2) of the softening law.

The reference model with the lowest $\Delta\varepsilon$ displays the fastest localization rate, because the rate with which the pre-exponential factor is increased is higher between the two thresholds due to the linear nature of the softening law. Model E2 with $\Delta\varepsilon$ of 0.8 however, reaches steady state only after a long period of ongoing softening (between 0.4 and 3.4 bulk shear strain). The local stress patterns of the tested models differ at a bulk shear strain of 1, depending on the applied threshold values. While model M0 is in the pre-weakening phase P1, model E3 and E2 are in phase P2 and model M1 and E1 already reached phase P3 approaching steady-state conditions (Figure 25b).

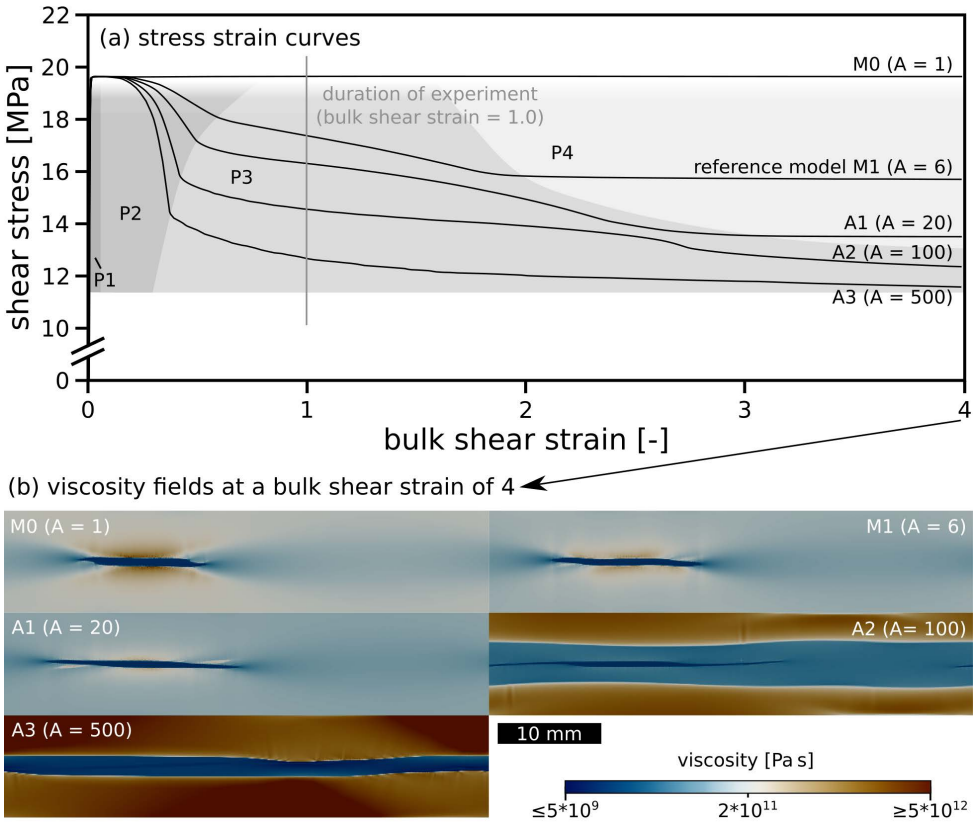

Figure 24: Effect of the weakening amplitude A. a) Stress strain curves of models with different weakening amplitude. For comparison the duration of the torsion experiment is indicated. P1–P4 refer to the phases described in ***section 3.3.4***: pre-weakening (P1), onset and acceleration of weakening (P2), deceleration of weakening (P3) and steady-state (P4). b) Viscosity fields of the models at a bulk shear strain of 4. The inclusion in the reference model is elongated further than in the model without weakening, as the matrix is increasingly deformed due to the softening law. This effect increases with A. For values of A > 50, strain localization is strongly pronounced, as shown by the viscosity field of models with a weakening amplitude A of 100 and 500. Higher values of weakening amplitude lead to stronger weakening and localization.

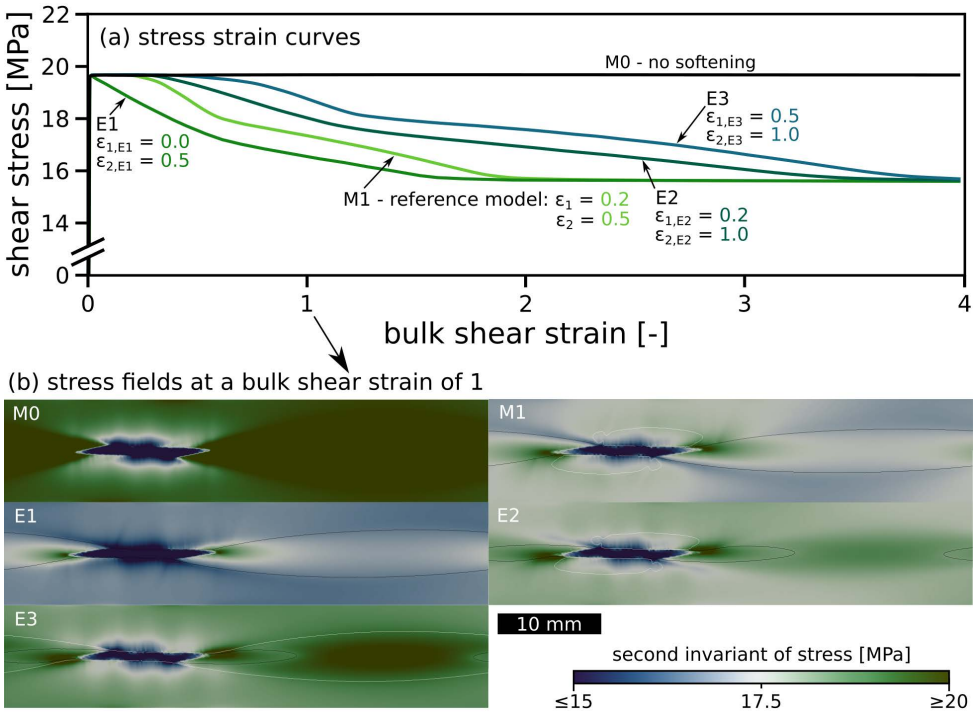

Figure 25: Effect of onset and end of weakening on the stress strain evolution. a) Stress strain curves of models with varying onset (ε_1) and end parameters (ε_2). Note the shapes of curves E1 and E3 (same $\Delta\varepsilon$) indicating a non linear relationship between threshold parameters and weakening behavior. b) Stress field (second invariant of the effective deviatoric stress) of models at bulk shear strain of 1. M0) no softening; M1) reference model; E1) $\varepsilon_1 = 0$; E2) $\varepsilon_2 = 1$; E3) $\varepsilon_1 = 0.5$ and $\varepsilon_2 = 1.0$. Models with lower ε_1 have lower bulk strengths at the same bulk shear strain.

3.4.5 Ultramylonite model - the effect of progressive softening and switch of deformation mechanism

Mylonitic shear zones often feature mm–cm wide bands with fine grain sizes referred to as ultramylonites (Hippertt & Hongn, 1998; Kenkmann & Dresen, 2002). It is commonly assumed that grain size refinement from cataclasis (Blenkinsop, 1991), dynamic recrystallization (Warren & Hirth, 2006) or mineral reactions (Herwegh et al., 2003) promotes a switch to grain size-sensitive deformation (Heitzmann, 1987; Bürgmann & Dresen, 2008). The switch to grain size-sensitive creep is transient unless grain growth is suppressed (e.g., Pearce et al., 2011), which can be achieved for example by pinning through phase mixing. In order to mimic a progressive change in mechanism, a second softening step is introduced using a similar approach as described above for the onset of weakening (Eq. 16), where we add additional strain thresholds for onset (ε_3) and end of weakening (ε_4). This second softening step is exploratory and not based any data. Configuration of the model setup and the initial onset of softening are identical to the reference model, hence earliest stages of model evolution are the same as before. The introduction of a second softening step with progressive strain, however, is expected to lead to further localization and formation of a narrow low-viscosity layer embedded in the primary shear zone. To this end finite strain thresholds for onset of weakening ($\varepsilon_3 = 1$) and completion ($\varepsilon_4 = 2$) are chosen, respectively. This procedure enables formation of a localized 'ultramylonite' band inside the active shear zone. A high weakening amplitude ($A_{um} = 20$) is chosen to enable

fast and strong localization once the threshold ε_3 is reached. Evolution of the model is

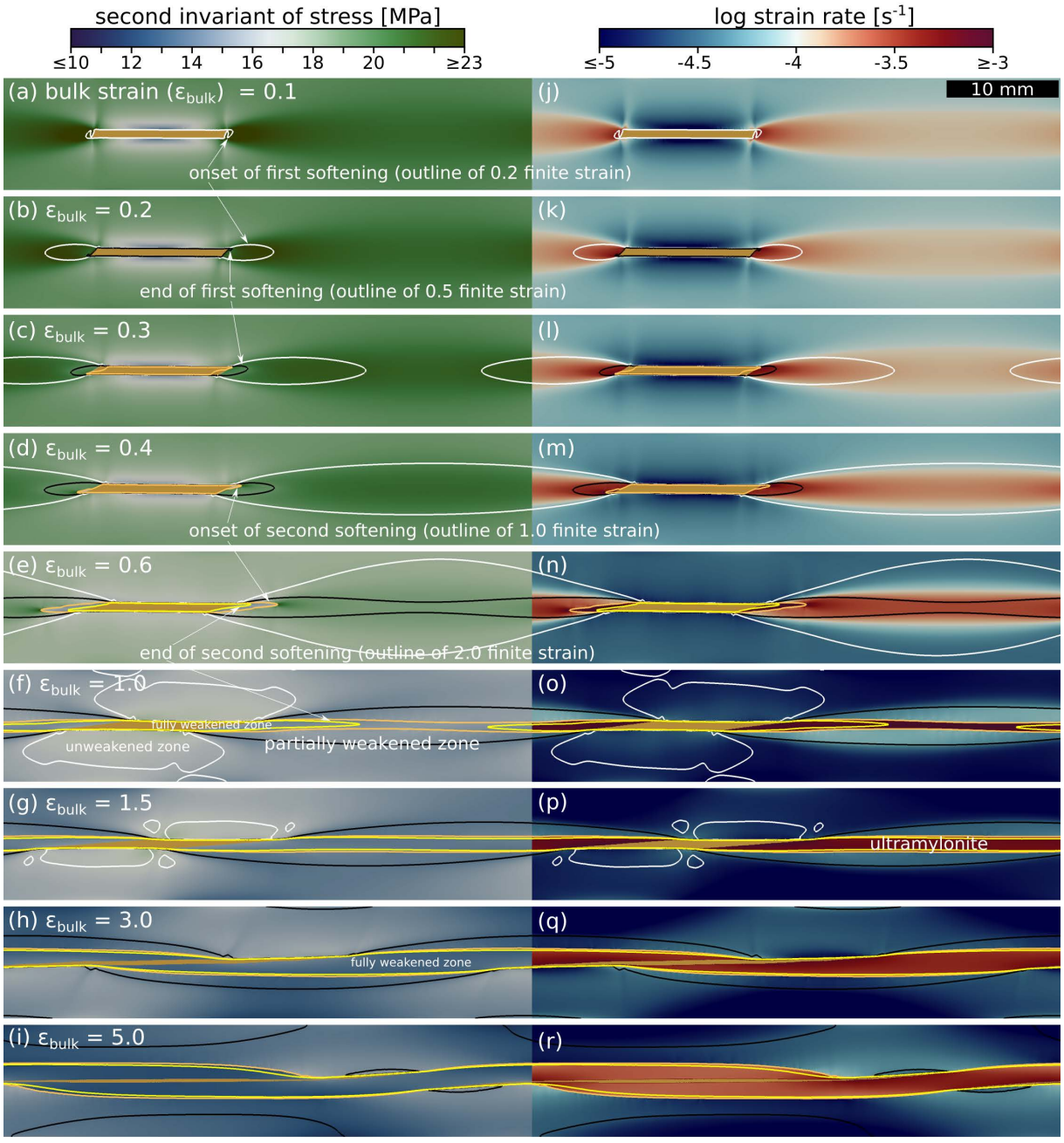

Figure 26: Local stress (second invariant of the effective deviatoric stress) (a-i) and strain rate (j-r) evolution within the matrix of the ultramylonite model. Outlines indicate finite strain thresholds $\varepsilon_1 = 0.2$ for onset of softening (white), $\varepsilon_2 = 0.5$ end of first softening stage (black), $\varepsilon_3 = 1.0$ for beginning of second stage (orange) and, $\varepsilon_4 = 2.0$ for end of second (yellow) softening stage. The onset of the second softening stage triggers evolution of further localized high strain layer (e,f,n,o) representing ultramylonite formation within a mylonite.

equivalent to the reference model for bulk shear strains less than 0.4 (compare Figure 21a-d to Figure 26a-d). Upon onset of the second softening stage, strain localizes into a narrow zone in the model center (Figure 26n,o). Inside this high strain zone, the inclusion is strongly elongated and an anastomosing pattern of the second shear zone establishes (Figure 26q,r) that additionally becomes wider with increasing bulk strain (Figure 26o-r). This transition to an anastomosing shape forms due to a rotation, which is caused by the shear deformation that the material is subjected to. Despite the simplicity of our

setup with a single inclusion, our model nevertheless captures the nested structure and the anastomosing shape of the resulting high-strain band. This agrees very well with common observations of ultramylonite bands in nature (Heitzmann, 1987; Kilian et al., 2011).

3.5 Discussion

3.5.1 Strain localization and shear zone evolution

The ductile shear zone formation observed in the experiments involves strain localization, rheological weakening of the Carrara marble and bulk strength reduction. Our numerical model reproduces these observations by employing a strain dependent viscous softening law. The model reaches steady state at a bulk shear strain of ≈ 2 in good agreement with observations from experiments (Rybacki et al., 2014). Once steady-state is reached, grain-size reduction through dynamic recrystallization and grain growth are anticipated to reach a dynamic balance (De Bresser et al., 2001), resulting in steady-state material strength. Our model results provide insight into the development of local stress, strain partitioning between matrix, inclusion and shear zone and ensuing viscosities. This provides detailed insight in the evolution of a localized shear zone that allows a direct comparison with the bulk mechanical data and microstructural observations collected from the deformation experiments. It has to be kept in mind though, that the numerical model does not feature the grain-scale resolution necessary to reproduce the brittle deformation as observed in the experiments. Nevertheless, the model successfully predicts local stress concentration and strain rate amplification ahead of the inclusion in first order agreement with the experimental results. This provides confidence to the results of the parameter study performed here, as to the magnitude of softening. This holds in particular to the results of models predicting progressive multistage softening combined with a change in deformation mechanisms, as suggested from a large number of field studies.

The nucleation of a localized shear zone at the inclusion tips involves formation of a process zone. This process zone is defined by a strong local stress concentration and resulting volume of enhanced microstructural modification (Rybacki et al., 2014). In our models this zone is represented by a 2D area showing local stress concentrations that result from the viscosity contrast between limestone and marble present at the assumed temperature conditions. The enhanced stress levels locally reduce the effective viscosity of the Carrara marble (power-law rheology) resulting in locally increased strain rates. In turn, this triggers rheological weakening causing shear strain to progressively localize in a shear zone embedded in the Carrara matrix. A localized, elliptical process zone is established, corresponding to the experiments, that displays a zone of gradually reduced grain-sizes around the inclusion tips.

3.5.2 Relating our softening parametrization to nature

The two threshold values for finite strain (ε_1 and ε_2) used in the numerical model are expected to mimic the effects that microstructural changes within the process zone have on the bulk strength of the experimentally deformed samples. As such, they are unlikely to represent specific and observable stages of the local microstructural evolution within the process zone. Strain weakening behavior is known to results from a number of different processes, e.g., dynamic recrystallization, dislocation annihilation, vacancy diffusion or lattice preferred orientation. These concur to produce the microstructural and textural modifications that can be observed in our experimental samples in proportions that are likely to vary in the course of the transient processes discussed here. A simple linear parametrization cannot be expected to capture single elements of such complexity within heterogeneously deforming samples. Our parameterization, however, appears to reproduce the phenomenological aspects of weakening as observed in our experiments with reasonably high accuracy. While it is beyond the scope of our model to pinpoint the micromechanical processes and features corresponding to specific values of local shear strain, some general observations can be made to discuss the significance of our approach. Plastic yield of the bulk assembly, suggesting the onset of strain weakening processes at the local scale, is already observed at very low values of bulk shear strain ($\approx$ 0.01-0.02, cf. Fig. 4 in Nardini et al., 2018) corresponding to a local strain of $\approx$ 0.1-0.2 at the tip of the inclusion (cf. Fig. 6a in Nardini et al., 2018), which is in the range of our selected ε_1. It is important to notice that the process zone forming along the weak inclusion plane is intrinsically transient both on a temporal and spatial level. The heterogeneity-induced viscosity contrast produces a volume of stress enhancement (e.g. Fig. 21), which evolves with bulk shear strain and determines a strongly heterogeneous strain distribution (Fig. 6 in Nardini et al., 2018). Similarly to what would be expected in the brittle regime for slip-weakening behavior, an area of strength perturbation is developed. It is characterized by higher strain rates and increasing microstructural changes closer to the inclusion: the extent of such a perturbation may determine the value of ε_2, i.e. the "end of weakening" in our softening law. Whether or not, in a non-steady-state shear zone like is the case in our experimental samples, a microstructural and/or textural signature would be associated at all times with the varying volume of perturbed material is questionable. It is therefore reasonable to conclude that, while a definite one-to-one correlation between the described finite strain threshold values and specific microstructural changes is not possible, these parameters are still able to capture the bulk mechanical expression of the strain weakening processes locally activated in the microstructures.

3.5.3 Scope and limitations of strain softening parametrization

The advantage of employing a simple, first-order softening law is to keep numerical complexity low, which is not only more transparent, but also saves computational time in

large-scale models (e.g. Huismans & Beaumont, 2003; Brune et al., 2014). In an attempt to model rock weakening and strain localization, different types of softening parameterizations have been previously used in order to describe the weakening behavior of natural materials. For example, Gardner et al. (2017) studied strain localization using different load bearing framework geometries. They found that interconnected weak layers are hard to form without a dynamic weakening process, which was also observed in an experimental study by Holyoke III and Tullis (2006). This agrees with our results showing that pronounced shear zone formation in the matrix only occurs for materials with an implemented weakening formalism simulating progressive material softening. This implies the necessity of using softening laws to properly model strain localization and thus shear zone formation. Gardner et al. (2017) used a different implementation to simulate weakening. They introduced stress dependent softening combined with time dependent hardening focusing on the transition from non-linear to linear flow. At larger scale, Mazzotti and Gueydan (2018) pointed out the fundamental role of inherited tectonic structures for strain and seismicity concentrations in an intraplate setting. Similar to our study, their model also includes irreversible softening (no counteracting hardening mechanism). However, in their model softening is achieved by changing the material yield stress instead of the pre-exponential factor in a constitutive law, as in this study.

In large-scale rock deformation, there are several major effects that may play an important role affecting localization and shear zone formation and that need to be considered in numerical modelling studies. These are highly non-linear processes such as shear heating (Thielmann & Kaus, 2012; Duretz et al., 2015; Foley, 2018), melting (Dannberg & Heister, 2016; Schmeling et al., 2017) or a switch to grain-size sensitive diffusion creep, like modeled in our study (e.g. Handy, 1989). In that aspect, our models provide a minimum constraint to the degree of viscous strain softening that can be expected to act in nature. Another important point is that numerical models of brittle deformation often involve a strong mesh-dependency (De Borst & Mühlhaus, 1992) such that the softening parameters have to be adopted to the chosen resolution. However, this is not the case when modeling viscous deformation where the size of the process zone as well as the bulk shear stress evolution and employed softening parameters (ε_1, ε_2, A) are almost independent of the model resolution.

3.6 Conclusions

Strain localization in shear zones is an important process in lithosphere dynamics occurring over a broad range of spatial scales. For simplicity, we use a piece-wise linear softening law and show that it is capable of reproducing rheological weakening observed in laboratory experiments. Our model provides a virtual way of analyzing the viscous process zone evolution that can be divided into four phases (P1) *pre-weakening*, (P2) *onset and acceleration of weakening*, (P3) *deceleration of weakening* and (P4) *steady-state*.

Spatial stress distributions show that matrix strain localization is initiated by a local stress peak at the inclusion tips. From there and with increasing strain, the process zone expands into the matrix. Shear zone width and localization rate are controlled by the amount of rheological weakening. Our numerical models show that rheological weakening is necessary to establish a pronounced shear zone in a strong matrix surrounding a weak inclusion and to explain the anastomosing shape and the nested structure of ultramylonites. This reinforces the importance for geodynamic models to contain softening laws that appropriately account for rheological weakening.

Acknowledgements

This manuscript has been greatly improved thanks to the constructive comments and suggestions of Andrew Cross, an anonymous reviewer, and associate editor Bjarne Almqvist. This study was conducted within the Helmholtz Young Investigators Group CRYSTALS (VH-NG-1132). Laboratory experiments were performed in Geomechanics and Rheology section of the German Research Centre for Geosciences and we thank Stefan Gehrmann for help with sample preparation. Simulations were performed on the cluster facilities of the German Research Centre for Geosciences. All data that this numerical study is based on is found in Figure 19 and the parameter Tables 4,5&6. Additional data regarding the torsion experiment is found within Nardini et al. (2018). Figures were created using Paraview and Matlab and color maps were taken from Crameri (2018).

Supplementary material

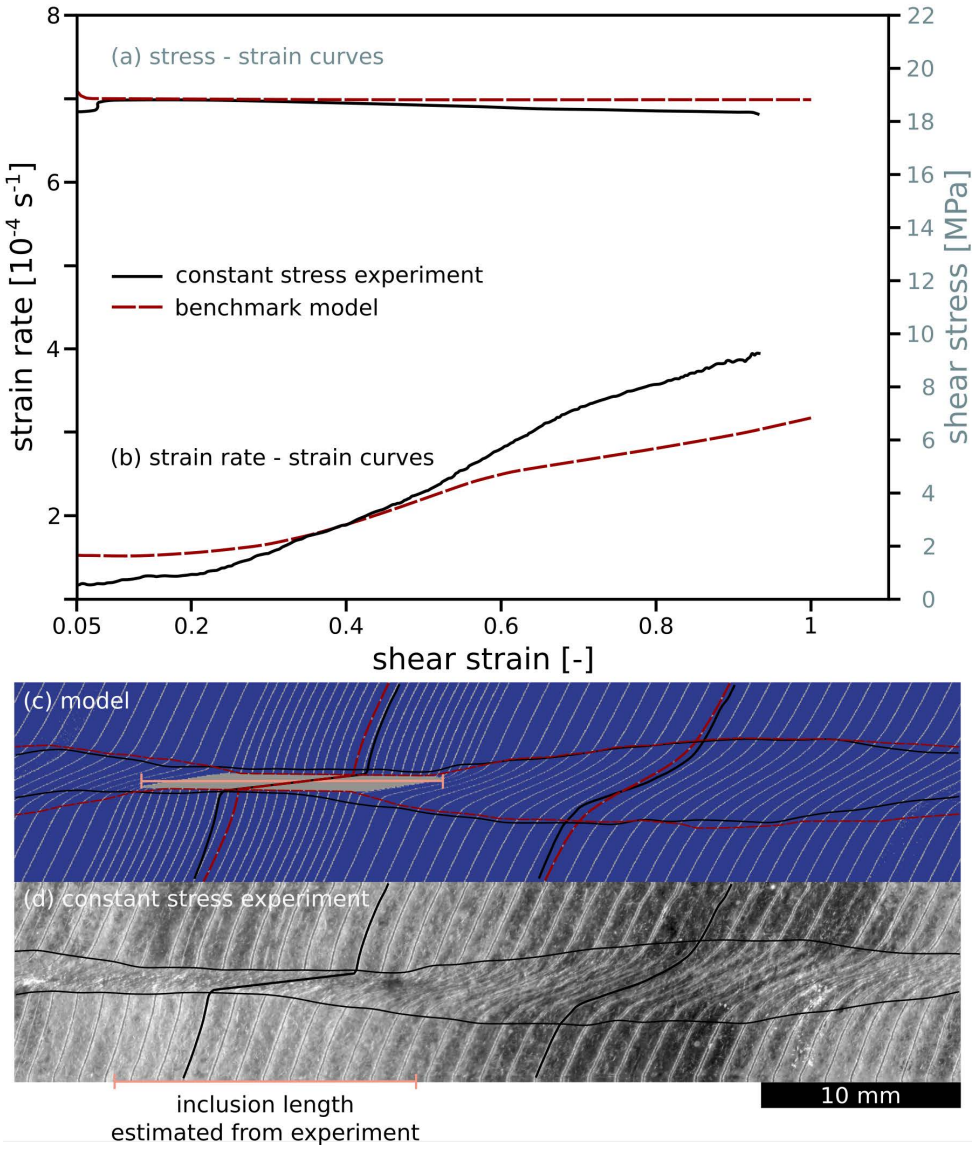

Figure 27: Comparison of constant stress model to experiment. a) Stress strain curves of model (red) and experiment (black). b) Strain rate plot over strain. c) Model with passive strain markers and shear zone outlines of model (red) and experiment (black). d) Copper jacket from experiment with passive strain markers, estimated inclusion length and shear zone outline. Results in c) and d) are shown at a bulk shear strain of 0.93.

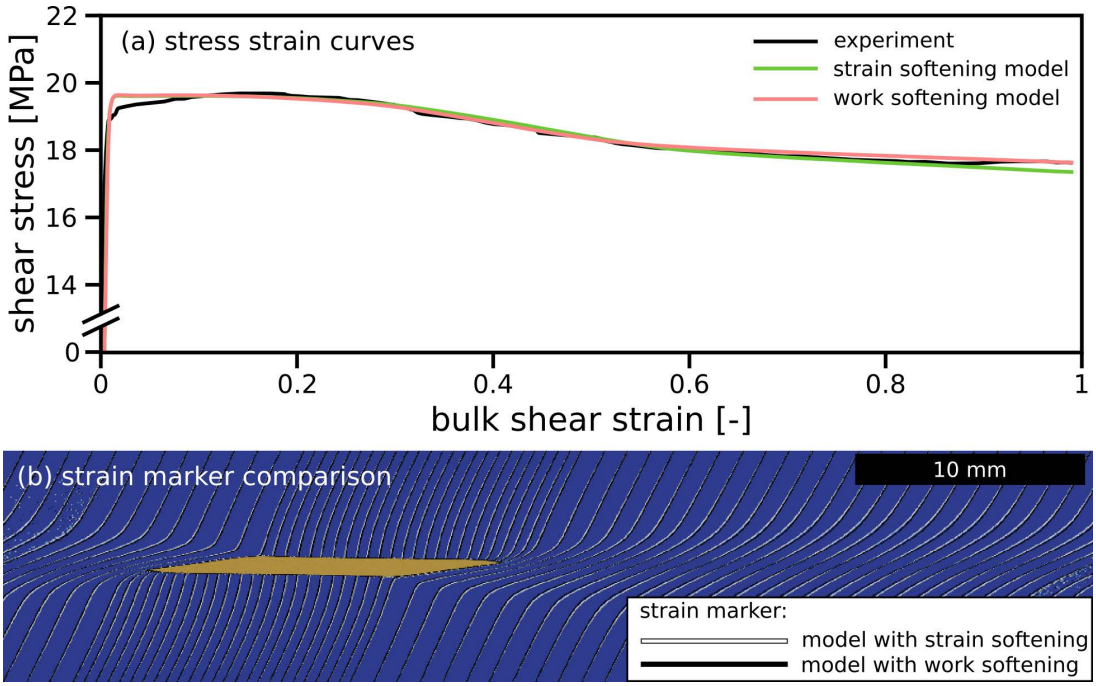

Figure 28: Comparison of strain and deformation work based weakening implementations with constant strain rate boundary conditions. a) Stress strain curves of strain weakening model (green), work weakening (purple) and experiment (black). b) Strain marker comparison between strain dependent (white) and work dependent (black) implementation of softening, showing almost identical results

4 Control of the geometric arrangement of material heterogeneities on strain localization at the brittle-to-ductile transition

Summary

Triaxial high temperature (900 °C) deformation experiments were conducted at constant strain rate in a Paterson-type deformation apparatus on cylinders of Carrara marble with two right or left stepping, non-overlapping weak inclusions of Solnhofen limestone, oriented at 45° to the cylinders' longitudinal axes. Applying different values of confinement (30, 50, 100 and 300 MPa) we induced various amounts of brittle deformation in the marble matrix and investigated the effect of brittle precursors on the initiation and development of heterogeneity-induced high temperature shear zones. Viscosity contrast between the matrix and the inclusions induces local stress concentration at the tips of these latter. Interaction of the stress fields results in a mean stress of either extensional or compressional nature, depending on the geometrical arrangement of the inclusions. At low confinement (30 and 50 MPa) abundant brittle deformation is observed, but the spatial distribution of microfractures is dependent on the kinematics of the step-over region: microcracks occur either along the shearing plane between inclusions (extensional samples), or broadly distributed outside the step-over region (compressional configuration). Accordingly, ductile deformation localizes along the inclusions plane in the extensional geometry as opposed to distributing over large areas of the matrix in the compressional samples. If microcracking is suppressed (high confinement), strain is accommodated by viscous creep and strain progressively de-localizes in extensional samples. Our experiments demonstrate that brittle precursors enhance the degree of localization in the ductile deformation regime, but only if the interaction of pre-existing heterogeneities induces an extensional mean stress regime in between.

4.1 Introduction

In the past decades, the study of the mechanical behaviour of rocks within the Earth's lower crustal levels has led to intense discussion on the nature and extent of the brittle-to-ductile transition, seen as the change in dominant deformation mechanisms operating in rocks as temperatures and pressures increase with increasing depth. Classic interpretations predict a transition zone where rheological behaviour of rocks changes from pressure-dependent frictional sliding to thermally-activated viscous creep (Brace & Kohlstedt, 1980; Evans & Kohlstedt, 1995; Kohlstedt et al., 1995; Bürgmann & Dresen, 2008). Compelling evidence, however, has been brought forward for the occurrence of seismicity at depth in the crust, sometimes down to Moho depth, where typical models of rheological behaviour would infer a hot, weak lower crust deforming plastically (e.g., Maggi, Jackson,

Mckenzie, & Priestley, 2000; Maggi, Jackson, Priestley, & Baker, 2000; Fagereng, 2013). In such environments, observations of mutually overprinting brittle and ductile deformation are abundant (e.g., Pennacchioni & Cesare, 1997; Pittarello et al., 2012; Menegon et al., 2017) and the interplay between viscous shearing and frictional sliding appears to be cyclic, governed by significant feedback effects between the two mechanisms. Experimental and modeling work investigating the characteristics of the brittle-ductile transition in natural rocks is abundant. In particular, the topic of the bulk rheological behaviour of bi(multi)-mineralic aggregates with components displaying different strength has been investigated in many studies over the years (e.g., Jordan, 1987; Handy, 1990; Dresen & Evans, 1993; Handy, 1994; Handy et al., 1999; Jessell et al., 2009; Auzende et al., 2015; Jammes et al., 2015). These studies, however, aim at characterizing the bulk behaviour of polyphase aggregates rather than exploring the microstructural and microphysical processes associated with small scale mechanical heterogeneities.

Ductile shear zones are a multiscale feature ubiquitous within the Earth's crust (Ramsay & Graham, 1970). The very existence of shear zones has been suggested to be a necessary condition for the presence of plate tectonics on our planet (Bürgmann & Dresen, 2008). Understanding the processes leading to shear zone nucleation and their rheological behaviour is important to unfold the mechanisms of stress transfer at depth in the Earth's crust and ultimately of the earthquake cycle (Bürgmann & Dresen, 2008). Through processes like grain size reduction and fluid channelling, brittle fracturing has been shown to facilitate strain weakening and ductile localization of strain in the high temperature domain, both when present as a precursor (e.g., Tremblay & Malo, 1991; Christiansen & Pollard, 1997; Guermani & Pennacchioni, 1998; Mancktelow & Pennacchioni, 2005; Pennacchioni & Mancktelow, 2007) and when occurring concomitantly with crystal-plastic processes (Fusseis et al., 2006; Fusseis & Handy, 2008; Goncalves et al., 2016).

The presence of pre-existing heterogeneities in largely homogeneous rock bodies is common in natural rocks. For example, rock formation processes inherently produce large amounts of defects, voids and inclusions. Brittle processes will generate planes of weakness (fractures and faults) at different times within the tectonometamorphic evolution of a rock mass such as jointing and veining of cooling intrusive plutons (e.g. Mancktelow & Pennacchioni, 2005). Deep crustal seismic slip generating pseudotachylites (e.g. Menegon et al., 2017) and episodic fracturing at the brittle-to-ductile transition (e.g. Fusseis & Handy, 2008) are examples of brittle processes occurring prior to (or concomitant with) viscous flow.

Here, the interplay between brittle and ductile deformation, its effect on the nucleation of high temperature shear zones and on the localization of deformation in the ductile regime in samples containing material heterogeneities is investigated. Samples of Carrara marble containing pairs of weak limestone inclusions arranged to form step-overs of different kinematic nature are deformed in triaxial compression at varying confining pressures. We find combined brittle and ductile deformation is occurring at conditions of low ef-

fective confining pressures regardless of the kinematics of the step-over geometry, while increasing confining pressure substantially suppresses the brittle component. Ductile localization assisted by brittle processes is observed whenever these latter attain themselves a favourable heterogeneous distribution at the time of formation.

4.2 Experimental setup

A series of high-temperature triaxial experiments were run on monomineralic Calcite specimens, composed of Carrara marble containing Solnhofen limestone inclusions. The sample configuration has been tested in previous studies (Rybacki et al., 2014; Nardini et al., 2018). Carrara marble forms the sample matrix, displaying an almost complete

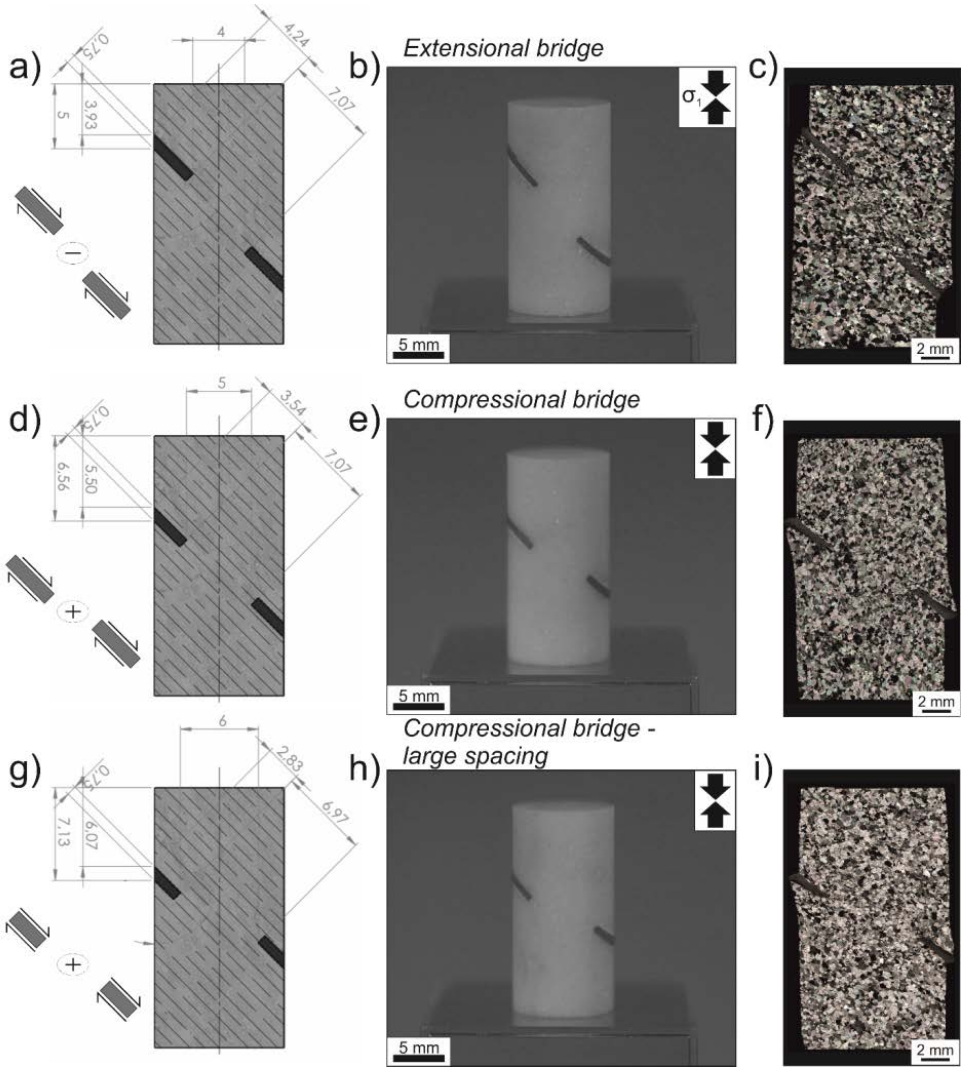

Figure 29: Three different sample configurations are employed in the experimental series. a), d) and g) represent 2D sketches with accurate measurements given in mm and b), e) and h) show pre-deformation pictures of the samples, while in c), f) and i) are the optical overviews of thin sections produced from the deformed specimens. The region between the inclusions are expected to deform in the extensional (a-c) and compressional (d-i) regime. While a-c and d-f only differ in the relative placement of the Solnhofen limestone inclusions, in g-i both the vertical and the in-plane distance between the inclusions are increased. Note that, in all cases, a 45° angle is formed between the cylinders' long axes and the planes where the inclusions lay.

absence of impurities (> 99% $CaCO_3$), low to no initial porosity and uniform initial

grain size ($\approx$ 150 μm). Moreover, the abundance of grain triple junctions, straight grain boundaries and the uniform initial crystallographic orientation distribution point to very low degrees of stored strain in the starting material (e.g., Rutter, 1995; Pieri, Burlini, et al., 2001; Pieri, Kunze, et al., 2001). Solnhofen limestone is characterized by high purity (97% $CaCO_3$, see Rutter, 1972) and very fine starting grain size ($\approx$ 5 μm). The inclusions (also a common experimental material, e.g. Rutter, 1972; Schmid et al., 1980, 1987) are placed in homogeneous Carrara marble. Solnhofen limestone is up to $\approx$ 20 times weaker than Carrara marble in compression at the high temperatures employed in our experiments (900 °C, Rybacki et al., 2014). The resulting large viscosity contrast leads to high stress concentrations inducing weakening processes and strain localization in the Carrara marble matrix.

The triaxial sample configuration is composed of a Carrara marble cylinder with 10 mm diameter and 20 mm in length. Two semi-circular inclusions of Solnhofen limestone are inserted in corresponding saw cuts within the cylinders as shown in Fig. 29. Note that the cuts are oriented at 45° to the cylinders' long axes and to the maximum and minimum stress directions σ_1 and σ_3, respectively. The presence and positioning of the two inclusions facilitates the formation of a shear zone, expected to mimic the common occurrence, in nature, of sets of pre-existing planar material heterogeneities that get exploited during ductile deformation and lead to the formation of "bridges" of highly deformed material within the host rock (e.g., Mancktelow & Pennacchioni, 2005; Pennacchioni & Mancktelow, 2007).

Three different sample configurations have been used in our study (Fig. 29). The positioning of the inclusions is designed to produce different kinematic conditions in the "deformational bridges", the area of the matrix comprised between the inclusions. Depending on the relative positioning of the inclusions with regard to the shear direction, extensional (Fig. 29a-b) or compressional (Fig. 29c-f) deformation zones are formed between the inclusions, respectively. We also varied the distance between the inclusions (Fig. 29d-e) to modify the intensity of their mutual interaction.

4.3 Methods

4.3.1 Experimental series

Constant strain rate experiments at different confining pressures were run in a Paterson-type gas deformation apparatus (Paterson, 1970). Temperature and strain rate were kept constant at 900 $\pm$ 2 °C and 7.2×10^{-5} s^{-1}, respectively. The confining pressure was varied between two end-member values of 30 and 300 MPa (Table 7). The samples were sealed by a thin copper jacket from the gas confining medium (Argon) and a correction for jacket strength was applied to the measured force, which was then converted to axial stress assuming constant volume deformation.

Axial strain was derived from axial displacement with a correction for system com-

Sample number	Inclusion l × z [mm], angle	Sample config.	P [MPa]	Shear (axial) $\dot{\varepsilon}$ [s^{-1}]	Shear (axial) stress [MPa]	Max shear (axial) ε [MPa]	EBSD
CMAS-17	4.24 × 0.75, 45°	EB	30	1.3×10^{-4} (7.2×10^{-5})	6.3 (12.5)	0.73 (0.02)	X
CMAS-23	4.24 × 0.75, 45°	EB	30	1.3×10^{-4} (7.2×10^{-5})	6.7 (13.3)	1.80 (0.05)	X
CMAS-16	4.24 × 0.75, 45°	EB	30	1.3×10^{-4} (7.2×10^{-5})	6.2 (12.3)	3.66 (0.10)	X
CMAS-12	4.24 × 0.75, 45°	EB	50	1.3×10^{-4} (7.2×10^{-5})	6.4 (12.7)	0.71 (0.02)	X
CMAS-13	4.24 × 0.75, 45°	EB	50	1.3×10^{-4} (7.2×10^{-5})	6.8 (13.5)	1.84 (0.05)	X
CMAS-14	4.24 × 0.75, 45°	EB	50	1.3×10^{-4} (7.2×10^{-5})	8 (16)	3.57 (0.09)	X
CMAS-18	4.24 × 0.75, 45°	EB	100	1.3×10^{-4} (7.2×10^{-5})	9.3 (18.6)	0.59 (0.02)	
CMAS-19	4.24 × 0.75, 45°	EB	100	1.3×10^{-4} (7.2×10^{-5})	9.6 (19.1)	1.82 (0.05)	
CMAS-20	4.24 × 0.75, 45°	EB	100	1.3×10^{-4} (7.2×10^{-5})	10.3 (20.6)	3.50 (0.09)	X
CMAS-21	4.24 × 0.75, 45°	EB	300	1.3×10^{-4} (7.2×10^{-5})	9.9 (19.8)	1.79 (0.05)	
CMAS-22	4.24 × 0.75, 45°	EB	300	1.3×10^{-4} (7.2×10^{-5})	12.2 (24.3)	3.53 (0.09)	X
CMAS-24	3.54 × 0.75, 45°	CB	30	1.3×10^{-4} (7.2×10^{-5})	7.5 (15)	3.63 (0.10)	
CMAS-26	3.54 × 0.75, 45°	CBLS	30	1.3×10^{-4} (7.2×10^{-5})	9.2 (18.4)	3.56 (0.09)	X
CMAS-25	2.83 × 0.75, 45°	CB	100	1.3×10^{-4} (7.2×10^{-5})	13.2 (26.3)	3.53 (0.09)	X
CMAS-27	2.83 × 0.75, 45°	CBLS	100	1.3×10^{-4} (7.2×10^{-5})	12.2 (24.3)	3.61 (0.10)	X
CMP-01	–	Solid	30	1.3×10^{-4} (7.2×10^{-5})	8.7 (17.3)	– (0.30)	
CMP-02	–	Solid	100	1.3×10^{-4} (7.2×10^{-5})	14.8 (29.6)	– (0.30)	
CMP-03	–	Solid	50	1.3×10^{-4} (7.2×10^{-5})	15.7 (31.3)	– (0.30)	
CMP-04	–	Solid	100	1.3×10^{-4} (7.2×10^{-5})	14.0 (27.9)	– (0.30)	
CMP-05	–	Solid	50/100	1.3×10^{-4} (7.2×10^{-5})	12.3 - 15.1 (24.5 - 30.1)	– (0.049 - 0.050)	
CMP-06	–	Solid	30	1.3×10^{-4} (7.2×10^{-5})	9.8 (19.6)	– (0.30)	
CMP-07	–	Solid	300	1.3×10^{-4} (7.2×10^{-5})	13.9 (27.8)	– (0.30)	

Table 7: Experimental conditions. Sample configurations are the following: EB: extensional bridge; CB: compressional bridge; CBLS: compressional bridge – large spacing; Solid: inclusion free, solid Carrara marble sample. Note that CMP-05 is a stepping experiment conducted at 50 and 100 MPa, respectively.

pliance. Shear strain and shear stress along the inclusion plane were derived from their axial equivalent (ε and σ, respectively) following:

$$\gamma = \frac{\varepsilon L}{d \cos(\alpha)} \tag{18}$$

and

$$\tau = \frac{1}{2} \sigma \sin(2\alpha) \tag{19}$$

where L and d are the initial sample length (20 mm) and inclusion thickness (0.75 mm), respectively, while α (= 45°) is the angle between the inclusion and the cylinder's long axis (Tembe et al., 2010). These calculations are valid for low strain, while correction would be required in the case of larger applied strains.

The microstructural evolution was analyzed by investigating discrete strain intervals, namely ≈ 2, 5 and 10% axial strain. Both heating and cooling rates were ≈ 30 °C/min, and the actuator load was maintained during cooling to preserve the deformation microstructures and avoid (where possible) substantial healing during unloading.

Samples were tested at four different confining pressures of 30, 50, 100 and 300 MPa. Although Carrara marble is known to deform at 900 °C temperature and 300 MPa confining pressure by crystal-plastic processes (e.g., Schmid et al., 1980; Rutter, 1995; Pieri, Burlini, et al., 2001; Rybacki et al., 2014) at low confinement brittle cracking is expected where stresses are concentrated at the inclusion tips (Fredrich et al., 1989). The "extensional bridge" configuration samples were tested over the entire range of confining pressures, while the two representative conditions of 30 and 100 MPa were applied to the "compressional bridge" and "compressional bridge – large spacing" configurations. See Table 7 for details of the experimental conditions.

4.3.2 Local shear strain estimation

To estimate the local shear strain of samples deformed to different bulk axial strain and sample configurations, a series of passive markers on the copper jackets were placed in the area between the two inclusions. Thin hollow half-cylinders were 3D-printed using a plastic polymer and fit around the copper jackets (Fig. 30a). They contain a series of openings with ca. 1 mm spacing and 45° inclination to the long axis of the cylinder; such openings were used to prepare straight markers on the jackets. After the experiments but before retrieving the samples, pictures and scans of the jackets were acquired (Fig. 30b and c). By measuring the angular deflection of the markers with respect to the initial orientation, local values of shear strain within the Carrara marble matrix were derived with distance from the limestone inclusions. Note that a non-negligible error is inherently carried by such angular measurements (e.g. at these values of shear strain a difference of 5° in the measured angle results in a change of shear strain of about 0.1). Furthermore, potential misalignments of markers with the target area of the cylindrical samples once

the jackets were in place was hard to verify. Therefore, the accuracy of the local shear strain measurements is rather uncertain.

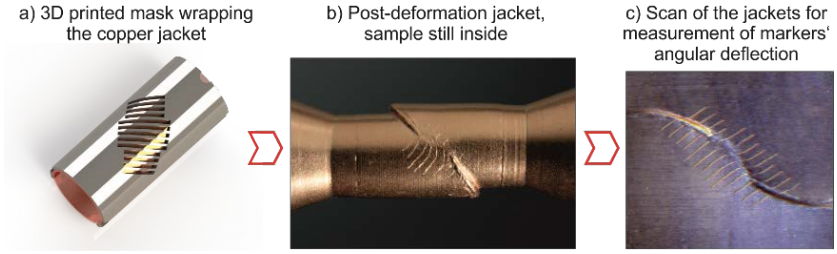

Figure 30: Example of the strain markers design that was used during the experiments to calculate the evolution of local shear strain. The plastic mask that was used to carve straight marks on the jackets' surfaces is shown in a, while in b and c the post-deformation result is displayed.

4.3.3 Analysis of microstructures

Thin sections were cut parallel to the long axes of the cylindrical samples and across the centres of the semi-circular inclusions and were mechanically polished with diamond paste (≈ 30 μm thickness). Final smoothing of the surfaces was achieved with a one-hour treatment in an alkaline solution of colloidal silica. Optical analysis of microstructures was conducted at a Leica DMRX with objective lenses $\times 2.5$, $\times 10$, $\times 20$, $\times 50$ and $\times 100$ and equipped with a DMC4500 high resolution color camera. Twin density calculations were carried out on the extensional bridge confining pressure samples series at 5 and 10% bulk axial strain conditions. Following Rowe and Rutter (1990), twin density was measured as the number of twin lamellae (belonging to the same twinning system) are present along a grain diameter measured perpendicular to the trace of the twins.

Crystallographic orientation mapping via automated indexation of electron backscatter diffraction (EBSD) patterns was carried out in a FEI Quanta 3D FEG dual beam machine with a EDAX-TSL Digiview IV EBSD detector. Overview EBSD maps were acquired for several samples. The specimens were uncoated and SEM parameters were: 20 kV accelerating voltage, 23 nA beam current, 8 μm step size and between 14 mm and 17 mm working distance. Processing and indexing of the patterns was carried out using the TSL software OIM 5.31. A clean-up routine of the raw data was performed through the TSL software OIM analysis 7.3. The routine involves a neighbouring confidence index (CI) correlation step with a minimum CI of 0.1, followed by a grain CI standardization (minimum tolerance angle 10° and minimum grain size of 6 pixels) and a subsequent further neighbour CI (> 0.2) step. The resulting maps were analysed for distribution and quantification of intracrystalline deformation with the mtex toolbox for Matlab (Hielscher & Schaeben, 2008; Bachmann et al., 2010). Grains were computed in mtex based on the following parameters: minimum misorientation angle of 10° and a minimum size of 6 pixels to avoid misindexing. "Mis2mean", an mtex property expressing the misorientation of a pixel with respect to the mean orientation of the grain it belongs to, is used for the

computation of grain orientation spread (GOS) values. Each grain in the map is assigned a GOS value which is the average of the "mis2mean" of all the pixels within the grain.

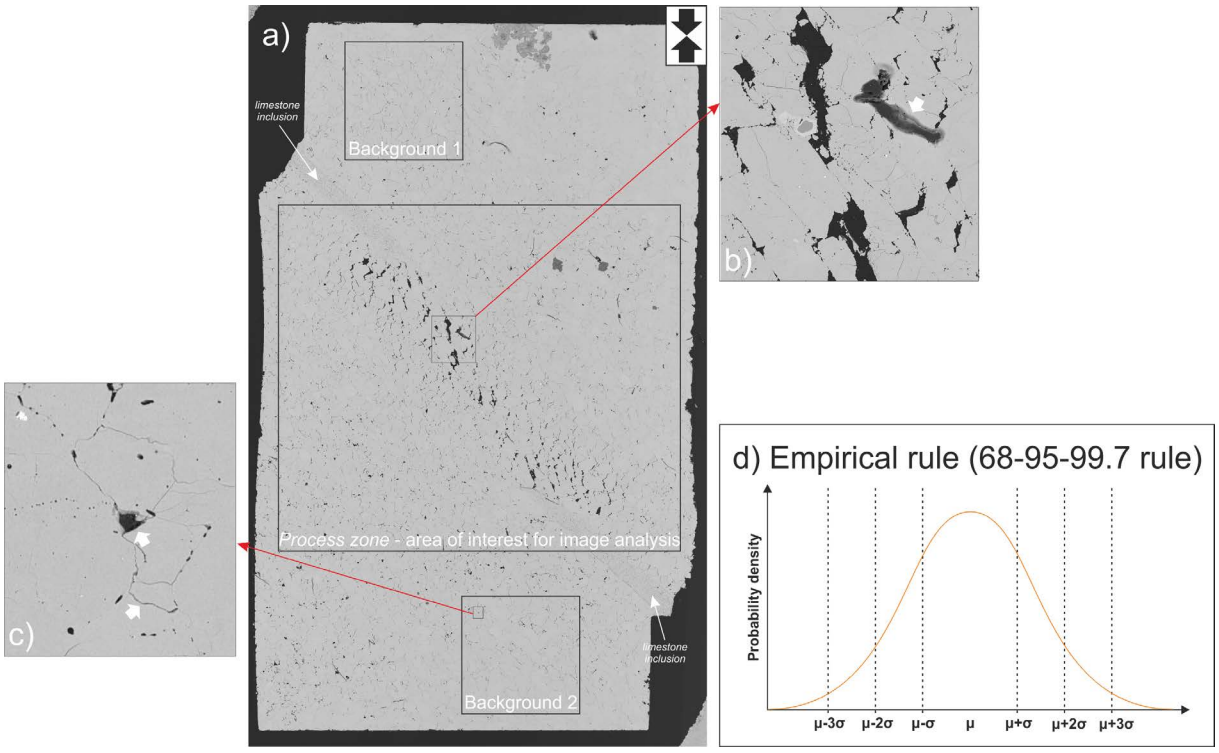

Figure 31: Example of a BSE overview image (sample CMAS-16 - 30 MPa and $\varepsilon_{bulk} \approx 0.10$) (a), illustrating fractures and grain sliding in the process zone (b) and background damage (c). Rectangles in a) show the areas that are considered for the calculation of the background 'noise' (following the statistical criteria of the empirical rule, as shown in d) and the process zone rectangle over which the image analysis of the brittle features has been conducted. See text for further explanation.

Sections of the six samples deformed to the highest axial bulk strain ($\varepsilon \approx 0.10$) and of the three lowest bulk strain samples ($\varepsilon \approx 0.02$) were carbon coated and mapped in a ZEISS Ultra Plus Field Emission-Scanning Electron Microscope equipped with an in-column Backscatter Electron Detector (BSE). The resulting overview micrographs, acquired at resolutions ranging from 1:0.744 to 1:1.117 pixel to μm and with an average single image overlap of $\approx$ 10%, were analysed using Fiji (an image-processing package of the image analysis software ImageJ, https://imagej.nih.gov/ij/) for identification of fractures and voids.

Overview images display a critical signal to noise ratio that requires signal conditioning (Fig. 31); some of the criticalities related to the heterogeneity of the background noise are pointed out in Figure 31b-c. The cleaning-up approach applied to all the BSE overviews analysed is shown (Fig. 31d). The term noise does, in this case, encompass a number of different features that are not considered relevant to the analysis of syn-deformational brittle fractures (tensile and shear cracks). Examples are dust particles on the thin section surface (arrow in Fig. 31b), pseudo-triangular shaped holes located at triple points (which are indicative of crystal damage from polishing) and partially opened grain boundaries (arrows in Fig. 31c); these features appear in the overview images in a darker shade of grey than the calcite crystals and are therefore computed as "particles" by the image analysis

software. To remove most of this noise, we first defined a rectangle (9×10 mm) centred in the space between the two inclusions (process zone in Fig. 31a), where the brittle deformation induced during the experiments is expected to be concentrated. Secondly, to estimate the distribution of noise particles that constitute the background of the image, we selected two small squares (3×3 mm, also shown in Fig. 31a) at the edges of the overview images. The images were converted to binary, within which groups of neighbouring black pixels (constituting open cracks) are computed as particles. A basic area filter was applied removing particles below 20 μm^2 and the statistical "empirical rule" (also known as the 68-95-99.7 rule) was applied to the area distribution of the particles in the background squares. Following the three σ-space convention from the mean value (Fig. 31d), all the material with areas within 99.7% of the background distribution was considered noise and removed from the process zone region of interest.

4.4 Results

4.4.1 Mechanical data

We deformed 15 inclusion-bearing and 7 solid Carrara marble samples. The mechanical data from the experimental series are summarized in Table 7. Stress-strain curves were measured at various confining pressures and for different sample configurations (Figs. 32 and 33). The sample with extensional bridge (EB) configuration of the inclusions has been tested under different confining pressure conditions of 30, 50, 100 and 300 MPa (Fig. 32a-d) and is compared to pure Carrara marble cylinders.

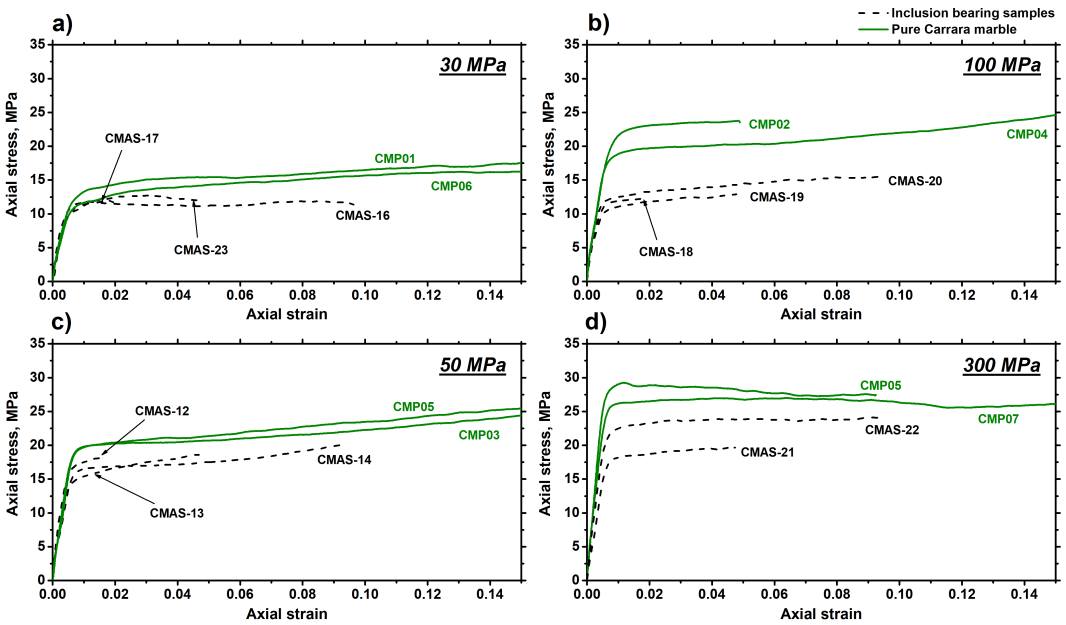

Figure 32: Mechanical data for some of the constant strain rate triaxial experiments presented in this study. Extensional bridge configuration and pure Carrara marble samples are compared at equivalent values of confining pressure, increasing from a) to d). Line styles distinguish inclusion-free from-inclusion bearing samples.

Yield stress of the inclusion-bearing samples increases with applied confining pressure

(Fig. 32). In all cases, the presence of inclusions with EB configuration appears to lower the yield strength of the specimens between ≈ 3-30% (300 MPa confining pressure) and up to ≈ 40% (50 MPa) compared to pure Carrara samples. The pressure-dependent strength at low confinement (< 100 MPa) suggests that dilatant cracking contributes to deformation. For inclusion-bearing samples this pressure-sensitivity probably persists at higher confining pressures than for pure Carrara marble because of the stress concentration at the tip of inclusions. With the exception of two intermediate confining pressure samples (50 and 100 MPa), all samples display weak hardening up to the maximum bulk axial strain.

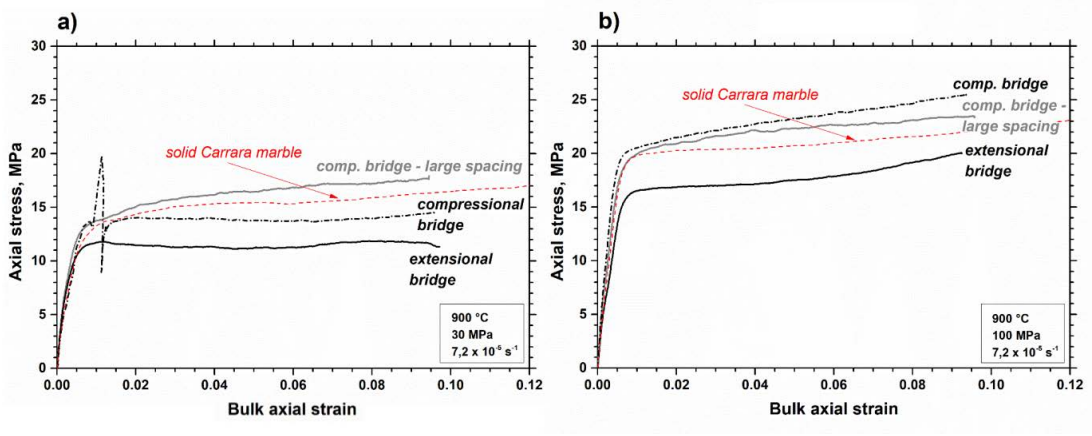

Figure 33: Comparison of the three different sample configurations at the representative confining pressures of 30 (a) and 100 (b) MPa. In these, a solid black line is indicative of the extensional bridge configuration, the stippled line of the compressional bridge one and the grey line stands for the compressional bridge – large spacing configuration. The red stippled line is representing the mechanical behaviour of solid cylinders of Carrara marble deformed at the same conditions.

The compressional bridge sample (CB, Fig. 29c-d) and compressional bridge – large spacing (CBLS, Fig. 29e-f) sample configurations were tested at similar temperature and strain rate as the EB and pure Carrara marble samples and at confining pressures of 30 and 100 MPa. All experiments were terminated at $\varepsilon_{\text{bulk}} \approx 0.10$. Strength of all samples increases with increasing pressure P_c (Fig. 33a and b). The extensional bridge samples are weakest (black solid line in Fig. 33a and b), and the different spacing between inclusions in the compressional bridge configurations does not affect significantly aggregate strength. It should be noted that the experiment performed at 30 MPa pressure using the CB assembly (CMAS-24) encountered a technical problem during loading. The CB configuration samples have similar peak strengths as the solid Carrara marble specimens (Fig. 33a and b). Instantaneous differential stress values at a bulk strain of ≈ 5-9% were measured in the high strain EB and in the solid Carrara samples; the stress differential between the two values (defined as: $\frac{(\sigma_{inst,CM}-\sigma_{inst,CM+SH})\times 100}{\sigma_{inst,CM}}$) is then plotted (in percentage) versus the applied confining pressure (Fig. 34). A trend is visible pointing in the direction of a decreased effect of the presence of weak inclusions on the aggregate strength of the samples with increasing confining pressure. Given the non-linearity of the trend, it is expected that a plateau would be reached at even higher confining pressures.

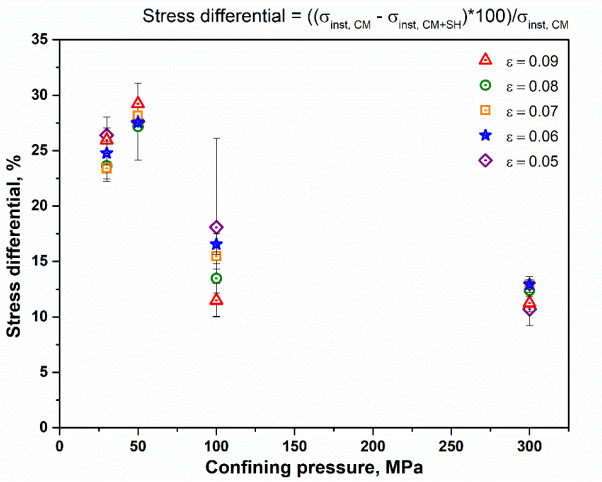

Figure 34: Plot of percentage stress differential between instantaneous axial stress (at different values of strain, from 5 to 9%) in the solid marble and in the extensional bridge inclusion-bearing samples, versus applied confining pressure.

4.4.2 Strain localization

The post-deformation angular deflection of the strain markers was investigated to compare the local evolution of shear strain at different experimental conditions. An appreciable deflection of the markers is only measured in the EB and the CB samples.

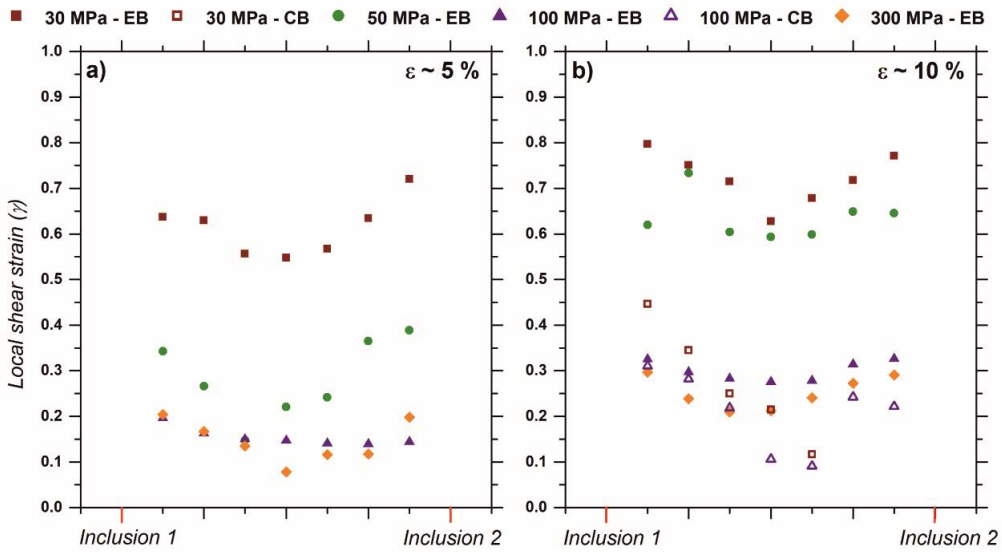

Figure 35: Local shear strain evolution with distance from the two inclusions within the process zones of extensional bridge (EB) and compressional bridge (CB) configuration samples. Spacing between the strain markers is approximately 1mm. Bulk axial strain in a) is ≈ 5% and in b) about 10%. Different colours correspond to the applied confining pressure (see legend at the top). Note that, due to a misalignment of the markers on the jacket with respect to the process zone of the sample, in one instance (30 MPa – compressional bridge) values are available for one side of the shear zone only. Considering the other samples plotted, we assume that the missing trend would be substantially symmetrical to the available values.

At large spacing of the inclusions (compressional bridge – large spacing) the markers maintain their pre-deformation orientation suggesting that strain remained largely homogeneous in the sample. Local shear strain estimates vary with distance from the two inclusions for different values of bulk axial strain (≈ 5% in Fig. 35a and ≈ 10% in Fig. 35b). The highest degree of strain localization is occurring at the lowest investigated confining pressure of 30 MPa for extensional bridge samples deformed to $\varepsilon \approx 0.05$ (Fig.

35a). The local shear strain concentration decreases with increasing confinement and the two highest confining pressures samples display only incipient localization. Note the symmetry of the measurements with respect to the center of the process zone, where the lowest shear strains are found. With increasing bulk axial strain (Fig. 35b), local shear strain within the process zone also increases, still showing the lowest values in the center of the shear zone. For equivalent values of bulk axial strain, local shear strains within the process zones of CB samples (open symbols in Fig. 35b) are considerably lower than those of EB samples, in particular at 30 MPa confinement. Additionally, the trend of decreasing shear strain from the contact with the inclusion towards the center of the process zone is more pronounced in the CB samples than in the EB ones, possibly indicating a narrower area of inclusion-induced weakening in the host Carrara marble matrix. These observations will be further addressed in the following sections.

4.4.3 Microstructural evolution

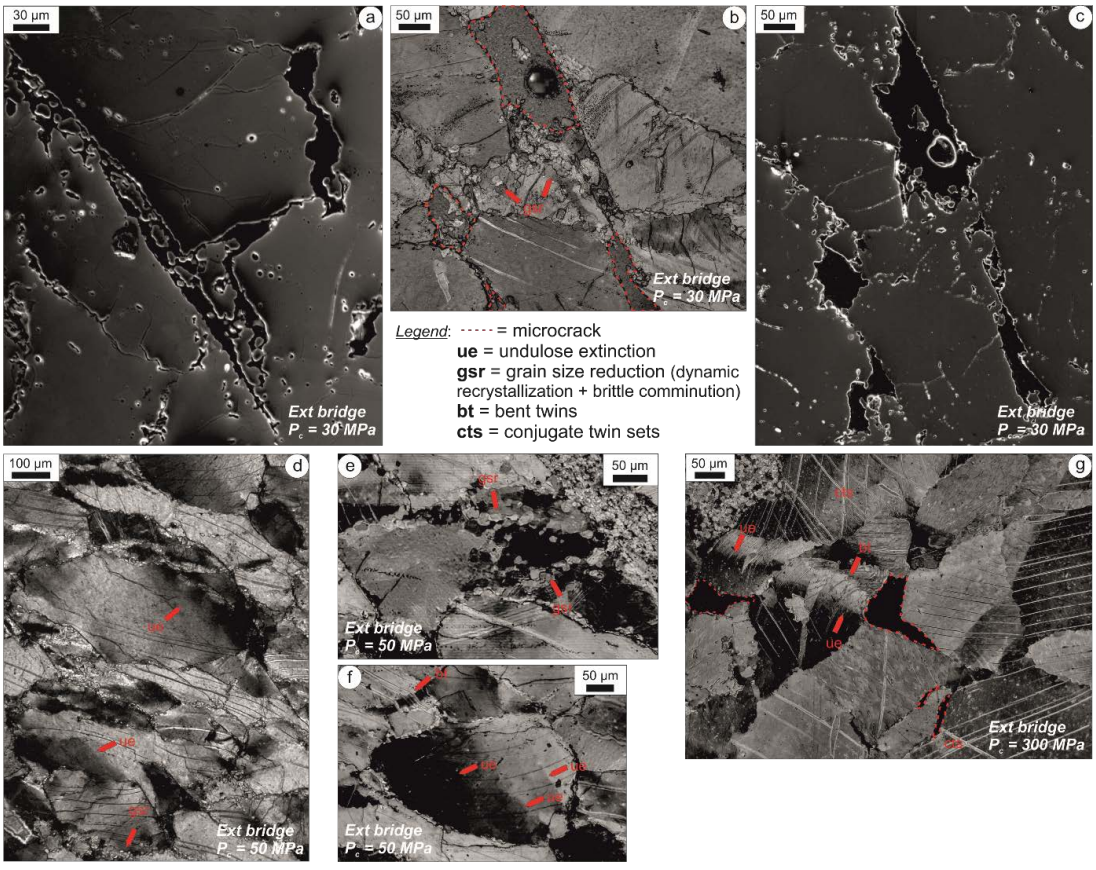

Figure 36: Details of high bulk strain ($\varepsilon \approx 0.1$) experimental microstructures. Applied confining pressure and sample configuration are specified on the images. A legend explains the abbreviations used to indicate most interesting features of the microstructures indicative either of brittle (microcracks) or ductile (e.g. undulose extinction, bent twins) deformation. Note that the major stress direction (σ_1) is vertical in all the images.

Optical analysis of the thin sections produced from the deformed samples reveals the occurrence of different degrees and spatial distribution of both brittle and ductile deformation mechanisms, depending on bulk axial strain, sample configuration and applied

confining pressure. The initially rectangular inclusions (see Fig. 29) are strongly deformed. Increasing deviation from the cylindrical shape of undeformed samples is visible as the applied total axial strain increases, in particular in the case of the EB configuration at low confinement. In comparison, the bulk sample deformation is more homogeneous for the CB configurations.

Crystal plastic deformation: The formation of a well-defined shear zone at the center of the specimens is observed only in medium to high bulk axial strain (≈ 5-10%), low confining pressure (30-50 MPa) EB configuration samples. Patches of undulose extinction, elongated grains and grain size reduction (Figs. 8b, d, e and f) are the most visible results of plastic strain localization. The initial grain size of the Carrara marble (≈ 150 μm, as reported in Rybacki et al., 2014; Nardini et al., 2018) is reduced to about 10-20 μm grainsize of recrystallized grains (Fig. 36e). Subgrain boundaries are visible and

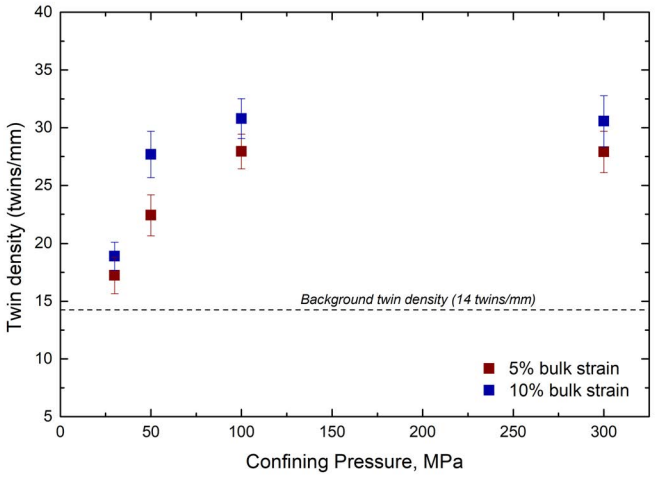

Figure 37: Twin densities (twins/mm) calculated within the process zone of EB configuration samples at different applied confining pressures and bulk strains ($\varepsilon \approx 0.05$ in red and $\varepsilon \approx 0.1$ in blue). The background twin density (14 twins/mm) is measured in a sample of undeformed Carrara marble.

match the size of the fully recrystallized grains. In some cases, (e.g. 50 MPa confining pressure, 10% axial strain EB sample) a weak foliation oriented at a low angle to the shearing direction is developed, but the majority of the samples do not display any shape preferred orientation of the grains. All samples deformed at confining pressures of 100 and 300 MPa and low confining pressure samples with CB configuration show only minor microstructural modification, often confined to the immediate surroundings of the inclusion tips. Deformation twinning is most prominent at high confinement in EB and CB samples (Fig. 36g). Twin lamellae are often bent (Fig. 36f and g) and display conjugate sets at roughly 60° from each other (Fig. 36g). Twin density was calculated within the process zone of the intermediate (5%) and high (10%) bulk strain EB samples. With an average of ≈ 30 to 40 measurements per sample, the resulting densities plotted against the applied confining pressure are shown in Figure 37. Note that the background twin density (quantified in a thin section of undeformed Carrara marble) is about 14 ± 1 twins/mm.

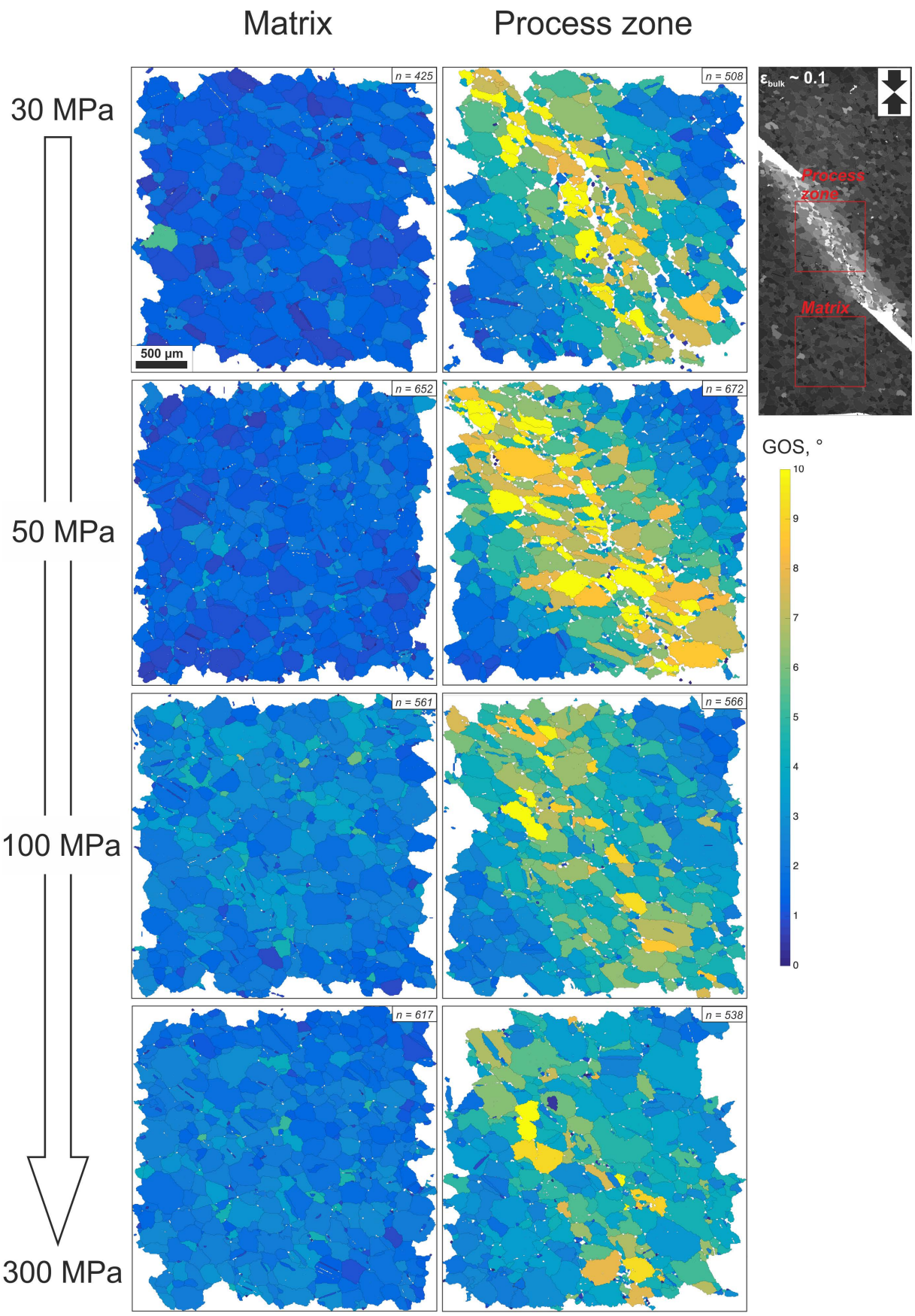

Figure 38: Grain maps displaying the GOS values distribution with increasing confining pressure (top to bottom) within equal area regions of interest in the matrix (left) and process zone (right) of extensional bridge samples deformed to 10% axial strain. In the top right corner of every map is the number of grains (n) computed per region of interest.

The contribution of deformation twinning to the total strain appears to be negligible at the lowest confining pressure investigated (30 MPa), but increases substantially at intermediate confining pressure of 50 MPa reaching a plateau at 100 MPa of roughly twice the background value (Fig. 37). Comparing twin densities for intermediate (5%) and high (10%) bulk strain samples suggests that twin nucleation may depend on strain (Rybacki et al., 2013). Overview EBSD maps were acquired over a selection of the experimental samples (Table 7). Grain orientation spread (GOS) is a common EBSD based method used to quantify the degree of intracrystalline lattice distortion within grains, relating internal lattice misorientation of grains to dislocation activity. A recent study (Cross et al., 2017) has developed GOS-based methods for paleopiezometric estimations, where newly recrystallized grains (low stored strain, low dislocation density) are distinguished from relict deformed grains by means of a GOS threshold.

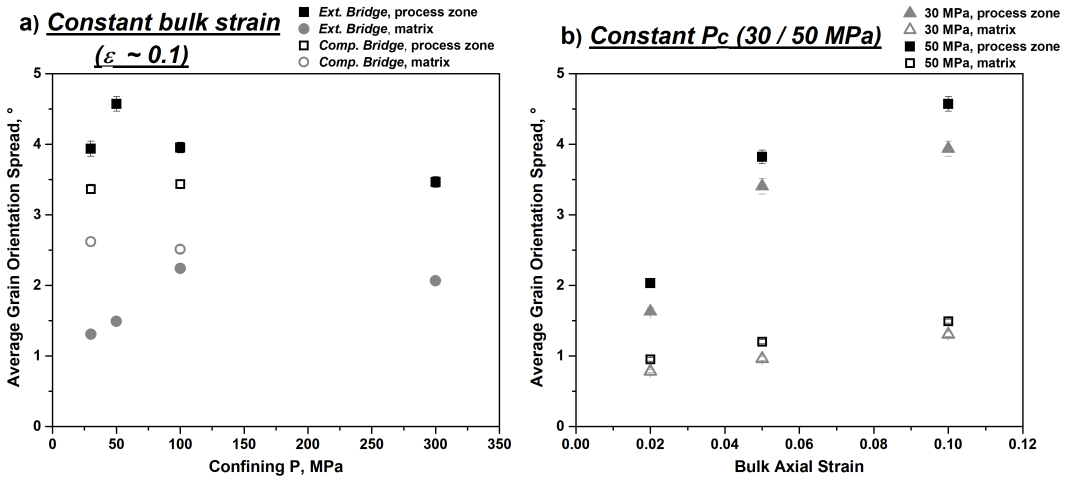

Figure 39: Average values for GOS (grain orientation spread) calculated in extensional bridge and compressional bridge configuration specimens over the process zone and the matrix of (a) the 4 high bulk strain samples confining pressure series and for extensional bridge samples of (b) the axial strain series at 30 and 50 MPa confining pressures. For details on the regions of interest selected for the analysis, see **textitsection 4.3.3**, where the computational parameters for the calculation of GOS are also given.

Two regions of interest were selected for every sample to carry out GOS calculations. Each covers a 3×3 mm square in the center of the process zone and an equal area region in the matrix away from the inclusions. These regions were treated separately, calculating the GOS for the computed grains and subsequently determining the mean value within the regions of interest. For the EB samples deformed to $\varepsilon \approx 0.10$, the resulting maps display opposing trends of GOS values with increasing confining pressure for matrix and process zone (Fig. 38, grains of low internal lattice distortion are shown in blue and highly deformed grains in yellow). With increasing confining pressure, GOS increases in the matrix but decreases in the process zone (Fig. 39a).

Increasing bulk strain (2, 5 and 10%) results in increasing average GOS for EB samples deformed at the two low confining pressures (30 and 50 MPa) (Fig. 39b). In the process zones where strain is localized, GOS increase is more pronounced with respect to the matrix. Irrespective of bulk strain, average GOS values are lower for samples deformed

at 30 MPa confining pressure compared to 50 MPa.

Brittle deformation features: In most samples, cracking is observed microscopically in the process zone. Intra- and inter-crystalline cracking of the Carrara marble occurs in all experimental configurations (Figs. 36, 40). In some cases, the fracturing is dis-

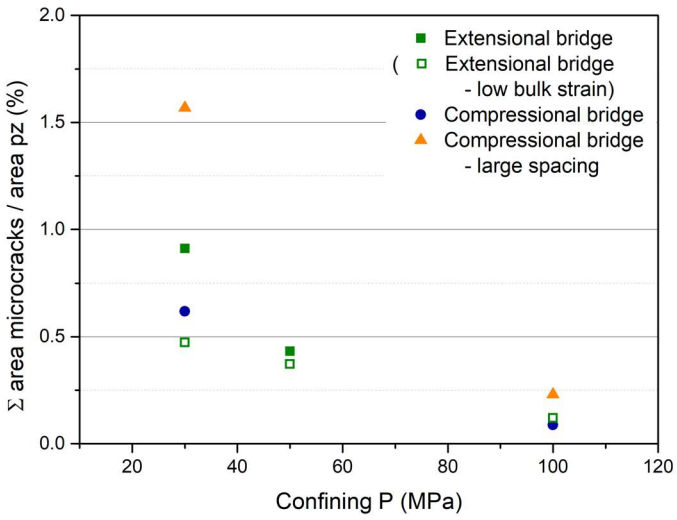

Figure 40: Porosity distribution in the process zone (pz) of samples at different applied confining pressure and for different sample configuration and total axial strain. Maximum porosity is achieved by the samples of the compressional bridge – large spacing configuration, regardless of the applied confining pressure. Solid symbols denote bulk axial strain of 10% and open symbols of 5%. The difference between configurations and between total axial strains is decreasing with increasing confining pressure.

tributed along the entire process zone between inclusions. Microcracks are surrounded by large calcite grains undergoing internal plastic deformation (Fig. 36g). Sutured grain boundaries are decorated by small recrystallized grains (Fig. 36b). The presence of recrystallized grains is typical of low confining pressure (30 and 50 MPa) and high bulk strain samples with extensional bridge configuration (Fig. 36b and e). For a detailed study of the microcracks, SEM overview images in BSE mode were collected for some of the experimental samples (Fig. 31). The total (crack) porosity, corrected for background porosity, decreases with increasing confining pressure (Fig. 40). The amount of deformation-induced porosity is lower at low axial bulk strain (2%) than at high strain (open vs solid squares in Fig. 40). At high axial strain (10%), the compressional bridge – large spacing configuration shows the highest amount of total porosity, followed by the EB and finally by the CB samples, regardless of confining pressure. At increasing confining pressure, differences in porosity between sample configurations or total axial strain decrease. At 100 MPa confining pressure total porosity is less than 0.25%.

For low confining pressure samples (30 and 50 MPa EB configuration and 30 MPa CB samples) the number of open cracks within the process zone is large enough to allow for a statistically significant analysis of their long axes' orientation with respect to the far-field stress directions. In Fig. 41, rose diagrams of the orientation of the long axes of cracks are

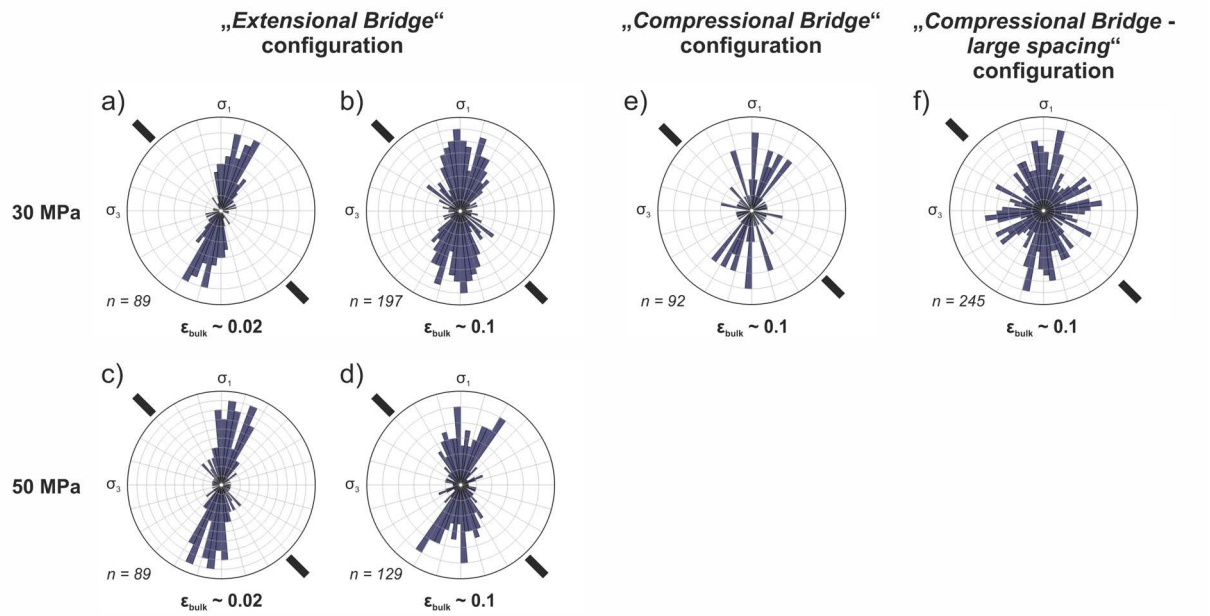

Figure 41: Rose diagrams displaying the preferential orientation of long axes of cracks (within the process zone of low confining pressure samples) with respect to the far-field stress directions and the shear plane determined by the arrangement of the limestone inclusions (solid bars). In a-d extensional bridge configuration samples at low strain (a, c) and high strain (b, d) are displayed; in e and f are the high strain compressional bridge and compressional bridge – large spacing configuration samples, respectively. The number of fractures included in the analysis (n) is indicated under the rose diagrams.

plotted for six selected samples, four from the extensional bridge configuration and two from the compressional bridge ones. Note that the long axis of a crack is assumed as the long axis of the best fit ellipse and is indicating the propagation direction perpendicular to opening. For the EB configuration microcracks are preferentially oriented parallel to the maximum principal stress direction σ_1, accompanied by a second maximum oriented at about 60-75° to the shear (inclusion) plane. These two maxima are enhanced at high strain of $\varepsilon_{bulk} = 0.1$. Fewer cracks are observed at 50 MPa confinement than at 30 MPa (Fig. 41 a-d). In comparison, CB samples display broader orientation distributions (Fig. 41e, f). The compressional bridge – large spacing sample (Fig. 41f) is characterized by the largest number of fractures (n = 245), which are distributed randomly with respect to the far-field stress and shearing direction along the inclusions plane.

Bivariate histograms were plotted where the region of interest was gridded and every square within the grid was color-coded according to the number of black pixels (in a binary image indicative of open space, hence fractures or pores) it contained (Fig. 42). The amount of cracking decreases with increasing confining pressure (c. ref. Fig. 40). At pressures > 100 MPa, cracking is largely suppressed regardless of inclusion configuration. At 30 MPa confining pressure microcracks increase with increasing bulk axial strain in EB samples as opposed to samples deformed at higher pressures (Fig. 42a). Most strikingly, the spatial distribution of microcracks within the process zone is strongly influenced by the positioning of the soft inclusions. In EB specimens cracks are arranged along the shear plane between the two inclusions (Fig. 42a). In contrast, CB samples display microcracks primarily around the inclusions and towards the external quadrants as opposed to the

internal region between the two inclusions (Fig. 42b, c).

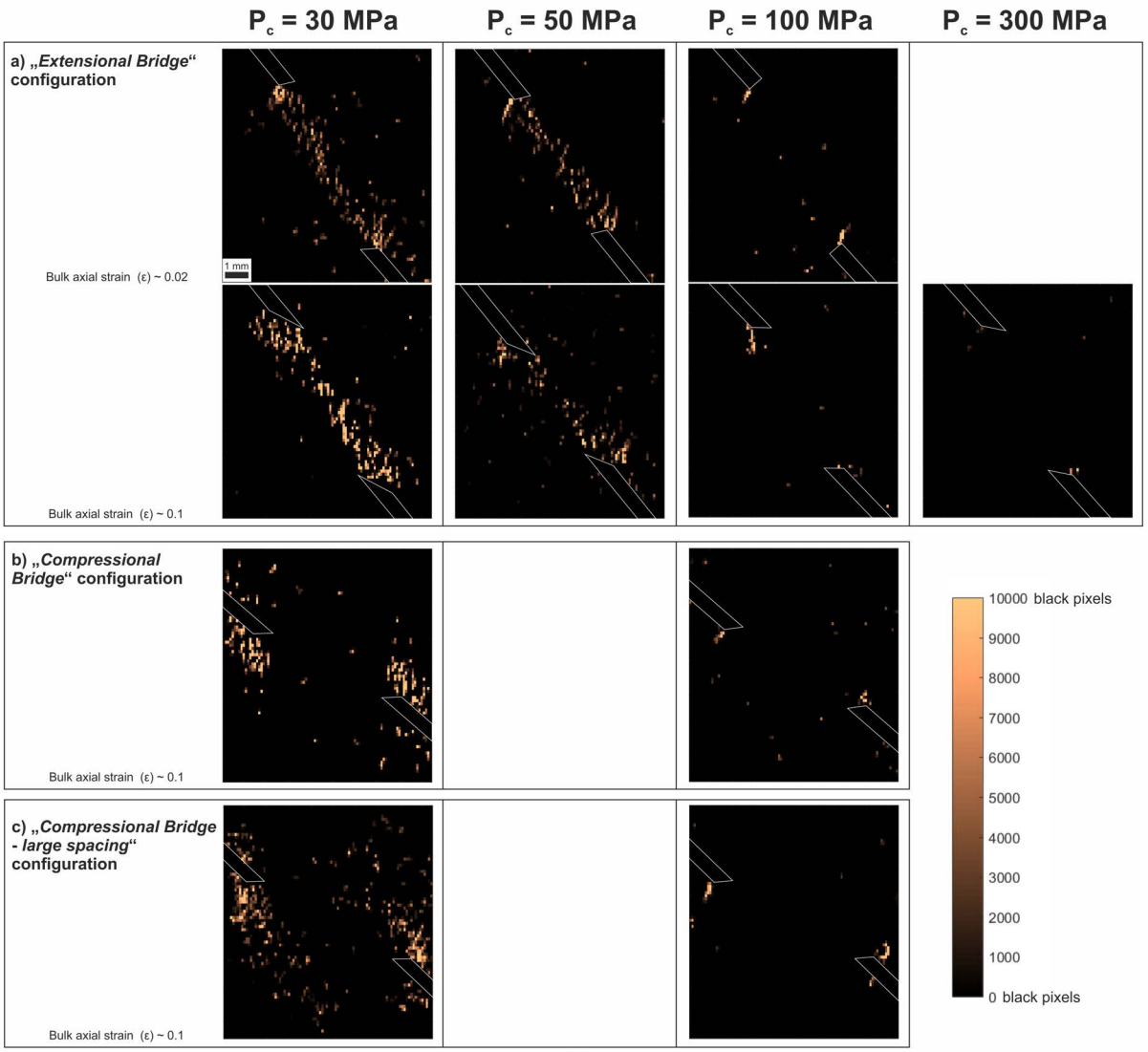

Figure 42: Bivariate histograms displaying the spatial distribution of cracks within the process zones of the samples considered. Applied confining pressure is increasing from left to right and for the extensional bridge configuration (a) end-member values of bulk axial strain are shown for comparison ($\varepsilon \approx 0.02$ and 0.1). The area of the process zone considered for the analysis (see Fig. 31a) is converted into a binary image where black pixels represent porosity and divided into an 85x85 squares grid, each of the squares being color-coded according to the number of black pixels it contains. It follows that high concentrations of pixels are indicative of coalescence of open fractures.

4.5 Discussion

4.5.1 The control of heterogeneities' distribution on strain localization

Nucleation of shear zones at local heterogeneities and defects is frequently observed in the field. In natural examples, as in intrusive granitoids crossed by systems of late magmatic fractures and veins (e.g., Segall & Simpson, 1986; Kronenberg et al., 1990; Mancktelow & Pennacchioni, 2005, 2013), deformation is often controlled by the geometry and arrangement of the precursor heterogeneities. For example, shear zones nucleate preferentially at the interfaces between the homogeneous host rock and pre-existing joints and fractures or within low-viscosity veins and dykes. As these geometric precursors are discrete elements

of finite length and width, the slip deficit arising as the displacement along the shear zone drops to zero at its termination is accommodated either by distributed foliation or by the opening of wing cracks, depending on the kinematics (extensional or contractional) of the quadrant involved (Pennacchioni & Mancktelow, 2018).

In our experimental setup, the limestone inclusions embedded in the Carrara matrix are strongly deformed after the tests (Fig. 29c, f, i). Their terminations, rectangularly shaped prior to deformation and with surfaces oriented at 45° to the direction of σ_1 (Fig. 29), appear to be passively rotated during the experiments almost to parallelism with the shearing direction in the highest bulk strain samples. A rough estimation of the local shear strain sustained by the inclusions yields values as high as $\gamma \approx 1$. The ensuing slip deficit at the inclusion terminations is accommodated within the host Carrara marble involving several deformation mechanisms (Pennacchioni & Mancktelow, 2018).

The normal stress distribution around a planar discontinuity subjected to simple shear displays an anti-symmetric configuration (tensile or compressional) with respect to the tip of the discontinuity (Segall & Pollard, 1980). In our experimental configuration with the presence of two pre-existing heterogeneities, the stress fields around their tips likely interact during deformation. Therefore, as the slip deficit builds up, the host marble in the region between the inclusions will be subjected to either extension or compression depending on the relative positioning of the inclusions and how the stress fields at their tips interact. In extension, abundant microcracking is observed at lower confining pressures (Fig. 42a) in accordance with the Goetze criterion (see ***section 4.5.3***). Conversely, when the region between the inclusions is in compression, tensile microcracking is found in external quadrants around the inclusion terminations (Fig. 42b and c). Similarly, the kinematic boundary conditions also affect the distribution and intensity of crystal-plastic processes and ultimately the degree of strain localization at the sample scale (Fig. 43). This is shown by means of grain orientation spread (GOS) maps based on overview EBSD data. In EB samples, the distribution of ductile deformation within the host marble is spatially highly heterogeneous (Fig. 43a), with a clear decrease in localization with increasing applied confining pressure (related, as will be discussed in detail in ***section 4.5.3***, to the role of brittle deformation; see also Figs. 40 and 42). In the CB configuration, on the other hand, strain localization is substantially suppressed and the slip deficit at the tip of the inclusion is accommodated by distributed ductile deformation over larger areas of the host marble (Fig. 43b and c).

In the fully brittle regime, a plethora of experimental studies have investigated the influence of the geometry of pre-existing flaws in a homogeneous medium on coalescence of cracks, potentially leading to localized failure. Although these studies were conducted at ambient conditions under uniaxial compression, some parallels exist with our results. Important differences are ultimately observed in the fracturing patterns between our experiments (where the active plastic processes may locally change the stress distribution) and the fully elastic investigations here discussed; nevertheless, interesting similarities are

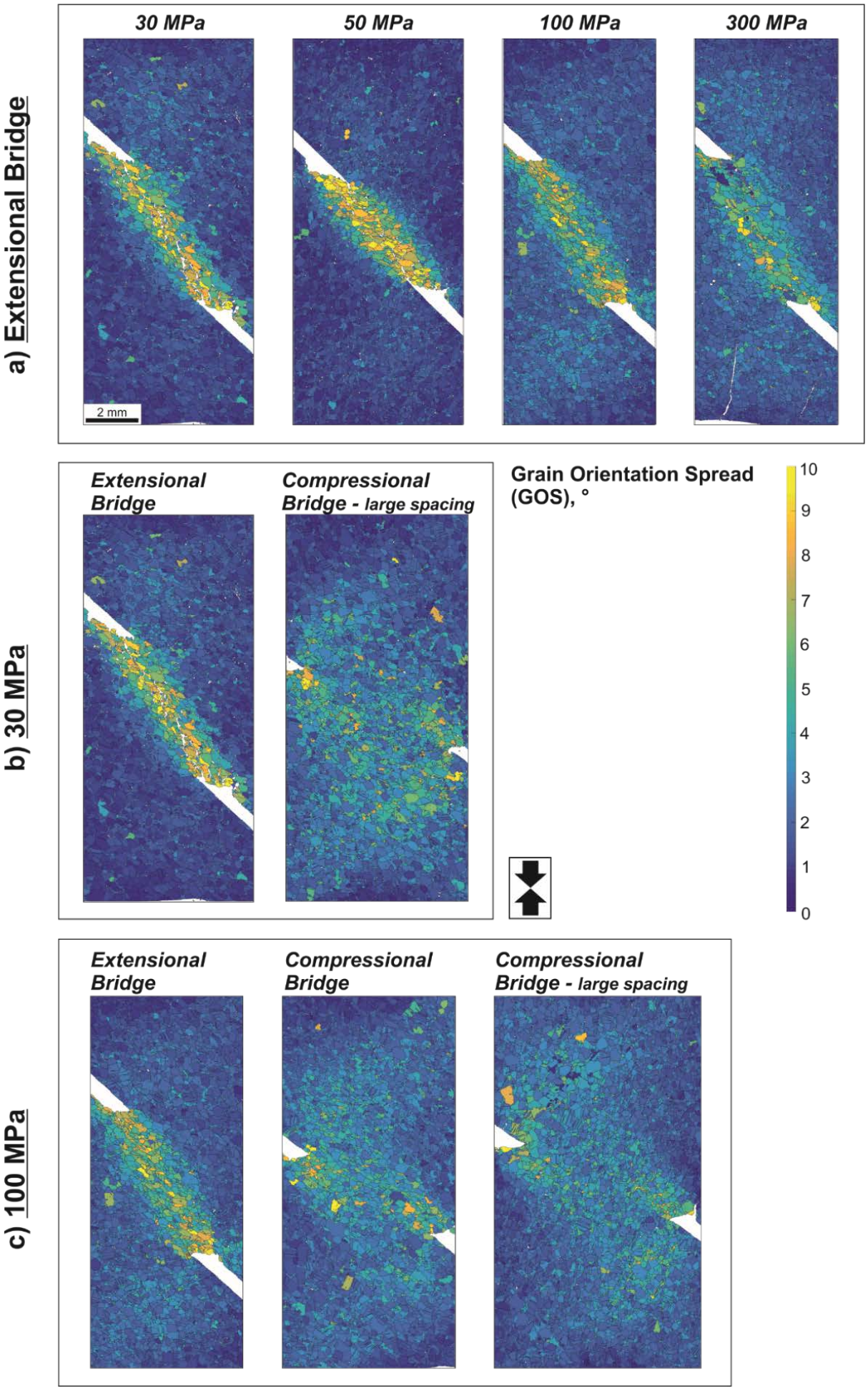
a) Extensional Bridge
30 MPa
50 MPa
100 MPa
300 MPa
2 mm
b) 30 MPa
Extensional Bridge
Compressional Bridge - large spacing
Grain Orientation Spread (GOS), °
10
9
8
7
6
5
4
3
2
1
0
c) 100 MPa
Extensional Bridge
Compressional Bridge
Compressional Bridge - large spacing

Figure 43: Overview GOS (grain orientation spread) maps based on EBSD data. In a) the maps for the largest bulk strain extensional bridge samples at increasing values of confining pressure (from left to right); in b) extensional bridge and compressional bridge – large spacing configurations at the same P_c of 30 MPa are shown (note that the thin section produced for the P_c = 30 MPa compressional bridge configuration sample was damaged during preparation for EBSD analysis, therefore no EBSD map was acquired for it), while in c) the three different configurations at P_c = 100 MPa are compared. All samples were deformed to ≈ 10% strain.

worth mentioning.

Most authors working on couples of pre-existing fractures within homogeneous host materials tested the equivalent of our extensional bridge configuration. The main factors controlling the type and timing of fracturing and, ultimately, the coalescence pattern of cracks were identified in the variation of three key parameters: initial angle of the flaw with respect to σ_1, length and angle of the bridging area (e.g., Reyes et al., 1991; Shen et al., 1995; Bobet & Einstein, 1998a, 1998b; R. H. Wong & Chau, 1998; Ko et al., 2006; Morgan et al., 2013). L. Wong and Einstein (2009) also investigated geometries similar to our compressional bridge configuration in their study on molded gypsum and Carrara marble prisms containing two parallel pre-existing open flaws under uniaxial loading. Different coalescence patterns were identified (Fig.13 in L. Wong & Einstein, 2009), the first two of which are characteristic of the compressional bridge equivalent geometry. Interestingly, these are the only ones that lead to either no crack coalescence or indirect coalescence occurring outside of the central bridging region. Similarly, no cracking and subsequently no ductile localization is occurring within the "process zone" of our compressional bridge samples (Fig. 42b, c). Contrary to these results, Morgan et al. (2013) observed indirect coalescence in some extensional geometries as well, but they attribute them to material effects (larger and stronger grains in the granite here employed compared to the Carrara marble used by L. Wong & Einstein, 2009).

We measured preferential orientation of cracks' long axes (Fig. 41), indicative of the interaction between far field and local stresses during brittle (or semi-brittle) failure. This behaviour is also well documented in experimental studies conducted in the fully brittle field. Wang et al. (1987) describe tensile primary and secondary cracks opening at the tip of pre-existing flaws in uniaxially compressed Fangshan marble rotating into parallelism with the compressive (σ_1) direction during propagation. Bobet and Einstein (1998a) observed occurrence of two types of cracks in uniaxial and biaxial experiments on gypsum blocks with couples of pre-existing flaws: tensile primary (wing) cracks, propagating in a curvilinear fashion away from the inclusion, and secondary (shear) cracks developing in plane with the flaws, which are typically responsible for macroscopic sample failure. The combination of these two crack types, and their propagation directions show similarities with cracks found in our 30 MPa confinement extensional bridge samples (Fig. 41a and b). At low bulk strain, cracks are mostly oriented at about 75° to the inclusions, developing at higher strain a new maximum aligned with the direction of maximum stress σ_1. With higher bulk strain (Fig. 41b), some cracks are found along the shear direction, equivalent to what Bobet and Einstein (1998a) describe for secondary shear

cracks. As the confinement is increased for the EB samples, the preferential orientation of cracks seems to point to the occurrence of primary/wing cracks type geometries, with two maxima parallel to σ_1 and nearly perpendicular to the inclusions, while no evidence for shear cracking parallel to the inclusions' plane is observed (Fig. 41c and d). It should be noted, however, that pure shear cracking might not be easily imaged in our BSE overviews if no appreciable tensile component is present and, particularly, if mechanical grinding produces fine grained material decorating the surfaces of cracks. Compared to the EB samples, the CB samples show no preferred crack orientations (Fig. 41e, f). This was also found by Jiefan et al. (1990), who performed uniaxial compression experiments on Fangshan marble plates containing single open flaws. The authors identified four different modes of rupture at the tip of the flaw, each characterized by a certain orientation with respect to the compressive stress direction. Bobet and Einstein (1998a) pointed out how the ratio between the inclusion length and the relative spacing between two inclusions affects the initiation stresses of wing cracks at the tips of the inclusions in the sense that, above a certain ratio, the inclusions (flaws) behave as if being isolated. This could easily be the case in our compressional bridge – large spacing samples.

While the analysis of the preferential orientation of microcracks is significant to unfold the orientation and magnitude of the stress field, caution should be used in our case. Firstly, the resolution of our technique does not allow for pure shear cracks to be included in the analysis. Moreover, the biggest criticality in the case of high temperature microcracking of Carrara marble lies in the large initial grain size of the material: we in fact observe how the orientation of grain boundaries is often the controlling factor for the development of microcracks. Finally, especially at large bulk strains, the complex interaction and interconnection of microcracks from areas of the process zone subjected to different local stresses is likely to smear and mask specific preferential orientations.

4.5.2 Numerical modeling

For a single planar inclusion of Solnhofen limestone located in Carrara marble subjected to simple shear at high temperature (T = 900 °C) and confining pressure (P = 300 MPa), enhanced stresses develop in front of the inclusion already at low values of bulk strain. This is due to the viscosity contrast between the matrix and the inclusion, being Carrara marble about 10 to 20 times stronger than Solnhofen limestone at our experimental conditions (Rybacki et al., 2014). The extent and propagation of the associated process zone ahead of the inclusions, where ductile deformation is enhanced, was modelled successfully for torsion tests (Döhmann et al., 2019). Their numerical modeling shows that localization mainly depends on the weakening behaviour of the matrix material and on finite strain. In the current study, localization is also linked to the development of microcracks, initiating around the tips of the weak inclusions but depending on confining pressure. Modeling of this complex interaction of brittle and crystal-plastic processes inducing nucleation and

propagation of localized deformation is beyond the scope of this paper. However, the elastic stress distribution of interacting cracks formed initially at the inclusion tips allows first order insight into the development of deformation in our experimental setups.

We therefore aimed at reproducing the elastic component of deformation occurring during our low confinement (30 MPa) experiments employing a 2D simplified geometry of the sample material, in which the Solnhofen limestone inclusions are substituted by pre-existing fractures and the surface being modelled is the same as the plane of the post-deformation thin sections. For this purpose, the simulation software roxolTM was employed to test a series of numerical models mimicking the experimental configurations used in this study. RoxolTM is designed to simulate fracture nucleation and growth and related fracture network evolution in rock and rock mass. The development is based on fracture mechanics principles and employs the mathematical framework of the extended finite element method (XFEM). The code is able to simulate linear elastic or poroelastic materials with existing faults or fracture networks that may propagate and coalesce during alteration of boundary conditions, e.g. due to excavation, well sinking, hydraulic fracturing, or similar (Backers et al., 2015; Meier et al., 2018). A Mohr-Coulomb type failure criterion is considered here for the initiation and propagation of fractures, and the models are stopped after the two subsequent initiation and propagation steps. Mechanical parameters and the applied stress field as derived from the experimental runs are listed in Table 8. A parameter study was conducted to investigate the effect of varying angle of internal friction, given that the extrapolation from the experimental data yielded an extremely low value. No substantial dependency on the angle of internal friction was detected either for the distribution of microcracks or the magnitude of the interacting stress fields.

Configuration	$\sigma_2 = \sigma_3$ [MPa]	σ_1	Cohesion [MPa]	Angle of internal friction
Extensional	30	42.3	3.9	0.57°
Compressional	30	45	3.9	0.57°

Table 8: Experimentally derived parameters employed for the simulation tests run with the roxolTM software.

Results from the simulations run using the sample geometry (EB and CB) do not agree well with our experimental observations. Distribution of mean stresses reveal strong gradients at the tips of the initial fractures and between them, but local stresses do not interact with each other and the resulting pattern of propagating microcracks does not reflect the different spatial arrangement of the initial fractures. A reason for this is likely the use of a purely elastic deformation simulation approach, that only accounts for very low amounts of bulk axial strain and only involves crack formation and coalescence, so that high strain plastic deformation is not considered. However, strain-related extension of the process zone in front of each inclusion (Nardini et al., 2018; Döhmann et al., 2019), causes stress perturbations ahead of the two inclusions to interact in the experiments.

To account for the above effect, we investigated interacting elastic stress fields gen-

erated by pre-existing discontinuities by reducing horizontal spacing between initial fractures and increasing their vertical distance so that they quasi-overlap (Fig. 44). The parameters employed in these simulations were the same as the ones used for the previous configuration (Table 8). Models reveal a strong interaction between the stress fields around the pre-existing fractures (Fig. 44). In the EB configuration (Fig. 44a) mean stresses in the step-over region are up to 70% smaller than the background value, while in the compressional configuration (Fig. 44b) mean stresses are on average 40% higher than background. As a result, the distribution of microcracks follows the areas of lowest mean stress in good qualitative agreement with our experimental observations (compare inset in Fig. 44a and b with Figure 42).

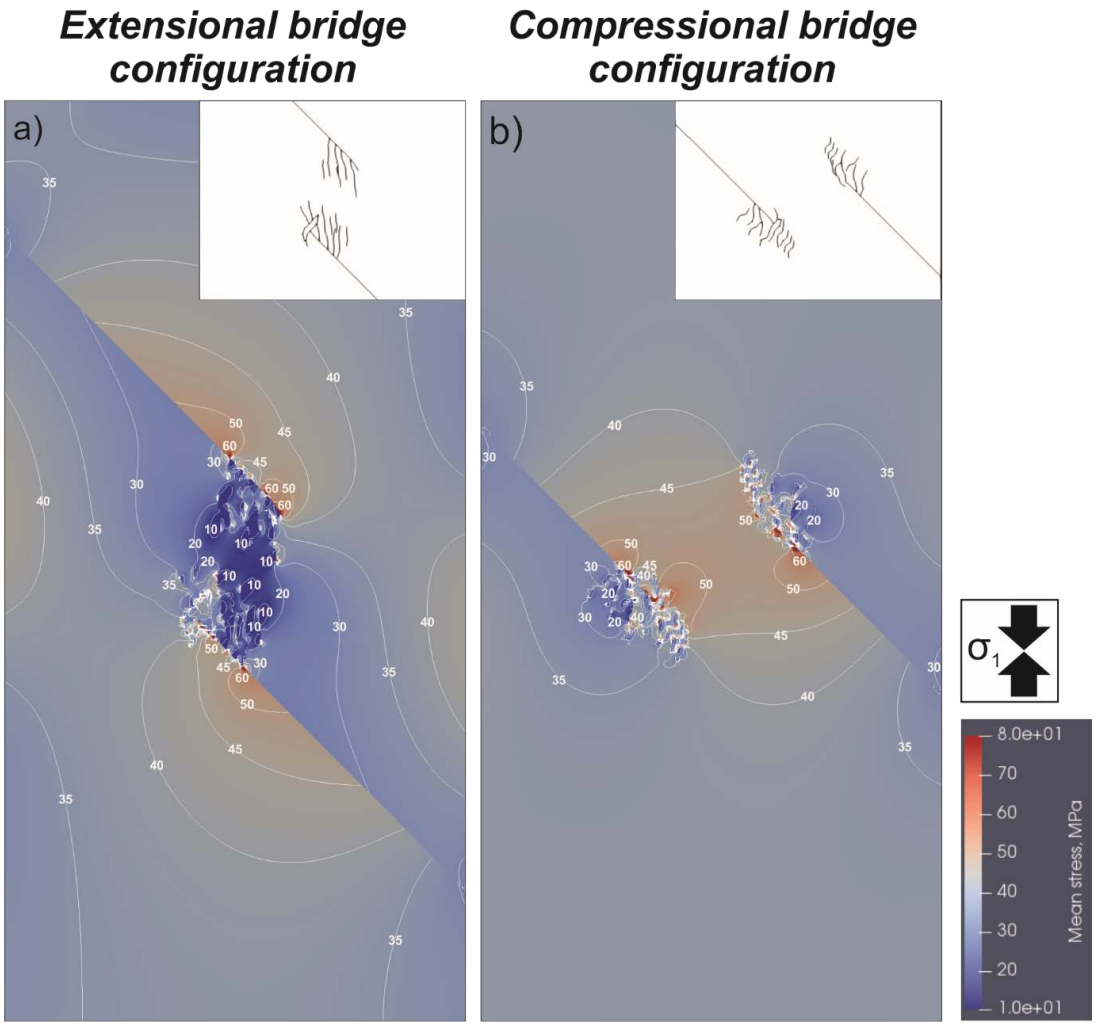

Figure 44: Results of mean stress distribution and fracture propagation (small insets) as resulting from simulations in roxolTM. The vertical and the horizontal spacing are both reduced with respect to the experimental samples to induce earlier interaction between the stress fields of the pre-existing fractures.

A modeling study of en-echelon fault arrays was conducted by Segall and Pollard (1980). Their analysis is focused on the distribution of elastic stresses during brittle deformation, but the results presented bear important resemblance to our case. In the geometry they employ (a right lateral fault array) "right stepping" is the equivalent of our extensional bridge, while "left stepping" corresponds to the compressional bridge config-

uration of our experimental samples. Given a specific spacing between the discrete fault arrays, a marked increase in mean stress is determined in the region between the cracks in the left stepping geometry, which is up to 1.4 times the background values. Conversely a distinct decrease of 0.6 times the background is noted in the right stepping configuration (see Figure 9 in Segall & Pollard, 1980). Most interestingly, their study predicts the spatial distribution of secondary fractures with respect to the two configurations also presented in our work. Tensile cracks distribution (Figure 9a-b in Segall & Pollard, 1980) mimics almost exactly what we observed in our experiments (Figure 42).

4.5.3 The brittle-to-ductile transition and the controlling deformation mechanism

For pure Carrara marble, a transition from brittle to crystal-plastic deformation at room temperature has been found experimentally by increasing confining pressure (Fredrich et al., 1989). The authors observed a transition from brittle to semibrittle to fully plastic deformation at constant strain rate deformation as a function of applied confining pressure ranging from 5 to 450 MPa. Calculations of the energy balance between brittle and plastic deformation mechanisms showed, in the semibrittle field, a decrease in the contribution of microcracking with increasing confining pressure until the r- slip system is activated in calcite. To satisfy the Von Mises criterion for plastic flow in polycrystalline calcite, the activation of both e^- twinning and r^- slip is required (Paterson, 1969). The transition between regimes is marked by a large variation in the strain partitioning between deformation mechanisms, which occurred in experiments of Fredrich et al. (1989) over a narrow range of pressures.

In our experiments performed at high temperature, plastic processes are expected to dominate the deformation behaviour. However, lowering of the applied confining pressure induces brittle behaviour in the host Carrara marble at inclusion tips where stresses are enhanced locally. Brittle cracks are ubiquitous in samples deformed at low confining pressures (e.g. Figs. 36, 40 and 42), regardless of the positioning of the inclusions. The large viscosity contrast between the inclusions and the host rock produces a strong stress concentration at the inclusion tips (Rybacki et al., 2014; Nardini et al., 2018; Döhmann et al., 2019), where differential stresses exceed the applied confining pressure. This allows microcracking to occur, in agreement with the empirical Goetze criterion stating that microcracking will be suppressed once confining pressure exceeds differential stress (Evans & Kohlstedt, 1995; Kohlstedt et al., 1995). In Fig. 45, peak differential stress for the high bulk strain experimental samples of all three configurations is plotted against the applied confining pressure. Local stresses at the tip of the Solnhofen inclusion are estimated to be a factor of 3 ($\pm$ 1) higher than the bulk background stress, based on piezometric calculations (Nardini et al., 2018). Local stresses at the inclusions' tips plot above or at the Goetze criterion line ($\sigma_1 - \sigma_3 = P_c$) for samples deformed at confining pressures of 30

and 50 MPa, in accordance with the dense microcracking observed in the low confinement samples (Figs. 36, 40, 41 and 42). At P_c = 100 MPa and above, on the other hand, cracking is largely suppressed (e.g. Figs. 40 and 42), also in accordance with the Goetze criterion (Fig. 45).

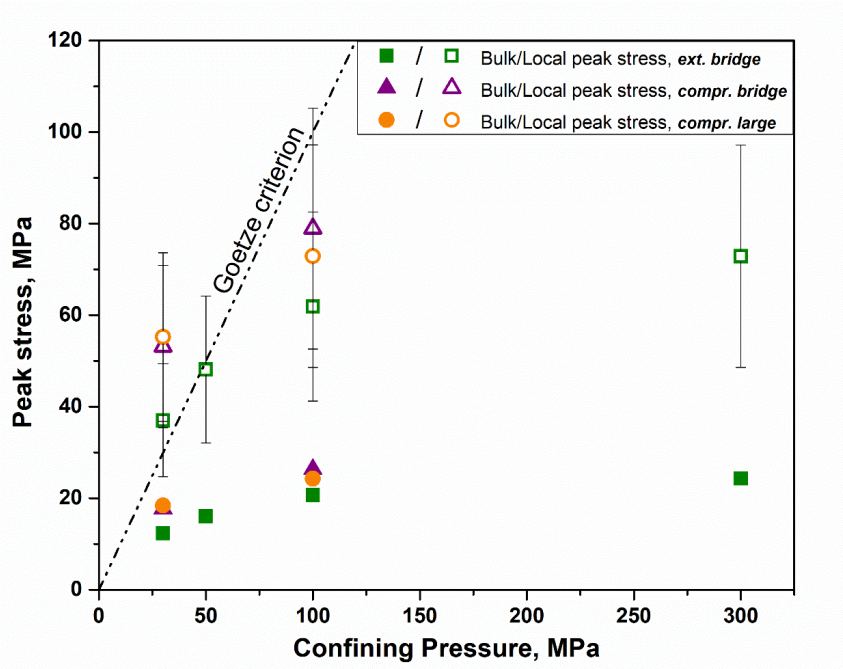

Figure 45: Peak (differential) stress versus confining pressure from the high bulk strain experiments of all inclusions' configurations. Bold symbols correspond to the bulk peak stress, while open ones are for the estimated stress concentration in the areas around the inclusions' tips (factor 3±1, following Nardini et al., 2018). The line corresponding to the Goetze criterion is also shown on the graph.

In addition to microcracking, evidence for dislocation activity is observed, like undulose extinction (e.g. Fig. 36d and f), subgrain boundaries and bending of twin lamellae (e.g. Fig. 36f and g). The presence of reduced grain size of the matrix material results from dynamic recrystallization producing core-and-mantle structures (Fig. 36e). In parts, grain size reduction may also result from brittle comminution (Fig. 36a, b and c), as in the process zone of EB specimens deformed at low confining pressures.

A semi-quantitative estimation of the partitioning of strain between microcracking and crystal-plastic deformation mechanisms active in the process zone and in the matrix of high strain ($\varepsilon \approx 0.1$) EB samples at different confining pressures reveals different deformation mechanisms including twinning (twin density, Fig. 37), dislocation activity reflected by internal lattice distortion (average GOS, Fig. 39), and microcracking (total area of microcracks over area of the process zone, Fig. 40).

The evolution of strain partitioning and localization is represented by the ratio between the average shear strain (γ) accrued in the process zone (Fig. 35b) and bulk axial strain of the sample ($\varepsilon_{bulk} \approx 0.1$). A more rigorous formulation of this quantity would require the estimation of the average shear strain within the matrix, which is expected to be varying with confining pressure (e.g. Fig. 38) while the bulk axial strain is constant in these samples; the technique employed here for measuring the local shear strain evolution

(Fig. 30), however, does not currently allow for the acquisition of such data. The increase in localization is accompanied by a steady increase in the amount of brittle deformation in the process zone (green curve, Fig. 46). Deformation of the matrix by crystal-plastic processes (dislocation creep and/or deformation twinning) is reduced due to progressive localization of strain within the process zone. Inside the process zone, average GOS reveals increasing dislocation activity with increasing localization until a threshold, represented by a confining pressure of 50 MPa at our thermodynamic boundary conditions, after which average GOS decreases again. In this interval (between 30 and 50 MPa, or 6.3 and 7.2 localization factor) the controlling deformation mechanisms is clearly the formation of microcracks, given the drastic increase in total area of secondary porosity (green curve in Fig. 46). Deformation twinning in calcite is a common feature characterized by very low critical resolved shear stress, activated already at low temperatures (e.g., Barber & Wenk, 1979; Burkhard, 1993). As only one independent slip system is available for e-twinning, the amount of strain that can be accommodated is relatively low, and strain incompatibilities at the grain scale arise (Burkhard, 1993). In our samples deformed at low pressures, strain incompatibilities are relaxed by dislocation activity, grain size refinement, and tensile cracking (Fig. 36a, b and c). As confining pressure is increased beyond 50

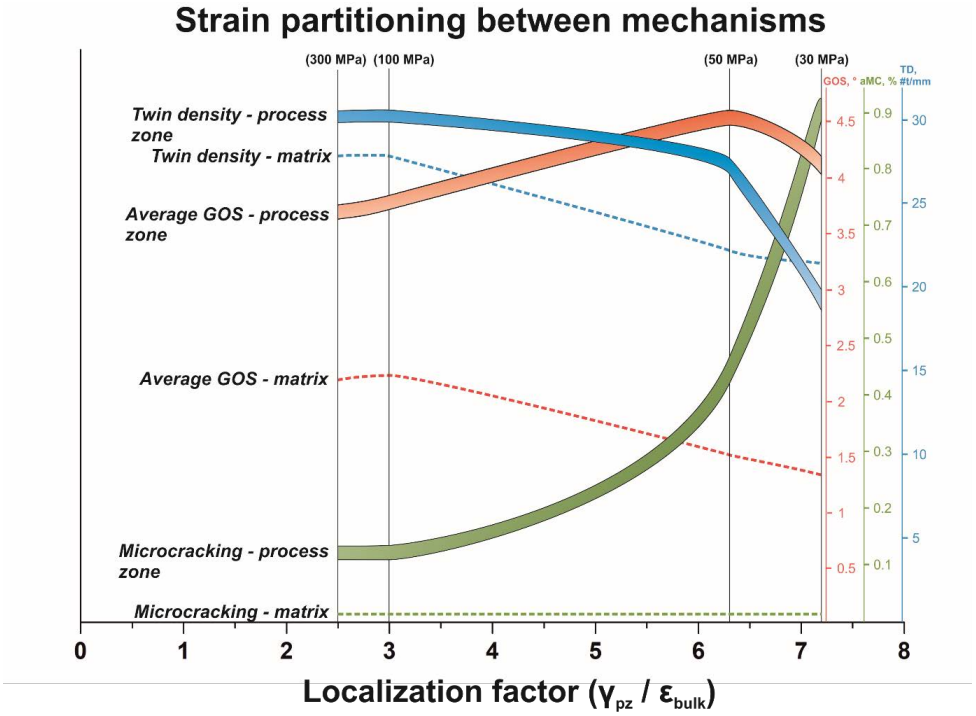

Figure 46: Semi-quantitative deformation mechanisms map for matrix and process zone as a function of localization factor, defined as the ratio between the average measured shear strain in the process zone (γ) and the bulk axial strain for the whole sample (ε_{bulk}). Data from the extensional bridge configuration high strain experimental series (from 30 to 300 MPa confinement) are employed. The six curves represent the evolution of partitioning between the three quantifiable deformation mechanisms (dislocation activity, expressed by the average GOS; deformation twinning, shown by twin density and microcracking) in the process zone (thick curves) and in the matrix (stippled lines). aMC = area microcracking, measured in percentage with respect to the total area of the process zone; TD = twin density, expressed as number of twins per mm; GOS = average grain orientation spread, measured in °.

MPa, however, cracking is suppressed and de-localization occurs, with mainly e-twinning accommodating strain within the process zone (Fig. 46). Variations in bulk axial strain

also affect strain partitioning between brittle and plastic mechanisms. Microcracking is pervasive in EB low confining pressure samples already at low values of bulk strain (2%). With increasing strain, the interplay between different deformation mechanisms (Figs. 39b, 41 and 42) becomes more dependent on the confinement applied: cracking and void formation increase substantially with increasing bulk strain at the lowest pressures investigated (Fig. 40), but are already significantly reduced at Pc = 50 MPa, where measured GOS values in the process zone are in turn consistently higher (Fig. 39b).

Interaction of brittle and plastic processes was also observed in nature. For example, in their study on the Cap De Creus shear zone, Fusseis et al. (2006) and Fusseis and Handy (2008) describe the local partitioning of strain between brittle and plastic processes during the formation of a crustal scale shear zone. Microfracturing appears to be occurring coevally with plastic deformation of the rock body as episodic propagation of pre-existing heterogeneities due to inefficient energy dissipation by dislocation creep and consequent concentration of stresses at flaw tips.

4.5.4 Geological implications

The occurrence of brittle precursors and material heterogeneities of various origin arranged in step-over geometries is very common in nature and is invariantly associated with the formation of small-scale high temperature shear zones. Moreover, the interplay between brittle and plastic deformation and its role in the nucleation and evolution of strain localization is a topic of interest in the study of large-scale shear zones at depth below the seismogenic zone of plate boundaries.

Field examples of localized ductile shear zones nucleating on brittle precursors are abundant in the case of granitoids undergoing complex tectonometamorphic paths prior to surface exposure (e.g., Segall & Simpson, 1986; Kronenberg et al., 1990; Guermani & Pennacchioni, 1998; Mancktelow & Pennacchioni, 2005; Pennacchioni & Mancktelow, 2007). In these examples, the presence of sets of cooling joints and pre-existing fractures often mineralized with hydrous phases is shown to facilitate localized high temperature plastic flow and assist with the formation of predominantly ductile shear zones at middle to lower crustal levels. Our experiments represent the laboratory analogue of strain transfer between lateral stepping of material heterogeneities (the en-echelon arrangement), where far-field stress orientation and the geometry of the step-over determines the kinematic of the ductile or brittle-to-ductile flow. Examples of both configurations presented in our study (compressional and extensional bridge) are documented in natural shear zones. Within the pre-Alpine granitoids exposed in north Eastern Italy in the Tauern tectonic window (Mancktelow & Pennacchioni, 2005), sets of thin cooling joints are organized in left-stepping en-echelon geometries which, combined with the imposed dextral sense of shear, produce contractional kinematic conditions in the area between the joints and the formation of shear band-like structures. Segall and Pollard (1983) report, in granodiorites

of the Sierra Nevada, the occurrence of secondary (dilatant) fractures in the en-echelon steps between left-stepping joint sets where the dominating sense of shear is sinistral and the resulting conditions between the joints are therefore extensional. Christiansen and Pollard (1997) present the case of end-to-end linkage of aplite dykes segments also within the granodiorites of the Sierra Nevada. The dykes are thin with respect to their length and extremely fine grained, therefore expected to be substantially weaker than the host rock. Their nature and the relative compression of the stepping area is similar to one of our experimental configurations. Shear strain transfer from the Solnhofen limestone inclusion to the host-rock marble in the step-over region is occurring in our experimental samples in a similar fashion to what described in the field studies mentioned above. The distribution of strain and its partitioning between brittle and ductile processes is a function of the step-over kinematics both in the experiments and in the natural examples.

Previous studies suggest an important role of pre-existing material heterogeneities in distribution of strain. However, the influence of the geometric arrangement of heterogeneities on the resulting kinematics of the deformation is often lacking in the analysis of natural cases. Our results suggest that strain localization is favoured by the interaction of brittle and ductile processes even in the absence of fluid infiltration and/or metamorphic reactions. However, the spatial arrangement of multiple heterogeneities can either promote or hinder localization in the ductile regime, even if brittle precursors exist.

Considering shallow crustal scale fault zones, Segall and Pollard (1980) discussed the kinematic relationship between the far field stress acting on the fault and the stepping direction of discrete fault segments, which can have a distinct effect on the seismicity (or lack thereof) of the stepping segments. Whether the arrangement of the fault segments promotes compressional or extensional conditions via the elastic interaction of the stress fields can determine the tendency of the stepping region to either be the site for diffuse small magnitude seismicity and aftershock activity, or to store larger elastic strains and ultimately fail catastrophically generating major seismic events.

Similarly, when moving to larger depths down to the brittle-to-ductile transition zone, comparable considerations can be made regarding the distribution of strain, the potential for brittle-assisted ductile localization and ultimately the style of deformation in step-over areas between material heterogeneities based on the results from the current study.

4.6 Conclusions

We conducted high temperature (900 °C) triaxial experiments on Carrara marble cylinders containing Solnhofen limestone inclusions arranged in different configurations, reproducing field examples of homogeneous rock bodies with pre-existing material heterogeneities arranged in compressional or extensional step-overs. The EB assembly was tested at varying conditions of total strain (2, 5 and 10%) and confining pressure (30, 50, 100 and 300 MPa), to investigate the effects of intervening brittle deformation on the nucleation

and development of localized strain. Confining pressures of 30 and 100 MPa have been employed to test two more configurations for the inclusions' step-over: one forming a simple CB and another one equally inducing compression but with a larger spacing between the inclusions. We observed abundant brittle deformation occurring in the samples at the lower confining pressures investigated (30 and 50 MPa) in all sample configurations with a substantial suppression of brittle deformation as the confining pressure increases. The spatial distribution of syn-deformational fractures is, however, a function of the inclusions configuration employed. In EB samples cracking is localized within the process zone between the inclusions, while in both the CB geometries the fractures distribute broadly around the tips towards the surrounding matrix and virtually no cracking occurs within the bridging region. Coevally active ductile deformation appears to follow such predefined path and distribute either heterogeneously, preferentially within the process zone (EB) or more homogeneously across the entire matrix (CB configuration). Ductile localization is therefore favoured by precursor and coeval brittle deformation only if this latter is in itself intrinsically heterogeneous. As brittle deformation gets suppressed with confining pressure, an EB configuration is still facilitating localization with respect to a compressional one, but less efficiently so than if assisted by brittle processes.

Acknowledgements

We are very grateful to Michael Naumann for his invaluable help with the designing of sample configurations and of passive strain markers. Stephan Gehrmann, Ilona Schäpan and Sathish Mayanna are also thanked for the preparation of samples and thin sections and the acquisition of SEM overviews, respectively. This project was funded via the DFG grant GR 4468/2.

5 General Conclusions

The current study presents the results of experimental work and numerical modelling, that were performed in an effort to better understand the nucleation and early development stages of high temperature shear zones formation. The study of localized deformation has been a main focus of the structural geology community ever since areas of higher-than-background strain have been recognized in the field as early as in the 19th century (Geikie, 1884). Ductile localization of strain is now established as a ubiquitous feature in exposed rocks of middle and lower crustal origin, as well as having been proposed for lithospheric mantle levels (e.g., Vissers et al., 1991; Wittlinger et al., 1998; Skemer et al., 2009; Vauchez et al., 2012). The results here presented bring a valuable contribution to the discussion over the parameters and mechanisms controlling strain localization in the ductile regime.

Based on experimental observations and natural examples, a number of factors are commonly suggested as being responsible for the creation of initial perturbations in an otherwise homogeneous ductile flow. One of the most accredited mechanisms for the localization of strain in the viscous regime is the presence of mechanical discontinuities within a homogeneous rock body, as has been extensively studied in the field (e.g., Tremblay & Malo, 1991; Guermani & Pennacchioni, 1998; Mancktelow & Pennacchioni, 2005; Pittarello et al., 2012), in the laboratory (e.g., Rybacki et al., 2014) and through numerical modelling (e.g., Mancktelow, 2002; Jammes et al., 2015). Whether represented by brittle precursors (joints and fractures), magmatic features (e.g., dykes) or surface discontinuities of various nature (e.g., fine grained pseudotachylytes), mechanical heterogeneities inducing viscosity contrast between phases are an efficient locus for the nucleation of strain localization at all scales. The interaction of this mechanism with environmental factors (e.g., loading conditions, temperature, confining pressure) as well as with further elements known to favour strain softening and localization (e.g., reaction softening, brittle comminution) can have important effects on the efficiency of shear zone formation.

Boundary conditions for the deformation of materials within the Earth's crust can be approximated to two end-member terms, that of a constant velocity (e.g., plate motion) and that of constant stress (e.g., the imposed stress for deformation to be activated). Whether any of these two conditions is more or less favourable to the localization of strain has been the subject of speculation in a previous study (Hansen et al., 2012). In their investigation, Hansen and co-authors have experimentally deformed monomineralic samples of olivine in a Paterson-type deformation apparatus, employing conditions of high temperature ($\approx$ 1200 °C) and confining pressure (300 MPa) and up to total shear strains (in torsion) in the range of $\gamma \approx$ 4-18. Microstructural and textural analysis revealed localized bands of reduced grain size and stronger textural index in samples deformed at constant stress conditions, as opposed to homogeneously deformed constant strain rate specimens. Earlier theoretical studies (e.g., Fressengeas & Molinari, 1987; Paterson,

2007) had already suggested that, while a stress perturbation is necessary in the deforming system to initiate strain localization, the size of such perturbation would be reduced at constant stress boundary conditions, therefore favouring the nucleation of shear zones in these settings.

We intended to experimentally test the hypothesis that, if a mechanism known to favour strain localization (the presence of a material heterogeneity within a homogeneous matrix, e.g. Rybacki et al., 2014) is in place, the effect of the imposed loading conditions on the efficiency of localization is minor if not absent. To do that, we conducted a series of torsion experiments in the Paterson apparatus on a monomineralic system composed of Carrara marble cylinders with single planar inclusions of weaker Solnhofen limestone. The experiments were carried out at high confining pressure (400 MPa) and temperature (900 °C), under conditions of constant torque (stress) or constant twist (strain) rate. Similar bulk shear strains were reached for the two different configurations, to allow for the comparison of resulting microstructures and textures. The viscosity contrast between the two materials (at the experimental conditions employed here, marble is estimated to be in the order of ≈ 10 times stronger than limestone) induces a significant strength perturbation at the tip of the inclusion and consequent strain softening in the Carrara marble matrix. Our experiments succeeded in reproducing the initiation and early propagation stages of a shear zone nucleating at the tip of a single inclusion of weaker material; strain partitioned in shear bands developing in front of the inclusion, characterized by grain size refinement, a weakly foliated fabric and the formation of a strong texture. Microstructural as well as textural analysis was carried out by means of optical microscopy, scanning electron microscopy (SEM), electron back-scatter diffraction (EBSD) and transmission electron microscopy (TEM). Quantification and comparison of parameters like grain size, dislocation density, shape preferred orientation, distribution of recrystallized grain and crystallographic preferred orientation showed that strain localization is largely independent of the imposed boundary conditions. The linear perturbation analysis carried out by Fressengeas and Molinari (1987) and reviewed by Paterson (2007) to advocate for the efficiency of constant stress loading conditions in localizing strain within single phase materials does not appear to be applicable to systems in which large strength perturbations exist. The type of imposed loading conditions did not affect the style and magnitude of the in-plane propagation of strain assisted by a migrating strain weakening front. This suggests a hierarchical organization of the mechanisms controlling the localization of strain in the ductile regime, where the efficiency of some can overcome and obliterate the effect of other ones. The implications of these findings are rather important for the analysis of post-mortem microstructures from natural high-temperature shear zones. In the presence of material heterogeneities inducing stress perturbations and strain softening in deforming materials, the microstructural signature of strain localization observed during nucleation and early shear zone development does not depend on the type of applied loading conditions.

In an effort to extrapolate our findings to the field scale, we developed a numerical model capable of reproducing the phenomenological aspects of our experimental results. Modelling of strain localization in the ductile regime involves the formulation of criteria accounting for mechanical weakening at the microscale. Previous attempts have involved strain-, stress-, deformation work- or grain size-dependent rheological weakening, with markedly different effects on resulting strain localization. We formulated a 2D numerical model with an implemented first-order softening law to mimic mechanical weakening, and benchmarked it to the high-temperature, high-pressure torsion experiments conducted on our Carrara marble with Solnhofen limestone inclusion samples. The three weakening parameters of the strain-dependent softening law employed in the model are derived by iterative comparison with the mechanical data from the experiments. The model successfully reproduces the emergence of a local stress concentration at the tip of the inclusion, the formation of an evolving shear zone and the locally heterogeneous distribution of strain. With the introduction of an arbitrary second softening step, a narrow band of reduced viscosity is formed within the previously described shear zone, in accordance with the frequent occurrence of ultramylonitic layers in the core of heterogeneous natural shear zones. Numerical modelling of this experimental setup showed the potential of formulating softening laws benchmarked against mechanical data. Accounting, in the model, for the strain softening observed to be at the basis of strain localization is necessary to accurately reproduce the experimental results. Consequently, large scale models of crustal processes involving the formation of shear zones must be implemented with solid softening law for their results to be reliable.

The influence of interacting brittle and ductile processes on strain localization is also a topic of great interest in the structural geology community. Natural shear zones are often associated with brittle precursors and/or syn-deformation (micro)fracturing. In these settings, the partitioning of strain between brittle and crystal-plastic processes can affect the geometry of the resulting deformation. We designed a series of experiments to test the effect of different amounts of brittle deformation (in the form of microcracking) on the localization of strain in the presence of material heterogeneities. Our high temperature (900 °C) triaxial deformation experiments were run in a Paterson-type apparatus on Carrara marble cylinders containing non-overlapping couples of weak Solnhofen limestone inclusions arranged in different types of step-over geometry. The areas of stress perturbation induced at the tip of the inclusions by the large viscosity contrast between marble and limestone interact to produce local mean stresses of either compressional or extensional nature in the region comprised between the two inclusions. The applied confining pressures ranged between 30 and 300 MPa, leading to varying amounts of brittle deformation developing in the marble matrix in the areas subjected to viscosity contrast-induced stress concentration, in accordance with the Goetze criterion. Scanning electron microscopy was used for the quantification of the brittle component of deformation. At low confinement (30 and 50 MPa) microcracking is abundant, but its spatial distribution

is a function of the kinematic conditions (compressional or extensional) dominating in the step-over region. A pervasive network of microcracks develops in the process zone between the two inclusions if their arrangement is extensional, while virtually no brittle deformation is present in the compressional step-overs and microcracking is concentrated around the inclusion tips. Crystal plasticity within the marble matrix, investigated by EBSD, is activated in parallel to the brittle processes, and the partitioning of ductile strain appears to mimic the distribution of microcracks, leading to markedly stronger strain localization in samples containing extensional step-overs than compressional ones. As the confining pressure is increased (100 and 300 MPa) and microcrack formation is suppressed almost entirely, localization is also progressively reduced in the extensional step-over samples. The current common understanding is that brittle deformation is in all cases favouring ductile localization. Our results, however, show that the magnitude and "sign" (whether extensional or compressional) of the stress perturbation induced in a strong matrix by stepping-over inclusions arranged in different geometries is what ultimately controls the efficiency of strain localization. Despite the large amount of microcracks observed in samples containing compressional geometry step-overs deformed at low confinement, no substantial strain localization is observed. Upscaling our conclusions to crustal settings, the nature of the seismic activity nucleating in step-over regions between fault arrays is known to be influenced by their kinematic characteristics (Segall & Pollard, 1983). Similarly, the geometry and mechanical behaviour (whether localizing or distributing deformation) of fault zone roots at depth within the ductile regime can be expected to be a function of the overlying step-over kinematics.

Although carbonate rocks are by no means representative lithologies for the middle and lower crustal depths of our planet, their occurrence within sedimentary sequences subjected to complex tectonometamorphic histories during orogenic processes and in subduction zones is well documented (see ***section 1.3.3***). Being calcite substantially weaker than the other most abundant rock-constituent phases, strain localization in these settings often occurs within the calcite-rich layers. The results here presented are, therefore, of great significance for the study of high temperature shear zones at all scales.

6 Outlook

The present study aimed at characterizing in more detail some of the processes that are known to be associated, in nature as well as in the laboratory, with high temperature strain localization. The inherent complexity of natural shear zones (multi-phase systems, complex tectonometamorphic histories, presence of heterogeneities and interaction of several strain weakening and strain hardening mechanisms) is not approachable from a laboratory perspective. If the micromechanical processes concurring to produce large scale strain localization are to be investigated, a simplified approach is necessary. For this reason, we focused our analysis on a monomineralic system, where metamorphic reactions and formation of secondary phases are suppressed, and only one specific localization-inducing mechanism (the presence of material heterogeneities) is operating in the deforming system. Our results shed light on the effects that some of the intervening "environmental" parameters have on the efficiency of strain localization in its nucleating and transient stages. While not exhausting all possibilities of intervening factors in the formation of high temperature shear zones, we investigated parameters we believe to be important to the ongoing discussion over the development of ductile shear zones.

Experimental rock deformation allows for a large degree of freedom to test the influence of the variation of single parameters on a well-characterized system. In this sense, our simple experimental setup lends itself to a large number of further investigations exploring the impact of, for example, different inclusions shapes, or the width of the step-over regions (in the case of inclusion pairs). Moreover, all the experiments presented in this study were conducted at conditions of high temperature (900 °C) to ensure that the viscosity contrast between marble and limestone would be high enough to generate a large stress perturbation in the system and ultimately lead to mechanical weakening and strain localization (Rybacki et al., 2014). Our results, therefore, are quantitatively significant for materials of comparatively different strengths. While we don't expect the nature of the underlying microphysical processes to be dependent on the viscosity contrast between phases, their magnitude and relative contribution is bound to change at the varying of the viscosity-induced stress perturbation. Experimentally investigating the effects of different viscosity contrasts on the ductile localization of strain would also add significance to our results. Although, in nature, carbonate rocks are frequently observed in shear zones at all scales (see ***section 1.3.3***), other lithologies are expected to dominate the middle and lower crustal depths where shear zones form at the roots of crustal scale fault zones. Therefore, investigating the behaviour of non-carbonate rocks in a setup similar to the one developed for our experiments would be of interest for the extrapolation of the present results to natural settings. Along the same lines, the impact of fluid inflow and/or of metamorphic reactions (both known to play a key role in the ductile localization of strain) would equally provide abundant cues for further experimental characterization of the processes at the basis of shear zones formation.

A limitation of our experimental setup (both in torsion and in triaxial compression) is the total bulk strain that can be reached before dynamic instabilities arise and the samples fail along the region of strain localization. Consequently, we conducted our analyses and observations on microstructures and textures that have not reached a steady-state condition and are therefore transient in nature. The results here presented are therefore strictly applicable to the nucleation and early stages of shear zones formation, a situation which is difficult to observe in nature. The torsion setup in the Paterson apparatus was designed with the intention of allowing stable deformation to high (shear) strains, and has been proven successful in this sense in a large number of experimental studies run on monomineralic and/or homogeneously mixed multi-phase materials. Our planar inclusion system, however, has been proven to slip along the shear zone already at bulk strains in the order of $\gamma \approx 2$ (Rybacki, pers. Communication).

The results from this study have addressed some general questions regarding strain localization and can be readily applied to relevant geological settings. Nature is, however, more complicated and a large number of further studies are required to unravel the process of shear zones formation more completely. In addition, numerical modelling can be integrated to experimental work as a powerful tool to upscale experimental results and quickly investigate the effect of key parameters on the system under analysis. Benchmarking modelling results to experimental data is, in this sense, a strong control mechanism to avoid large departures from physical processes that can be hard to detect. In our experience with modelling techniques, however, we encountered difficulties in integrating brittle and ductile processes simultaneously occurring in deforming rock bodies. The development of numerical models capable of handling the feedback effects between the different deformation mechanisms would be a great advance to our capabilities of modelling naturally occurring processes.

References

Afonso, J. C., & Ranalli, G. (2004). Crustal and mantle strengths in continental lithosphere: is the jelly sandwich model obsolete? *Tectonophysics*, *394*(3-4), 221–232.

Austin, N. J., & Evans, B. (2007). Paleowattmeters: A scaling relation for dynamically recrystallized grain size. *Geology*, *35*(4), 343–346.

Austin, N. J., Evans, B., Herwegh, M., & Ebert, A. (2008). Strain localization in the morcles nappe (helvetic alps, switzerland). *swiss Journal of Geosciences*, *101*(2), 341–360.

Austrheim, H. (1987). Eclogitization of lower crustal granulites by fluid migration through shear zones. *Earth and Planetary Science Letters*, *81*(2-3), 221–232.

Auzende, A.-L., Escartin, J., Walte, N. P., Guillot, S., Hirth, G., & Frost, D. J. (2015). Deformation mechanisms of antigorite serpentinite at subduction zone conditions determined from experimentally and naturally deformed rocks. *Earth and Planetary Science Letters*, *411*, 229–240.

Bachmann, F., Hielscher, R., & Schaeben, H. (2010). Texture analysis with mtex–free and open source software toolbox. In *Solid state phenomena* (Vol. 160, pp. 63–68).

Backers, T., Moeck, I., et al. (2015). Fault tips as favorable drilling targets for geothermal prospecting–a fracture mechanical perspective. In *Isrm regional symposium-eurock 2015.*

Badertscher, N. P., & Burkhard, M. (2000). Brittle–ductile deformation in the glarus thrust lochseiten (lk) calc-mylonite. *Terra Nova*, *12*(6), 281–288.

Ballato, P., Brune, S., & Strecker, M. R. (2019). Sedimentary loading–unloading cycles and faulting in intermontane basins: Insights from numerical modeling and field observations in the nw argentine andes. *Earth and Planetary Science Letters*, *506*, 388–396.

Barber, D., & Wenk, H.-R. (1979). Deformation twinning in calcite, dolomite, and other rhombohedral carbonates. *Physics and Chemistry of Minerals*, *5*(2), 141–165.

Barnhoorn, A., Bystricky, M., Burlini, L., & Kunze, K. (2004). The role of recrystallisation on the deformation behaviour of calcite rocks: large strain torsion experiments on carrara marble. *Journal of Structural Geology*, *26*(5), 885–903.

Barnhoorn, A., Bystricky, M., Burlini, L., & Kunze, K. (2005). Post-deformational annealing of calcite rocks. *Tectonophysics*, *403*(1-4), 167–191.

Barnhoorn, A., Bystricky, M., Kunze, K., Burlini, L., & Burg, J.-P. (2005). Strain localisation in bimineralic rocks: experimental deformation of synthetic calcite–anhydrite aggregates. *Earth and Planetary Science Letters*, *240*(3-4), 748–763.

Beaumont, C., Jamieson, R. A., Nguyen, M. H., & Medvedev, S. (2004). Crustal channel flows: 1. numerical models with applications to the tectonics of the himalayan-tibetan orogen. *Journal of Geophysical Research: Solid Earth*, *109*(B6).

Bercovici, D. (1996). Plate generation in a simple model of lithosphere-mantle flow with dynamic self-lubrication. *Earth and Planetary Science Letters*, *144*(1-2), 41–51.

Bercovici, D. (1998). Generation of plate tectonics from lithosphere–mantle flow and void–volatile self-lubrication. *Earth and Planetary Science Letters*, *154*(1-4), 139–151.

Bercovici, D. (2003). The generation of plate tectonics from mantle convection. *Earth and Planetary Science Letters*, *205*(3-4), 107–121.

Bercovici, D., & Karato, S.-i. (2002). Theoretical analysis of shear localization in the lithosphere. *Reviews in mineralogy and geochemistry*, *51*(1), 387–420.

Bercovici, D., & Ricard, Y. (2012). Mechanisms for the generation of plate tectonics by two-phase grain-damage and pinning. *Physics of the Earth and Planetary Interiors*, *202*, 27–55.

Berthé, D., Choukroune, P., & Jégouzo, P. (1979). Orthogneiss, mylonite and non coaxial deformation of granites: the example of the south armorican shear zone. *Journal of Structural Geology*, *1*(1), 31–42.

Bestmann, M., Kunze, K., & Matthews, A. (2000). Evolution of a calcite marble shear zone complex on thassos island, greece: microstructural and textural fabrics and their kinematic significance. *Journal of Structural Geology*, *22*(11-12), 1789–1807.

Blenkinsop, T. G. (1991). Cataclasis and processes of particle size reduction. *Pure and Applied Geophysics*, *136*(1), 59–86.

Bobet, A., & Einstein, H. (1998a). Fracture coalescence in rock-type materials under uniaxial and biaxial compression. *International Journal of Rock Mechanics and Mining Sciences*, *35*(7), 863–888.

Bobet, A., & Einstein, H. H. (1998b). Numerical modeling of fracture coalescence in a model rock material. *International Journal of Fracture*, *92*(3), 221.

Bonet, J., & Wood, R. D. (1997). *Nonlinear continuum mechanics for finite element analysis*. Cambridge university press.

Brace, W., & Kohlstedt, D. (1980). Limits on lithospheric stress imposed by laboratory experiments. *Journal of Geophysical Research: Solid Earth*, *85*(B11), 6248–6252.

Bruhn, D. F., & Casey, M. (1997). Texture development in experimentally deformed two-phase aggregates of calcite and anhydrite. *Journal of Structural Geology*, *19*(7), 909–925.

Bruhn, D. F., Olgaard, D., & Dell'Angelo, L. (1999). Evidence for enhanced deformation in two-phase rocks: Experiments on the rheology of calcite-anhydrite aggregates. *Journal of Geophysical Research: Solid Earth*, *104*(B1), 707–724.

Brune, S. (2014). Evolution of stress and fault patterns in oblique rift systems: 3-d numerical lithospheric-scale experiments from rift to breakup. *Geochemistry, Geophysics, Geosystems*, *15*(8), 3392–3415.

Brune, S. (2016). Rifts and rifted margins: A review of geodynamic processes and natural hazards. *Plate Boundaries and Natural Hazards*, *219*, 13.

Brune, S., & Autin, J. (2013). The rift to break-up evolution of the gulf of aden: Insights from 3d numerical lithospheric-scale modelling. *Tectonophysics*, *607*, 65–79.

Brune, S., Heine, C., Clift, P. D., & Pérez-Gussinyé, M. (2017). Rifted margin architecture and crustal rheology: reviewing iberia-newfoundland, central south atlantic, and south china sea. *Marine and Petroleum Geology*, *79*, 257–281.

Brune, S., Heine, C., Pérez-Gussinyé, M., & Sobolev, S. V. (2014). Rift migration explains continental margin asymmetry and crustal hyper-extension. *Nature Communications*, *5*, 4014.

Brune, S., Popov, A. A., & Sobolev, S. V. (2012). Modeling suggests that oblique extension facilitates rifting and continental break-up. *Journal of Geophysical Research: Solid Earth*, *117*(B8).

Brune, S., Popov, A. A., & Sobolev, S. V. (2013). Quantifying the thermo-mechanical impact of plume arrival on continental break-up. *Tectonophysics*, *604*, 51–59.

Brune, S., Williams, S. E., Butterworth, N. P., & Müller, R. D. (2016). Abrupt plate accelerations shape rifted continental margins. *Nature*, *536*(7615), 201.

Bunge, H.-J. (1982). *Texture analysis in materials science: mathematical methods*. Elsevier.

Burg, J., & Laurent, P. (1978). Strain analysis of a shear zone in a granodiorite. *Tectonophysics*, *47*(1-2), 15–42.

Bürgmann, R., & Dresen, G. (2008). Rheology of the lower crust and upper mantle: Evidence from rock mechanics, geodesy, and field observations. *Annu. Rev. Earth Planet. Sci.*, *36*, 531–567.

Bürgmann, R., Ergintav, S., Segall, P., Hearn, E. H., McClusky, S., Reilinger, R. E., ... Zschau, J. (2002). Time-dependent distributed afterslip on and deep below the izmit earthquake rupture. *Bulletin of the Seismological Society of America*, *92*(1), 126–137.

Burkhard, M. (1993). Calcite twins, their geometry, appearance and significance as stress-strain markers and indicators of tectonic regime: a review. *Journal of structural geology*, *15*(3-5), 351–368.

Burlini, L., & Bruhn, D. (2005). High-strain zones: laboratory perspectives on strain softening during ductile deformation. *Geological Society, London, Special Publications*, *245*(1), 1–24.

Burov, E. (2011). Rheology and strength of the lithosphere. *Marine and Petroleum Geology*, *28*(8), 1402–1443.

Burov, E., Watts, A., et al. (2006). The long-term strength of continental lithosphere:" jelly sandwich" or" crème brûlée"? *GSA today*, *16*(1), 4.

Byerlee, J. (1978). Friction of rocks. In *Rock friction and earthquake prediction* (pp. 615–626). Springer.

Bystricky, M., Heidelbach, F., & Mackwell, S. (2006). Large-strain deformation and strain partitioning in polyphase rocks: Dislocation creep of olivine–magnesiowüstite aggregates. *Tectonophysics*, *427*(1-4), 115–132.

Bystricky, M., Kunze, K., Burlini, L., & Burg, J.-P. (2000). High shear strain of olivine aggregates: Rheological and seismic consequences. *Science*, *290*(5496), 1564–1567.

Bystricky, M., & Mackwell, S. (2001). Creep of dry clinopyroxene aggregates. *Journal of Geophysical Research: Solid Earth*, *106*(B7), 13443–13454.

Carreras, J. (2001). Zooming on northern cap de creus shear zones. *Journal of Structural Geology*, *23*(9), 1457–1486.

Casey, M., Kunze, K., & Olgaard, D. L. (1998). Texture of solnhofen limestone deformed to high strains in torsion. *Journal of Structural Geology*, *20*(2-3), 255–267.

Chen, S., Hiraga, T., & Kohlstedt, D. L. (2006). Water weakening of clinopyroxene in the dislocation creep regime. *Journal of Geophysical Research: Solid Earth*, *111*(B8).

Chen, W.-P., & Molnar, P. (1983). Focal depths of intracontinental and intraplate earthquakes and their implications for the thermal and mechanical properties of the lithosphere. *Journal of Geophysical Research: Solid Earth*, *88*(B5), 4183–4214.

Christiansen, P. P., & Pollard, D. D. (1997). Nucleation, growth and structural development of mylonitic shear zones in granitic rock. *Journal of structural Geology*, *19*(9), 1159–1172.

Clift, P. D., Brune, S., & Quinteros, J. (2015). Climate changes control offshore crustal structure at south china sea continental margin. *Earth and Planetary Science Letters*, *420*, 66–72.

Cook, A., Vel, S., Gerbi, C., & Johnson, S. (2014). Computational analysis of nonlinear creep of polyphase aggregates: Influence of phase morphology. *Journal of Geophysical Research: Solid Earth*, *119*(9), 6877–6906.

Corti, G., van Wijk, J., Cloetingh, S., & Morley, C. K. (2007). Tectonic inheritance and continental rift architecture: Numerical and analogue models of the east african rift system. *Tectonics*, *26*(6).

Coyan, M. M., Arrowsmith, J. R., Umhoefer, P., Coyan, J., Kent, G., Driscoll, N., & Gutíerrez, G. M. (2013). Geometry and quaternary slip behavior of the san juan de los planes and saltito fault zones, baja california sur, mexico: Characterization of rift-margin normal faults. *Geosphere*, *9*(3), 426–443.

Crameri, F. (2018). Geodynamic diagnostics, scientific visualisation and staglab 3.0. *Geoscientific Model Development*, *11*(6), 2541–2562.

Cross, A. J., Ellis, S., & Prior, D. J. (2015). A phenomenological numerical approach for investigating grain size evolution in ductiley deforming rocks. *Journal of Structural Geology*, *76*, 22–34.

Cross, A. J., Prior, D., Stipp, M., & Kidder, S. (2017). The recrystallized grain size piezometer for quartz: An ebsd-based calibration. *Geophysical Research Letters*, *44*(13), 6667–6674.

Cross, A. J., & Skemer, P. (2017). Ultramylonite generation via phase mixing in high-strain experiments. *Journal of Geophysical Research: Solid Earth*, *122*(3), 1744–1759.

Cyprych, D., Brune, S., Piazolo, S., & Quinteros, J. (2016). Strain localization in polycrystalline material with second phase particles: Numerical modeling with application to ice mixtures. *Geochemistry, Geophysics, Geosystems*, *17*(9), 3608–3628.

Dannberg, J., & Heister, T. (2016). Compressible magma/mantle dynamics: 3-d, adaptive simulations in aspect. *Geophysical Journal International*, *207*(3), 1343–1366.

De Borst, R., & Mühlhaus, H.-B. (1992). Gradient-dependent plasticity: formulation and algorithmic aspects. *International Journal for Numerical Methods in Engineering*, *35*(3), 521–539.

De Bresser, J. (1996). Steady state dislocation densities in experimentally deformed calcite materials: Single crystals versus polycrystals. *Journal of Geophysical Research: Solid Earth*, *101*(B10), 22189–22201.

De Bresser, J., Ter Heege, J., & Spiers, C. (2001). Grain size reduction by dynamic recrystallization: can it result in major rheological weakening? *International Journal of Earth Sciences*, *90*(1), 28–45.

De Bresser, J., Urai, J., & Olgaard, D. (2005). Effect of water on the strength and microstructure of carrara marble axially compressed at high temperature. *Journal of Structural Geology*, *27*(2), 265–281.

de Bresser, J. t., & Spiers, C. (1993). Slip systems in calcite single crystals deformed at 300–800 c. *Journal of Geophysical Research: Solid Earth*, *98*(B4), 6397–6409.

Delle Piane, C., Burlini, L., & Grobety, B. (2007). Reaction-induced strain localization: torsion experiments on dolomite. *Earth and Planetary Science Letters*, *256*(1-2), 36–46.

Delle Piane, C., Wilson, C., & Burlini, L. (2009). Dilatant plasticity in high-strain experiments on calcite–muscovite aggregates. *Journal of Structural Geology*, *31*(10), 1084–1099.

Dimanov, A., & Dresen, G. (2005). Rheology of synthetic anorthite-diopside aggregates: Implications for ductile shear zones. *Journal of Geophysical Research: Solid Earth*, *110*(B7).

Dimanov, A., Dresen, G., & Wirth, R. (1998). High-temperature creep of partially molten plagioclase aggregates. *Journal of Geophysical Research: Solid Earth*, *103*(B5), 9651–9664.

Dimanov, A., Dresen, G., Xiao, X., & Wirth, R. (1999). Grain boundary diffusion creep of synthetic anorthite aggregates: The effect of water. *Journal of Geophysical Research: Solid Earth*, *104*(B5), 10483–10497.

Dimanov, A., Lavie, M.-P., Dresen, G., Ingrin, J., & Jaoul, O. (2003). Creep of polycrystalline anorthite and diopside. *Journal of Geophysical Research: Solid Earth*, *108*(B1).

Dimanov, A., Rybacki, E., Wirth, R., & Dresen, G. (2007). Creep and strain-dependent microstructures of synthetic anorthite–diopside aggregates. *Journal of Structural Geology*, *29*(6), 1049–1069.

Döhmann, M. J., Brune, S., Nardini, L., Rybacki, E., & Dresen, G. (2019). Strain localization and weakening processes in viscously deforming rocks: Numerical modeling based on laboratory torsion experiments. *Journal of Geophysical Research: Solid Earth*, *124*(1), 1120–1137.

Dresen, G., & Evans, B. (1993). Brittle and semibrittle deformation of synthetic marbles composed of two phases. *Journal of Geophysical Research: Solid Earth*, *98*(B7), 11921–11933.

Drury, M. R., & Urai, J. L. (1990). Deformation-related recrystallization processes. *Tectonophysics*, *172*(3-4), 235–253.

Duesterhoeft, E., Quinteros, J., Oberhänsli, R., Bousquet, R., & de Capitani, C. (2014). Relative impact of mantle densification and eclogitization of slabs on subduction dynamics: A numerical thermodynamic/thermokinematic investigation of metamorphic density evolution. *Tectonophysics*, *637*, 20–29.

Duretz, T., Petri, B., Mohn, G., Schmalholz, S., Schenker, F., & Müntener, O. (2016). The importance of structural softening for the evolution and architecture of passive margins. *Scientific reports*, *6*, 38704.

Duretz, T., Schmalholz, S., & Podladchikov, Y. (2015). Shear heating-induced strain localization across the scales. *Philosophical Magazine*, *95*(28-30), 3192–3207.

Ebert, A., Herwegh, M., & Pfiffner, A. (2007). Cooling induced strain localization in carbonate mylonites within a large-scale shear zone (glarus thrust, switzerland). *Journal of Structural Geology*, *29*(7), 1164–1184.

Evans, B., & Kohlstedt, D. L. (1995). Rheology of rocks. *Rock Physics and Phase Relations: A Handbook of Physical Constants, AGU Ref. Shelf*, *3*, 148–165.

Fagereng, Å. (2013). Fault segmentation, deep rift earthquakes and crustal rheology: Insights from the 2009 karonga sequence and seismicity in the rukwa–malawi rift zone. *Tectonophysics*, *601*, 216–225.

Ferrill, D. A. (1991). Calcite twin widths and intensities as metamorphic indicators in natural low-temperature deformation of limestone. *Journal of Structural Geology*, *13*(6), 667–675.

Ferrill, D. A., Morris, A. P., Evans, M. A., Burkhard, M., Groshong Jr, R. H., & Onasch, C. M. (2004). Calcite twin morphology: a low-temperature deformation geothermometer. *Journal of structural Geology*, *26*(8), 1521–1529.

Foley, B. J. (2018). On the dynamics of coupled grain size evolution and shear heating in lithospheric shear zones. *Physics of the Earth and Planetary Interiors*, *283*, 7–25.

Fossen, H., & Cavalcante, G. C. G. (2017). Shear zones–a review. *Earth-Science Reviews*, *171*, 434–455.

Fredrich, J. T., Evans, B., & Wong, T.-F. (1989). Micromechanics of the brittle to plastic transition in carrara marble. *Journal of Geophysical Research: Solid Earth*, *94*(B4), 4129–4145.

Fressengeas, C., & Molinari, A. (1987). Instability and localization of plastic flow in shear at high strain rates. *Journal of the Mechanics and Physics of Solids*, *35*(2), 185–211.

Fusseis, F., & Handy, M. (2008). Micromechanisms of shear zone propagation at the brittle–viscous transition. *Journal of Structural Geology*, *30*(10), 1242–1253.

Fusseis, F., Handy, M., & Schrank, C. (2006). Networking of shear zones at the brittle-to-viscous transition (cap de creus, ne spain). *Journal of Structural Geology*, *28*(7), 1228–1243.

Fusseis, F., Regenauer-Lieb, K., Liu, J., Hough, R., & De Carlo, F. (2009). Creep cavitation can establish a dynamic granular fluid pump in ductile shear zones. *Nature*, *459*(7249), 974.

Gardner, R., Piazolo, S., Evans, L., & Daczko, N. (2017). Patterns of strain localization in heterogeneous, polycrystalline rocks–a numerical perspective. *Earth and Planetary Science Letters*, *463*, 253–265.

Geikie, A. (1884). *The crystalline rocks of the scottish highlands.* Nature Publishing Group.

Gerbi, C., Johnson, S. E., Cook, A., & Vel, S. S. (2014). Effect of phase morphology on bulk strength for power-law materials. *Geophysical Journal International*, *200*(1), 374–389.

Goetze, C., & Evans, B. (1979). Stress and temperature in the bending lithosphere as constrained by experimental rock mechanics. *Geophysical Journal International*, *59*(3), 463–478.

Goncalves, P., Poilvet, J.-C., Oliot, E., Trap, P., & Marquer, D. (2016). How does shear zone nucleate? an example from the suretta nappe (swiss eastern alps). *Journal of Structural Geology*, *86*, 166–180.

Griggs, D., & Miller, W. (1951). Deformation of yule marble: part i—compression and extension experiments on dry yule marble at 10,000 atmospheres confining pressure, room temperature. *Geological Society of America Bulletin*, *62*(8), 853–862.

Groshong Jr, R. H., Pfiffner, O. A., & Pringle, L. R. (1984). Strain partitioning in the helvetic thrust belt of eastern switzerland from the leading edge to the internal zone. *Journal of Structural Geology*, *6*(1-2), 5–18.

Guermani, A., & Pennacchioni, G. (1998). Brittle precursors of plastic deformation in a granite: an example from the mont blanc massif (helvetic, western alps). *Journal of Structural Geology*, *20*(2-3), 135–148.

Guillope, M., & Poirier, J. (1979). Dynamic recrystallization during creep of single-crystalline halite: An experimental study. *Journal of Geophysical Research: Solid Earth*, *84*(B10), 5557–5567.

Handy, M. R. (1989). Deformation regimes and the rheological evolution of fault zones in the lithosphere: the effects of pressure, temperature, grainsize and time. *Tectonophysics*, *163*(1-2), 119–152.

Handy, M. R. (1990). The solid-state flow of polymineralic rocks. *Journal of Geophysical Research: Solid Earth*, *95*(B6), 8647–8661.

Handy, M. R. (1994). Flow laws for rocks containing two non-linear viscous phases: a phenomenological approach. *Journal of Structural Geology*, *16*(3), 287–301.

Handy, M. R., & Brun, J.-P. (2004). Seismicity, structure and strength of the continental lithosphere. *Earth and Planetary Science Letters*, *223*(3-4), 427–441.

Handy, M. R., Mulch, A., Rosenau, M., & Rosenberg, C. (2001). The role of fault zones and melts as agents of weakening, hardening and differentiation of the continental crust: a synthesis. *Geological Society, London, Special Publications*, *186*(1), 305–332.

Handy, M. R., & Stünitz, H. (2002). Strain localization by fracturing and reaction weakening—a mechanism for initiating exhumation of subcontinental mantle beneath rifted margins. *Geological Society, London, Special Publications*, *200*(1), 387–407.

Handy, M. R., Wissing, S., & Streit, L. (1999). Frictional–viscous flow in mylonite with varied bimineralic composition and its effect on lithospheric strength. *Tectonophysics*, *303*(1-4), 175–191.

Hansen, L., Zimmerman, M. E., Dillman, A. M., & Kohlstedt, D. L. (2012). Strain localization in olivine aggregates at high temperature: A laboratory comparison of constant-strain-rate and constant-stress boundary conditions. *Earth and Planetary Science Letters*, *333*, 134–145.

Heilbronner, R., & Barrett, S. (2013). *Image analysis in earth sciences: microstructures and textures of earth materials* (Vol. 129). Springer Science & Business Media.

Heine, C., & Brune, S. (2014). Oblique rifting of the equatorial atlantic: why there is no saharan atlantic ocean. *Geology*, *42*(3), 211–214.

Heitzmann, P. (1987). Calcite mylonites in the central alpine "root zone". *Tectonophysics*, *135*(1-3), 207–215.

Herwegh, M., Berger, A., & Ebert, A. (2005). Grain coarsening maps: a new tool to predict microfabric evolution of polymineralic rocks. *Geology*, *33*(10), 801–804.

Herwegh, M., & Kunze, K. (2002). The influence of nano-scale second-phase particles on deformation of fine grained calcite mylonites. *Journal of Structural Geology*, *24*(9), 1463–1478.

Herwegh, M., Poulet, T., Karrech, A., & Regenauer-Lieb, K. (2014). From transient to steady state deformation and grain size: A thermodynamic approach using elasto-visco-plastic numerical modeling. *Journal of Geophysical Research: Solid Earth*, *119*(2), 900–918.

Herwegh, M., Xiao, X., & Evans, B. (2003). The effect of dissolved magnesium on diffusion creep in calcite. *Earth and Planetary Science Letters*, *212*(3-4), 457–470.

Hielscher, R., & Schaeben, H. (2008). A novel pole figure inversion method: specification of the mtex algorithm. *Journal of Applied Crystallography*, *41*(6), 1024–1037.

Hippertt, J., & Hongn, F. (1998). Deformation mechanisms in the mylonite/ultramylonite transition. *Journal of Structural Geology*, *20*(11), 1435–1448.

Hirth, G., & Kohlstedt, D. (2003). Inside the subduction factory. *Rheology of the Upper Mantle and the Mantle Wedge: A View From the Experimentalists, Geophys. Monogr. Ser*, *138*, 83–105.

Hobbs, B., Mühlhaus, H.-B., & Ord, A. (1990). Instability, softening and localization of deformation. *Geological Society, London, Special Publications*, *54*(1), 143–165.

Holyoke III, C. W., & Tullis, J. (2006). Mechanisms of weak phase interconnection and the effects of phase strength contrast on fabric development. *Journal of Structural Geology*, *28*(4), 621–640.

Huang, Y., Chubakov, V., Mantovani, F., Rudnick, R. L., & McDonough, W. F. (2013). A reference earth model for the heat-producing elements and associated geoneutrino flux. *Geochemistry, Geophysics, Geosystems*, *14*(6), 2003–2029.

Huismans, R. S., & Beaumont, C. (2003). Symmetric and asymmetric lithospheric extension: Relative effects of frictional-plastic and viscous strain softening. *Journal of Geophysical Research: Solid Earth*, *108*(B10).

Jackson, J. (2002). Strength of the continental lithosphere: time to abandon the jelly sandwich? *GSA today*, *12*, 4–10.

Jammes, S., Lavier, L. L., & Reber, J. E. (2015). Localization and delocalization of deformation in a bimineralic material. *Journal of Geophysical Research: Solid Earth*, *120*(5), 3649–3663.

Jessell, M. W., Bons, P. D., Griera, A., Evans, L. A., & Wilson, C. J. (2009). A tale of two viscosities. *Journal of Structural Geology*, *31*(7), 719–736.

Jessell, M. W., Siebert, E., Bons, P. D., Evans, L., & Piazolo, S. (2005). A new type of numerical experiment on the spatial and temporal patterns of localization of deformation in a material with a coupling of grain size and rheology. *Earth and Planetary Science Letters*, *239*(3-4), 309–326.

Ji, S., Jiang, Z., Rybacki, E., Wirth, R., Prior, D., & Xia, B. (2004). Strain softening and microstructural evolution of anorthite aggregates and quartz–anorthite layered composites deformed in torsion. *Earth and Planetary Science Letters*, *222*(2), 377–390.

Ji, S., Wang, Z., & Wirth, R. (2001). Bulk flow strength of forsterite–enstatite composites as a function of forsterite content. *Tectonophysics*, *341*(1-4), 69–93.

Ji, S., Wirth, R., Rybacki, E., & Jiang, Z. (2000). High-temperature plastic deformation of quartz-plagioclase multilayers by layer-normal compression. *Journal of Geophysical Research: Solid Earth*, *105*(B7), 16651–16664.

Jiefan, H., Ganglin, C., Yonghong, Z., & Ren, W. (1990). An experimental study of the strain field development prior to failure of a marble plate under compression. *Tectonophysics*, *175*(1-3), 269–284.

Jordan, P. G. (1987). The deformational behaviour of bimineralic limestone-halite aggregates. *Tectonophysics*, *135*(1-3), 185–197.

Kenkmann, T., & Dresen, G. (1998). Stress gradients around porphyroclasts: palaeopiezometric estimates and numerical modelling. *Journal of Structural Geology*, *20*(2-3), 163–173.

Kenkmann, T., & Dresen, G. (2002). Dislocation microstructure and phase distribution in a lower crustal shear zone–an example from the ivrea-zone, italy. *International Journal of Earth Sciences*, *91*(3), 445–458.

Kennedy, L., & White, J. (2001). Low-temperature recrystallization in calcite: Mechanisms and consequences. *Geology*, *29*(11), 1027–1030.

Kenner, S. J., & Segall, P. (2003). Lower crustal structure in northern california: Implications from strain rate variations following the 1906 san francisco earthquake. *Journal of Geophysical Research: Solid Earth*, *108*(B1), ETG–5.

Kilian, R., Heilbronner, R., & Stünitz, H. (2011). Quartz grain size reduction in a granitoid rock and the transition from dislocation to diffusion creep. *Journal of Structural Geology*, *33*(8), 1265–1284.

Kirby, S. H. (1985). Rock mechanics observations pertinent to the rheology of the continental lithosphere and the localization of strain along shear zones. *Tectonophysics*, *119*(1-4), 1–27.

Ko, T. Y., Einstein, H., Kemeny, J., et al. (2006). Crack coalescence in brittle material under cyclic loading. In *Golden rocks 2006, the 41st us symposium on rock mechanics (usrms)*.

Kohlstedt, D., Evans, B., & Mackwell, S. (1995). Strength of the lithosphere: Constraints imposed by laboratory experiments. *Journal of Geophysical Research: Solid Earth*, *100*(B9), 17587–17602.

Koopmann, H., Brune, S., Franke, D., & Breuer, S. (2014). Linking rift propagation barriers to excess magmatism at volcanic rifted margins. *Geology*, *42*(12), 1071–1074.

Kronenberg, A. K., Segall, P., & Wolf, G. H. (1990). Hydrolytic weakening and penetrative deformation within a natural shear zone. *Geophysical Monograph*, *56*, 21–36.

Küster, M., & Stöckhert, B. (1999). High differential stress and sublithostatic pore fluid pressure in the ductile regime—microstructural evidence for short-term post-seismic creep in the sesia zone, western alps. *Tectonophysics*, *303*(1-4), 263–277.

Leroy, Y. M., & Molinari, A. (1992). Stability of steady states in shear zones. *Journal of the Mechanics and Physics of Solids*, *40*(1), 181–212.

Linckens, J., Herwegh, M., Müntener, O., & Mercolli, I. (2011). Evolution of a polymineralic mantle shear zone and the role of second phases in the localization of deformation. *Journal of Geophysical Research: Solid Earth*, *116*(B6).

Little, T., Holcombe, R., & Ilg, B. (2002). Kinematics of oblique collision and ramping inferred from microstructures and strain in middle crustal rocks, central southern alps, new zealand. *Journal of Structural Geology*, *24*(1), 219–239.

Llana-Fúnez, S., & Rutter, E. H. (2008). Strain localization in direct shear experiments on solnhofen limestone at high temperature–effects of transpression. *Journal of Structural Geology*, *30*(11), 1372–1382.

Maggi, A., Jackson, J., Mckenzie, D., & Priestley, K. (2000). Earthquake focal depths, effective elastic thickness, and the strength of the continental lithosphere. *Geology*, *28*(6), 495–498.

Maggi, A., Jackson, J., Priestley, K., & Baker, C. (2000). A re-assessment of focal depth distributions in southern iran, the tien shan and northern india: Do earthquakes really occur in the continental mantle? *Geophysical Journal International*, *143*(3), 629–661.

Mancktelow, N. S. (2002). Finite-element modelling of shear zone development in viscoelastic materials and its implications for localisation of partial melting. *Journal of Structural Geology*, *24*(6-7), 1045–1053.

Mancktelow, N. S., & Pennacchioni, G. (2005). The control of precursor brittle fracture and fluid–rock interaction on the development of single and paired ductile shear zones. *Journal of Structural Geology*, *27*(4), 645–661.

Mancktelow, N. S., & Pennacchioni, G. (2013). Late magmatic healed fractures in granitoids and their influence on subsequent solid-state deformation. *Journal of Structural Geology*, *57*, 81–96.

Mazzotti, S., & Gueydan, F. (2018). Control of tectonic inheritance on continental intraplate strain rate and seismicity. *Tectonophysics*, *746*, 602–610.

Mei, S., & Kohlstedt, D. L. (2000). Influence of water on plastic deformation of olivine aggregates: 1. diffusion creep regime. *Journal of Geophysical Research: Solid Earth*, *105*(B9), 21457–21469.

Meier, T., Grühser, C., & Backers, T. (2018). Workflow for homogenising permeability of a low permeable rock containing a high permeable discrete fracture network. In *80th eage conference and exhibition 2018.*

Menegon, L., Pennacchioni, G., Malaspina, N., Harris, K., & Wood, E. (2017). Earthquakes as precursors of ductile shear zones in the dry and strong lower crust. *Geochemistry, Geophysics, Geosystems*, *18*(12), 4356–4374.

Menegon, L., Stünitz, H., Nasipuri, P., Heilbronner, R., & Svahnberg, H. (2013). Transition from fracturing to viscous flow in granulite facies perthitic feldspar (lofoten, norway). *Journal of Structural Geology*, *48*, 95–112.

Michibayashi, K., & Mainprice, D. (2004). The role of pre-existing mechanical anisotropy on shear zone development within oceanic mantle lithosphere: an example from the oman ophiolite. *Journal of Petrology*, *45*(2), 405–414.

Misra, S., & Mandal, N. (2007). Localization of plastic zones in rocks around rigid inclusions: Insights from experimental and theoretical models. *Journal of Geophysical Research: Solid Earth*, *112*(B9).

Montési, L. G., & Hirth, G. (2003). Grain size evolution and the rheology of ductile shear zones: from laboratory experiments to postseismic creep. *Earth and Planetary Science Letters*, *211*(1-2), 97–110.

Morgan, S. P., Johnson, C. A., & Einstein, H. H. (2013). Cracking processes in barre granite: fracture process zones and crack coalescence. *International journal of fracture*, *180*(2), 177–204.

Nardini, L., Rybacki, E., Döhmann, M. J., Morales, L. F., Brune, S., & Dresen, G. (2018). High-temperature shear zone formation in carrara marble: The effect of loading conditions. *Tectonophysics*, *749*, 120–139.

Okada, Y. (1985). Surface deformation due to shear and tensile faults in a half-space. *Bulletin of the seismological society of America*, *75*(4), 1135–1154.

Palin, R., Searle, M., St-Onge, M., Waters, D., Roberts, N., Horstwood, M., ... Weller, O. (2015). Two-stage cooling history of pelitic and semi-pelitic mylonite (sensu lato) from the dongjiu–milin shear zone, northwest flank of the eastern himalayan syntaxis. *Gondwana Research*, *28*(2), 509–530.

Park, M., & Jung, H. (2017). Microstructural evolution of the yugu peridotites in the gyeonggi massif, korea: Implications for olivine fabric transition in mantle shear zones. *Tectonophysics*, *709*, 55–68.

Paterson, M. (1969). *The ductility of rocks, physics of strength and plasticity as argon, 377–392.* MIT Press, Cambridge, Mass.

Paterson, M. (1970). A high-pressure, high-temperature apparatus for rock deformation. In *International journal of rock mechanics and mining sciences & geomechanics abstracts* (Vol. 7, pp. 517–526).

Paterson, M. (2007). Localization in rate-dependent shearing deformation, with application to torsion testing. *Tectonophysics*, *445*(3-4), 273–280.

Paterson, M., & Olgaard, D. (2000). Rock deformation tests to large shear strains in torsion. *Journal of structural Geology*, *22*(9), 1341–1358.

Pearce, M. A., Wheeler, J., & Prior, D. J. (2011). Relative strength of mafic and felsic rocks during amphibolite facies metamorphism and deformation. *Journal of Structural Geology*, *33*(4), 662–675.

Pennacchioni, G., & Cesare, B. (1997). Ductile-brittle transition in pre-alpine amphibolite facies mylonites during evolution from water-present to water-deficient conditions (mont mary nappe, italian western alps). *Journal of Metamorphic Geology*, *15*(6), 777–791.

Pennacchioni, G., & Mancktelow, N. (2018). Small-scale ductile shear zones: neither extending, nor thickening, nor narrowing. *Earth-Science Reviews*, *184*, 1–12.

Pennacchioni, G., & Mancktelow, N. S. (2007). Nucleation and initial growth of a shear zone network within compositionally and structurally heterogeneous granitoids under amphibolite facies conditions. *Journal of Structural Geology*, *29*(11), 1757–1780.

Pfiffner, O. A. (1985). Displacements along thrust faults. *Eclogae Geologicae Helvetiae*, *78*(2), 313–333.

Pieri, M., Burlini, L., Kunze, K., Stretton, I., & Olgaard, D. L. (2001). Rheological and microstructural evolution of carrara marble with high shear strain: results from high temperature torsion experiments. *Journal of Structural Geology*, *23*(9), 1393–1413.

Pieri, M., Kunze, K., Burlini, L., Stretton, I., Olgaard, D., Burg, J.-P., & Wenk, H.-R. (2001). Texture development of calcite by deformation and dynamic recrystallization at 1000 k during torsion experiments of marble to large strains. *Tectonophysics*, *330*(1-2), 119–140.

Pittarello, L., Pennacchioni, G., & Di Toro, G. (2012). Amphibolite-facies pseudotachylytes in premosello metagabbro and felsic mylonites (ivrea zone, italy). *Tectonophysics*, *580*, 43–57.

Platt, J., & Behr, W. (2011a). Deep structure of lithospheric fault zones. *Geophysical Research Letters*, *38*(24).

Platt, J., & Behr, W. (2011b). Grainsize evolution in ductile shear zones: Implications for strain localization and the strength of the lithosphere. *Journal of Structural Geology*, *33*(4), 537–550.

Platt, J., & Behr, W. (2011c). Lithospheric shear zones as constant stress experiments. *Geology*, *39*(2), 127–130.

Poirier, J. (1980). Shear localization and shear instability in materials in the ductile field. *Journal of Structural Geology*, *2*(1-2), 135–142.

Popov, A. A., & Sobolev, S. (2008). Slim3d: A tool for three-dimensional thermomechanical modeling of lithospheric deformation with elasto-visco-plastic rheology. *Physics of the Earth and Planetary Interiors*, *171*(1-4), 55–75.

Popov, A. A., Sobolev, S. V., & Zoback, M. D. (2012). Modeling evolution of the san andreas fault system in northern and central california. *Geochemistry, Geophysics, Geosystems*, *13*(8).

Poulet, T., Veveakis, M., Herwegh, M., Buckingham, T., & Regenauer-Lieb, K. (2014). Modeling episodic fluid-release events in the ductile carbonates of the glarus thrust. *Geophysical Research Letters*, *41*(20), 7121–7128.

Quinteros, J., Sobolev, S., & Popov, A. A. (2010). Viscosity in transition zone and lower mantle: Implications for slab penetration. *Geophysical Research Letters*, *37*(9).

Quinteros, J., & Sobolev, S. V. (2013). Why has the nazca plate slowed since the neogene? *Geology*, *41*(1), 31–34.

Ramsay, J., & Graham, R. (1970). Strain variation in shear belts. *Canadian Journal of Earth Sciences*, *7*(3), 786–813.

Ranalli, G., & Murphy, D. C. (1987). Rheological stratification of the lithosphere. *Tectonophysics*, *132*(4), 281–295.

Regenauer-Lieb, K., & Yuen, D. A. (2003). Modeling shear zones in geological and planetary sciences: solid-and fluid-thermal–mechanical approaches. *Earth-Science Reviews*, *63*(3-4), 295–349.

Regenauer-Lieb, K., & Yuen, D. A. (2004). Positive feedback of interacting ductile faults from coupling of equation of state, rheology and thermal-mechanics. *Physics of the Earth and Planetary Interiors*, *142*(1-2), 113–135.

Reyes, O., Einstein, H., et al. (1991). Failure mechanisms of fractured rock-a fracture coalescence model. In *7th isrm congress.*

Rogowitz, A., Grasemann, B., Huet, B., & Habler, G. (2014). Strain rate dependent calcite microfabric evolution–an experiment carried out by nature. *Journal of Structural Geology*, *69*, 1–17.

Rogowitz, A., White, J., & Grasemann, B. (2016). Strain localization in ultramylonitic marbles by simultaneous activation of dislocation motion and grain boundary sliding (syros, greece). *Solid Earth*, *7*(2), 355–366.

Rowe, K., & Rutter, E. (1990). Palaeostress estimation using calcite twinning: experimental calibration and application to nature. *Journal of Structural Geology*, *12*(1), 1–17.

Rudnick, R. L., & Gao, S. (2003). Composition of the continental crust. *Treatise on geochemistry*, *3*, 659.

Rutter, E. H. (1972). The influence of interstitial water on the rheological behaviour of calcite rocks. *Tectonophysics*, *14*(1), 13–33.

Rutter, E. H. (1974). The influence of temperature, strain rate and interstitial water in the experimental deformation of calcite rocks. *Tectonophysics*, *22*(3-4), 311–334.

Rutter, E. H. (1995). Experimental study of the influence of stress, temperature, and strain on the dynamic recrystallization of carrara marble. *Journal of Geophysical Research: Solid Earth*, *100*(B12), 24651–24663.

Rutter, E. H., Casey, M., & Burlini, L. (1994). Preferred crystallographic orientation development during the plastic and superplastic flow of calcite rocks. *Journal of Structural Geology*, *16*(10), 1431–1446.

Rutter, E. H., & Schmid, S. M. (1975). Experimental study of unconfined flow of solnhofen limestone at 500 to 600 c. *Geological Society of America Bulletin*, *86*(2), 145–152.

Rybacki, E., & Dresen, G. (2000). Dislocation and diffusion creep of synthetic anorthite aggregates. *Journal of Geophysical Research: Solid Earth*, *105*(B11), 26017–26036.

Rybacki, E., & Dresen, G. (2004). Deformation mechanism maps for feldspar rocks. *Tectonophysics*, *382*(3-4), 173–187.

Rybacki, E., Evans, B., Janssen, C., Wirth, R., & Dresen, G. (2013). Influence of stress, temperature, and strain on calcite twins constrained by deformation experiments. *Tectonophysics*, *601*, 20–36.

Rybacki, E., Gottschalk, M., Wirth, R., & Dresen, G. (2006). Influence of water fugacity and activation volume on the flow properties of fine-grained anorthite aggregates. *Journal of Geophysical Research: Solid Earth*, *111*(B3).

Rybacki, E., Morales, L., Naumann, M., & Dresen, G. (2014). Strain localization during high temperature creep of marble: The effect of inclusions. *Tectonophysics*, *634*, 182–197.

Rybacki, E., Paterson, M. S., Wirth, R., & Dresen, G. (2003). Rheology of calcite–quartz aggregates deformed to large strain in torsion. *Journal of Geophysical Research: Solid Earth*, *108*(B2).

Rybacki, E., Wirth, R., & Dresen, G. (2008). High-strain creep of feldspar rocks: Implications for cavitation and ductile failure in the lower crust. *Geophysical Research Letters*, *35*(4).

Rybacki, E., Wirth, R., & Dresen, G. (2010). Superplasticity and ductile fracture of synthetic feldspar deformed to large strain. *Journal of Geophysical Research: Solid Earth*, *115*(B8).

Schmeling, H., Marquart, G., & Grebe, M. (2017). A porous flow approach to model thermal non-equilibrium applicable to melt migration. *Geophysical Journal International*, *212*(1), 119–138.

Schmid, S., Boland, J., & Paterson, M. (1977). Superplastic flow in finegrained limestone. *Tectonophysics*, *43*(3-4), 257–291.

Schmid, S., Casey, M., & Starkey, J. (1981). The microfabric of calcite tectonites from the helvetic nappes (swiss alps). *Geological Society, London, Special Publications*, *9*(1), 151–158.

Schmid, S., Panozzo, R., & Bauer, S. (1987). Simple shear experiments on calcite rocks: rheology and microfabric. *Journal of structural Geology*, *9*(5-6), 747–778.

Schmid, S., Paterson, M. S., & Boland, J. N. (1980). High temperature flow and dynamic recrystallization in carrara marble. *Tectonophysics*, *65*(3-4), 245–280.

Schmocker, M., Bystricky, M., Kunze, K., Burlini, L., Stünitz, H., & Burg, J.-P. (2003). Granular flow and riedel band formation in water-rich quartz aggregates experimentally deformed in torsion. *Journal of Geophysical Research: Solid Earth*, *108*(B5).

Schubert, G., Turcotte, D. L., & Olson, P. (2001). *Mantle convection in the earth and planets*. Cambridge University Press.

Segall, P., & Pollard, D. D. (1980). Mechanics of discontinuous faults. *Journal of Geophysical Research: Solid Earth*, *85*(B8), 4337–4350.

Segall, P., & Pollard, D. D. (1983). Nucleation and growth of strike slip faults in granite. *Journal of Geophysical Research: Solid Earth*, *88*(B1), 555–568.

Segall, P., & Simpson, C. (1986). Nucleation of ductile shear zones on dilatant fractures. *Geology*, *14*(1), 56–59.

Shen, B., Stephansson, O., Einstein, H. H., & Ghahreman, B. (1995). Coalescence of fractures under shear stresses in experiments. *Journal of Geophysical Research: Solid Earth*, *100*(B4), 5975–5990.

Simo, J. C., & Hughes, T. J. (2006). *Computational inelasticity* (Vol. 7). Springer Science & Business Media.

Skemer, P., Warren, J. M., Kelemen, P. B., & Hirth, G. (2009). Microstructural and rheological evolution of a mantle shear zone. *Journal of Petrology*, *51*(1-2), 43–53.

Stern, R. J. (2016). Is plate tectonics needed to evolve technological species on exoplanets? *Geoscience Frontiers*, *7*(4), 573–580.

Tackley, P. J. (2000). Mantle convection and plate tectonics: Toward an integrated physical and chemical theory. *Science*, *288*(5473), 2002–2007.

Tasaka, M., Zimmerman, M. E., Kohlstedt, D. L., Stünitz, H., & Heilbronner, R. (2017). Rheological weakening of olivine+ orthopyroxene aggregates due to phase mixing: Part 2. microstructural development. *Journal of Geophysical Research: Solid Earth*, *122*(10), 7597–7612.

Tembe, S., Lockner, D. A., & Wong, T.-F. (2010). Effect of clay content and mineralogy on frictional sliding behavior of simulated gouges: Binary and ternary mixtures of quartz, illite, and montmorillonite. *Journal of Geophysical Research: Solid Earth*, *115*(B3).

Ter Heege, J., De Bresser, J., & Spiers, C. (2002). The influence of dynamic recrystallization on the grain size distribution and rheological behaviour of carrara marble deformed in axial compression. *Geological Society, London, Special Publications*, *200*(1), 331–353.

Thatcher, W., & England, P. C. (1998). Ductile shear zones beneath strike-slip faults: Implications for the thermomechanics of the san andreas fault zone. *Journal of Geophysical Research: Solid Earth*, *103*(B1), 891–905.

Thielmann, M., & Kaus, B. J. (2012). Shear heating induced lithospheric-scale localization: Does it result in subduction? *Earth and Planetary Science Letters*, *359*, 1–13.

Tommasi, A., Knoll, M., Vauchez, A., Signorelli, J. W., Thoraval, C., & Logé, R. (2009). Structural reactivation in plate tectonics controlled by olivine crystal anisotropy. *Nature Geoscience*, *2*(6), 423.

Treagus, S. H., & Lan, L. (2004). Deformation of square objects and boudins. *Journal of Structural Geology*, *26*(8), 1361–1376.

Tremblay, A., & Malo, M. (1991). Significance of brittle and plastic fabrics within the massawippi lake fault zone, southern canadian appalachians. *Journal of structural geology*, *13*(9), 1013–1023.

Trepmann, C. A., & Stöckhert, B. (2002). Cataclastic deformation of garnet: a record of synseismic loading and postseismic creep. *Journal of Structural Geology*, *24*(11), 1845–1856.

Trepmann, C. A., & Stöckhert, B. (2003). Quartz microstructures developed during non-steady state plastic flow at rapidly decaying stress and strain rate. *Journal of Structural Geology*, *25*(12), 2035–2051.

Tullis, T. E., Horowitz, F. G., & Tullis, J. (1991). Flow laws of polyphase aggregates from end-member flow laws. *Journal of Geophysical Research: Solid Earth*, *96*(B5), 8081–8096.

Valoroso, L., Chiaraluce, L., Piccinini, D., Di Stefano, R., Schaff, D., & Waldhauser, F. (2013). Radiography of a normal fault system by 64,000 high-precision earthquake locations: The 2009 l'aquila (central italy) case study. *Journal of Geophysical Research: Solid Earth*, *118*(3), 1156–1176.

Vauchez, A., Clerc, C., Bestani, L., Lagabrielle, Y., Chauvet, A., Lahfid, A., & Mainprice, D. (2013). Preorogenic exhumation of the north pyrenean agly massif (eastern pyrenees-france). *Tectonics*, *32*(2), 95–106.

Vauchez, A., Neves, S., Caby, R., Corsini, M., Egydio-Silva, M., Arthaud, M., & Amaro, V. (1995). The borborema shear zone system, ne brazil. *Journal of South American Earth Sciences*, *8*(3-4), 247–266.

Vauchez, A., & Tommasi, A. (2003). Wrench faults down to the asthenosphere: Geological and geophysical evidence and thermomechanical effects. *Geological Society, London, Special Publications*, *210*(1), 15–34.

Vauchez, A., Tommasi, A., & Mainprice, D. (2012). Faults (shear zones) in the earth's mantle. *Tectonophysics*, *558*, 1–27.

Vissers, R., Drury, M., Strating, E. H., & Wal, D. v. d. (1991). Shear zones in the upper mantle: A case study in an alpine iherzolite massif. *Geology*, *19*(10), 990–993.

Wang, R., Zhao, Y., Chen, Y., Van, H., Yin, Y.-Q., Yao, C.-Y., & Zhang, H. (1987). Experiment and finite element simulation of x-type shear fractures from a crack in marble. *Tectonophysics*, *144*(1-3), 141–150.

Warren, J. M., & Hirth, G. (2006). Grain size sensitive deformation mechanisms in naturally deformed peridotites. *Earth and Planetary Science Letters*, *248*(1-2), 438–450.

Webber, S., Ellis, S., & Fagereng, Å. (2018). "virtual shear box" experiments of stress and slip cycling within a subduction interface mélange. *Earth and Planetary Science Letters*, *488*, 27–35.

Weber, M., Abu-Ayyash, K., Abueladas, A., Agnon, A., Al-Amoush, H., Babeyko, A., ... others (2004). The crustal structure of the dead sea transform. *Geophysical Journal International*, *156*(3), 655–681.

Wenk, H.-R. (1985). Carbonates. In *Preferred oreintation in deformed metals and rocks: an introduction to modern texture analysis* (pp. 361–384).

Wenk, H.-R., Armann, M., Burlini, L., Kunze, K., & Bortolotti, M. (2009). Large strain shearing of halite: Experimental and theoretical evidence for dynamic texture changes. *Earth and Planetary Science Letters*, *280*(1-4), 205–210.

Wenk, H.-R., Rybacki, E., Dresen, G., Lonardelli, I., Barton, N., Franz, H., & Gonzalez, G. (2006). Dauphiné twinning and texture memory in polycrystalline quartz. part 1: experimental deformation of novaculite. *Physics and chemistry of minerals*, *33*(10), 667.

Wenk, H.-R., Venkitasubramanyan, C., Baker, D., & Turner, F. (1973). Preferred orientation in experimentally deformed limestone. *Contributions to Mineralogy and Petrology*, *38*(2), 81–114.

White, S. (1976). A discussion on natural strain and geological structure-the effects of strain on the microstructures, fabrics, and deformation mechanisms in quartzites. *Philosophical Transactions of the Royal Society of London. Series A, Mathematical and Physical Sciences*, *283*(1312), 69–86.

White, S., Burrows, S., Carreras, J., Shaw, N., & Humphreys, F. (1980). On mylonites in ductile shear zones. *Journal of Structural Geology*, *2*(1-2), 175–187.

Wirth, R. (2005). Focused ion beam (fib): applications in micro-and nanoanalysis in geosciences and applied mineralogy. *Practical Metallography*, *42*(4), 188–205.

Wittlinger, G., Tapponnier, P., Poupinet, G., Mei, J., Danian, S., Herquel, G., & Masson, F. (1998). Tomographic evidence for localized lithospheric shear along the altyn tagh fault. *Science*, *282*(5386), 74–76.

Wong, L., & Einstein, H. (2009). Crack coalescence in molded gypsum and carrara marble: part 1. macroscopic observations and interpretation. *Rock Mechanics and Rock Engineering*, *42*(3), 475–511.

Wong, R. H., & Chau, K. (1998). Crack coalescence in a rock-like material containing two cracks. *International Journal of Rock Mechanics and Mining Sciences*, *35*(2), 147–164.

Zang, A., Wagner, F. C., Stanchits, S., Janssen, C., & Dresen, G. (2000). Fracture process zone in granite. *Journal of Geophysical Research: Solid Earth*, *105*(B10), 23651–23661.

Zhu, L. (2000). Crustal structure across the san andreas fault, southern california from teleseismic converted waves. *Earth and Planetary Science Letters*, *179*(1), 183–190.